UNIVERSITY OF SOUTHAMPTON

Potential engineering of optically trapped nanospheres

by

George Paul Winstone

A thesis submitted in partial fulfillment for the degree of Doctor of Philosophy

in the

Faculty of Physical and Applied Sciences

Physics and Astronomy

March 2019

Declaration of Authorship

I, George Paul Winstone, declare that this thesis titled, 'Potential engineering of optically trapped nanospheres' and the work presented in it are my own. I confirm that:

- This work was done wholly or mainly while in candidature for a research degree at this University.
- Where any part of this thesis has previously been submitted for a degree or any other qualification at this University or any other institution, this has been clearly stated.
- Where I have consulted the published work of others, this is always clearly attributed.
- Where I have quoted from the work of others, the source is always given. With the exception of such quotations, this thesis is entirely my own work.
- I have acknowledged all main sources of help.
- Where the thesis is based on work done by myself jointly with others, I have made clear exactly what was done by others and what I have contributed myself.

Signed: _____

Date: 21/03/2019

"I have no mouth. And I must scream."

Harlan Ellison

UNIVERSITY OF SOUTHAMPTON

Abstract

Faculty of Physical and Applied Sciences
Physics and Astronomy

Doctor of Philosophy

by George Paul Winstone

This thesis documents a first principle analysis of the motion of a levitated particle in the potential defined by a Gaussian optical focus. The linear and nonlinear motional modes enabled by a full expansion of the Gaussian potential are explored and modifications to this potential are engineered by superimposing additional fields in the spatial domain as well as selectively enhancing particular terms in the potential by time driving operations.

We describe new experimental results in modulating the motion of a charged suspended nanoparticle with the dispersion forces projected by its interaction with a dielectric surface and discuss its possible application as a levitated atomic force microscope, as well as future investigations of Casimir-Polder interactions.

Control over the nonlinear terms of the particles motion is demonstrated by generating controllable Fano resonances by using both spatial and temporal potential additions independently. In both cases we generate resonances of positive and negative Fano factors. We also selectively enhance the Duffing factor of the potential to show a controllable double well separation and demonstrate preliminary results of limited chaotic motion of a levitated nanoparticle.

Acknowledgements

I'd like to thank the favourable market volatility over Christmas 2017 for allowing me to fund a trip home to the UK in lieu of travel funding, the Universe for teaching me how to do research with a minimal budget, Professor Hendrik Ulbricht for his significant reserves of patience, Muddassar Rashid for being a great human being, David Hempston for the comedy and useful discussion, Ashley setter and Chris Timberlake for discussions and ideas, Marko Toros for a great deal of theoretical input, James Bateman for very good ideas, Marek Schmitt for cleanroom assistance, Tokyo for being a cool city and Hiroshi Mizuta for hosting me at JAIST. Stefan Buhmann and Robert Bennet wrote the theory for the surface dispersion interactions. Robert Bennet performed the numerical simulation for the Morse potential. Markos Toros wrote the expanded theory for the Fano resonance experiment. The Iridis 4 cluster at Southampton and Cray HPC cluster at JAIST provided valuable computing power. Lastly, I wish to thank my parents for being themselves.

Supporting Publications

Direct measurement of short-range forces with a levitated nanoparticle

Physical Review A

Force sensing with an optically levitated charged nanoparticle

Applied Physics Letters

Optically driven mechanical Fano resonances of a levitated nanoparticle

In preparation

Electric field mediated Fano resonances of a levitated nanoparticle

In preparation

Chaotic motion of a levitated nanoparticle

In preparation

Contents

List of Figures

Chapter 1

Levitated Optomechanics

1.1 Chapter overview

This chapter gives a brief overview of levitated optomechanics, outlines why experiments of this type in the femtogram regime are interesting and presents an overview of the general physics of the system studied throughout this thesis that can be broadly transferred between the specific experiments of each chapter.

1.2 Motivations and brief introduction to levitated optomechanics

Levitated optomechanics is the manipulation and control of mechanical resonators or test masses via their interactions with driving fields [10][11]. The field of research potentially offers the exploration of quantum mechanical systems in an increasingly macroscopic regime[12], large potential sensitivities for specific regimes of inertial sensing [11], and a platform for the embedding of environmentally isolated qubits for quantum information processing[13].

While levitated optomechanics often refers to the control and manipulation of nano, micro and millimetre scale objects[11], the same physical principles of decoupled or isolated test masses or cavities are often applied to much larger systems, such as LIGO[14], VIRGO[15] and ESA's future LISA [16] mission.

In solid state or with otherwise membrane based resonators, creation of an oscillator in a bespoke potential is done by design of the physical clamping structure and geometry of the resonantor. In a levitated system these bespoke potentials are generated by

manipulating the applied fields in space and time, both of which can usually be done much more readily on a real time basis than making changes to the design of a substrate based system. While methods of real time spatial and temporal manipulation exist in both the substrate bound[17] and levitated resonator cases, doubling the power of a laser or manipulating the pixels in a spatial modulator is often easier than constructing a new MEMS device from scratch. Furthermore, levitated systems offer the virtual elimination of clamping losses as well as easy access to high mechanical quality(Q) factors[18]. On the other hand, as another axis of comparison, substrate bound mechanical resonators are almost always more scalable in number than their levitated counterparts.

This inherent flexibility of the potential of the resonator is highly motivating for both the development of highly sensitive measurement devices as well as the exploration of fundamental physics since an oscillator of a required resonant frequency, motional mode or susceptibility equation can be just a case of choosing right driving fields.

1.2.1 Macroscopicity

Exploring the limits of the quantum mechanics and how it extends both conceptually and scientifically into the macroscopic world in which we inhabit is a significant element of modern physics. We might explore the concept of locality, or its loss through photon based entanglement experiments [19]. Or we might explore the limits of the quantum superposition principle by generating ever more massive quantum superpositions, such as those created by neutron diffraction [20] or Bose-Einstein condensed atoms [21]. Quantum optomechanics often concerns itself with the latter case generating massive quantum superpositions, we now discuss the meaning of the term 'massive' in this context.

While defining the exact measure for the 'macroscopicity' of a superposition remains a matter for some debate in the community, measures do exist [22][23]. For an interference experiment, the macroscopicity μ can be expressed as:

$$\mu = log_{10}\Big[\frac{1}{ln(f)}(\frac{M}{m_e})^2\frac{t}{1s}\Big] \tag{1.1}$$

where M is the mass of the interfered species, m_e is an arbitrarily chosen reference mass (in this case the mass of the electron is used), t the coherence lifetime of the experiment and f the fraction of the expected interference visibility. Thus, when we refer to the size of macroscopic quantum experiment, we refer to the numerical value of the quantity μ. It is important to note here that the macroscopicity scales more strongly with the mass of the inteferometer species than the life time of the state.

The creation of ever greater macroscopic superpositions has been a significant cornerstone of the levitated optomechanics community to date. With such experiments as the superposition of fullerene spheres [24], large molecules [25], and the interference of nanoparticles [26] and even microparticles[27] planned for the near future. One goal of generating and pushing the size of such a measure is to push the limit of quantum mechanical systems until their existence contradicts and thereby tests existing theories describing the intermediate regime between the quantum and classical regimes of matter. To give a an indication as to the progress of the field, nanosphere interference would give a macroscopicity of 20.5[23], whilst the interference of a literal Schrodinger's cat would give a value of 57[23].

The motivation for the exploration of such intermediate states being to make a serious attempt at solving the measurement problem [28] in quantum mechanics, that is to say, how exactly does the collapse of a wavefunction of a quantum state to a classical reality occur. Conventionally, decoherence provides the link between the quantum and classical, however decoherence does not actually explain how wavefunction collapse occurs, rather it only states that it does.

Continuous Spontaneous Localization (CSL)[29] and Schrodinger-Newton [30] models provide two of the leading theories with regards to wavefunction collapse. The central posit of CSL states that there exists a universal noise field that should limit the lifetime of highly macroscopic quantum states. In the case of Schrodinger-Newton, the central idea is that the wavefunction is a literal distribution of mass (rather than the conventional picture of a probability distribution) that should express self gravitation, leading to size dependant wavefunction collapse that would again, limit the lifetime of macroscopic quantum states.

The quantum ground state of otherwise large mass systems such as membrane resonators is less interesting for the testing of such theories because of the relatively low amplitude of its zero point motion. If the same mass were to be used to produce an interefference pattern in a free fall interferometer, it give a larger macroscopicity number by the popularly accepted measure.

One further point of physical interest in the generation of macroscopic quantum superpositions is the possibility to ascertain whether gravity is a phenomenon that acts 'quantum mechanically' [31]. While the other fundamental forces of nature have theoretical description consistent with quantum field theory, gravity remains non renormalizable and the lack of a quantum theory of gravity remains a major unsolved problem in modern physics. Theoretical proposals to generate quantum superpositions massive enough and close enough together such that gravitational effects between the quantum states become significant [31] do exist.

As one last element of motivation for why optomechanics in the quantum regime is interesting, some smaller viruses are on the scale of some 10's of nm [32], and some bacterium on the scale of 100's of nm. Bearing in mind the length scale of these agents combined with the fact that several experimental groups are approaching groundstate for a levitated nanoparticle [10], it is reasonable to say that an object of size of a living component could be put into a state of quantum superposition in the near future [33].

The idea that something that is in principle alive (or at least the size of something alive) could be put into a state of quantum superposition is both fundamentally interesting from a conceptual point of view, and also from the cynical point of view of attracting public interest and thus funding to the field.

The above arguments represent, to some degree, some of the grand planned goals of the field of levitated optomechanics for the near future. However, for it to be scientifically interesting to work on in the mid term, the intermediate goals also need to be of value. The main arguments for studying such a field outside of or just outside of the quantum regime, are the development of high sensitivity force measurement devices[34], nanoscale information engines[35], and optomechanical circuit components, and these concepts are described in more detail elsewhere in this thesis.

1.3 Simple motional model

In the simple, equilibrium, linear case, a high field seeking (attracted to regions of high potential, such as the focus of a laser) dielectric particle in an optical gradient trap can be modelled as three one-dimensional linear driven damped harmonic oscillators[11], conceptually similar to figure 1.1. These oscillators exhibit coupling to each others motion, defined by the the exact potential configuration in the region explored by the particle during its motion, background gas collisions and other mechanisms detailed in section 1.3.3. The coupling between degrees of freedom therefore decreases with pressure and the volume of the trap explored, and can generally be treated as decoupled from one another if the particle is held in a vacuum below 10 mbar [10] and is in thermodynamic equilibrium (subsection 1.3.1) with an equivalent of a non geometrically biased (no preferred direction) and memory-less heat bath (see appendix A for the justification of these terms to the background gas collisions experienced by the particle), such as a parametric feedback scheme or background gas collisions at a density significantly below that required for the particle to be in the drift diffusion limit.

In this simple model, each degree of freedom follows the equation of motion[10]:

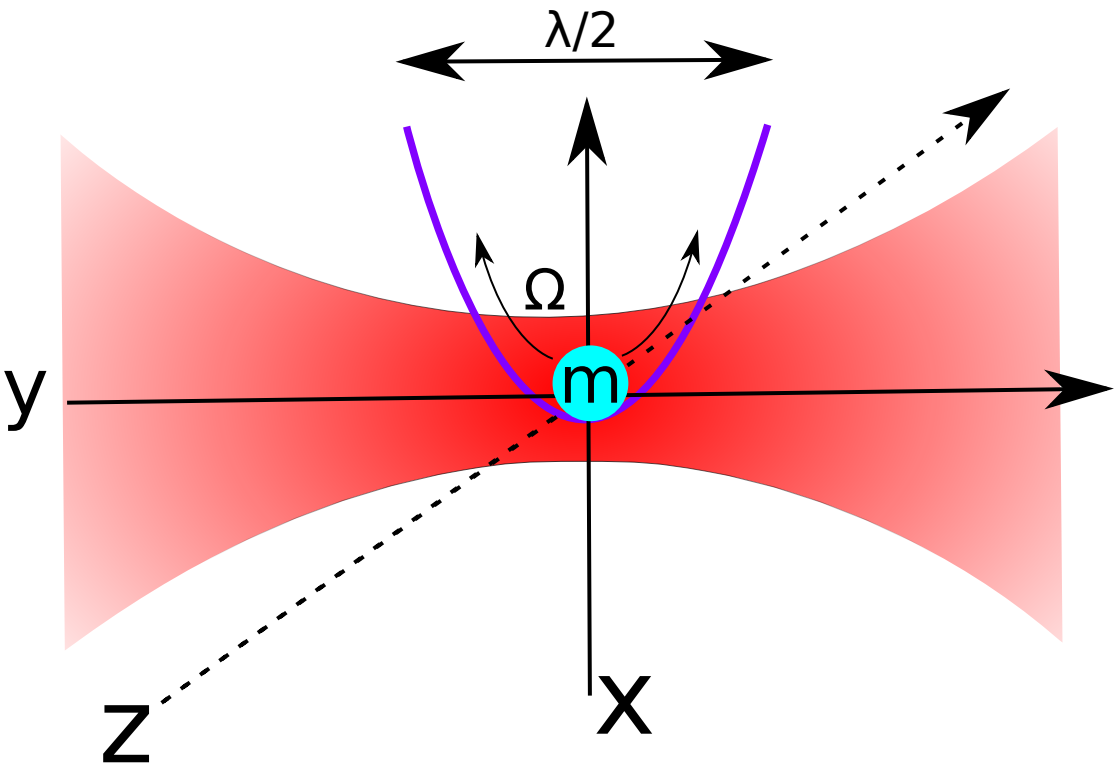

FIGURE 1.1: Simple conceptual diagram of an optically trapped nanoparticle of mass m, natural oscillation frequency Ω undergoing motion in the y axis.

$$\ddot{y} + \gamma\dot{y} + \Omega y = \frac{1}{m}F(t) \tag{1.2}$$

In which γ describes the damping or heating to a degree of freedom of the particles motion, Ω describes the natural frequency of that oscillator, m represents the oscillators mass, y the oscillators displacement and $F(t)$ describes the time fluctuating forces acting on the particle. γ and ω are in units of Hz, m is in units of kilograms and $F(t)$ is in units of Newtons.

1.3.1 Definition of temperature

The particle may be considered to have two temperatures, an internal and an external temperature. The internal temperature referring to motion of its constituent atoms inside the lattice of the silicon dioxide glass that the nanoparticle is composed of. Whilst the particle is levitated in a vacuum, its internal temperature is determined by the intensity of the trapping laser field, along with the particle's absorption and emissivity characteristics at that wavelength and the contact between the particle and random gas collisions in the vacuum chamber[36].

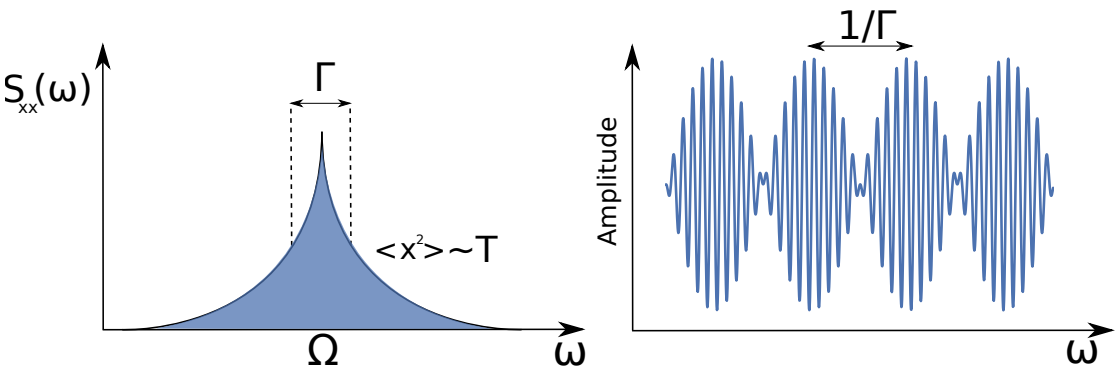

FIGURE 1.2: Left: Lorentzian resonance lineshape of a driven damped harmonic oscillator (equation 1.2) manifesting as a 'temperature' corresponding to an external degree of freedom of the system. S_{xx} is the power spectral density (PSD) of the systems motion at a frequency Ω. Ω is the natural frequency of the oscillator and Γ the damping on the same oscillator, equal to the full width half maximum (FWHM) of the PSD. The area under the PSD is equal to the variance of the square motion of the particle and is taken to be the particle's external temperature. Right: Visual representation of the physical meaning of the damping time $\frac{1}{\Gamma}$ on a simulated time trace.

The quantity defined as the particles external temperature represents its thermodynamic balance with a heatbath or baths composed of random kicks to its motion imparted by background gas collisions, optical imperfections, mechanical vibrations of the experimental apparatus and laser noise[10].

1.3.2 Definition of equilibrium

The definition of equilibrium in our system requires the particle to experience all frequency modes of the heatbath. Experimentally, this can be seen with the data given in section 1.8.1. Mathematically however, this can also be seen from the constraint of the Wiener-Khinchin requirement of the limit $t \to \infty$[37]. A natural question is what are the experimental timescales required to be a good approximation of this, which is explored in section 1.8.1, with the answer turning out to be a surprisingly macroscopic number, a small number of seconds depending on the laser power. This raises significant implications for the ease of doing non-equilibrium thermodynamics experiments in this system, namely that manipulation (of the system) on the characteristic timescale of the particles motion may not be required.

1.3.3 Coupling between degrees of freedom

Coupling mechanisms between the particles internal and external degrees of freedom do exist[2] and are often blamed as a mechanism for particle loss, with several coupling

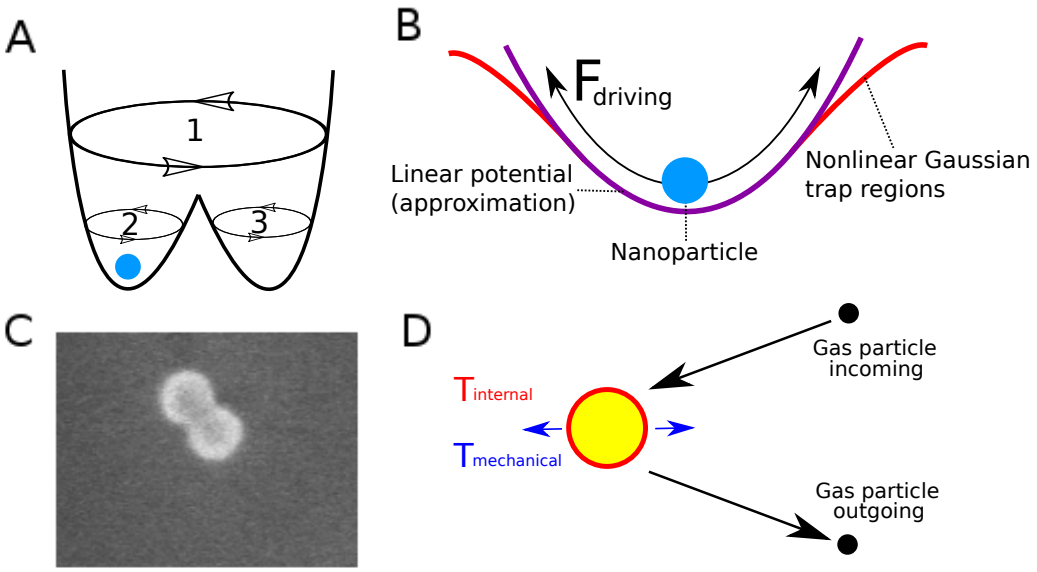

FIGURE 1.3: Methods of generating coupled or nonlinear equations of motion for the nanoparticle-light system. A) A spatially nonlinear potential, in this case an optical multiwell, discussed in section 4. B) coupling between degrees of freedom enforced by using time domain driving operations to drive the particle into the nonlinear regions of its Gaussian potential (occuring at high displacements from the center), where the degrees of freedom are substantially coupled and additional frequency modes are generated, sections 3.84 and 6. C) A cluster composed of two fused nanoparticles, which will result in a nonlinear equation of motion with additional degrees of freedom, coupled motional modes and precession[1]. While these are not discussed at length in this thesis, examples are given in Appendix C and possible methods of deconvoluting the motional modes of arbitrary cluster shapes is discussed in section 5. D) Coupling between internal and external degrees of freedom or temperatures, mediated by gas collisions. As the different Cartesian degrees of freedom (x,y and z) are all coupled to the internal degree of freedom (the particle's temperature) by this mechanism, this also provides a mechanism for coupling between the external degrees of freedom as well, in a method analogous to the zeroth law of thermodynamics. T^{imp} and T^{em} represent the momentum assigned to a gas particle in the vacuum chamber before and after collision with the nanosphere, T_{CM} the centre of mass of external temperature corresponding to a degree of freedom of the nanoparticles motion and T_{sur} represents the surface temperature of the nanoparticle, often referred to as the internal temperature. Reproduced from [2]

.

mechanisms detailed in figure 1.3. This thesis deals almost exclusively with the particles' external degrees of freedom, and thus external temperature.

Methods of generating coupled or nonlinear equations of motion for the nanoparticle-light system are discussed in figure 1.3. Spatially non uniform potentials (A), and time driving operations (B) are the main focus of this thesis. Non-uniform particles (C) are discussed briefly in [38][39] and coupling from gas particle collisions (D) is discussed in [40].

1.4 Fokker-Planck approach

A Fokker-Planck equation is a general mathematical tool that can describe the time evolution of a particle displaying velocity coupled drag and random perturbations to its motion. Specifically, the evolution of its statistical distribution over time. Here we use it to give an intuitive framework between the balance of cooling/heating channels applied to the particle and its resultant temperature, and thus (average) phonon occupation number.

1.4.1 Basic formulation

As the heating or cooling process of the particle colliding with residual atmospheric particles is stochastic, the evolution of the energy associated to each degree of motion of the nanoparticle should follow a Fokker-Planck relation[10][41]:

$$\frac{d}{dt}E(t) = -\zeta[E(t) - E_\infty] \tag{1.3}$$

with E_∞ as the average energy in a steady state and E(t) as the energy at a time t, ζ is the rate at which the system is reaching its steady state, and with the energy of the particle quantised as:

$$< E_n >=< n > \hbar\Omega \tag{1.4}$$

In which Ω is the natural frequency of the oscillator in the laser trapping field.

An important implication of the relationship between the principle oscillator frequency and its energy levels is that a higher frequency has a higher absolute energy value for its groundstate (n=0). Given that $E = k_B T$ where k_B is the Boltzmann constant and T is temperature in Kelvin, this fact is exploited by GHz frequency substrate based membranes to reach groundstate[11][42] by having the systems groundstate $E_{n=0}$ represent a relatively high absolute temperature.

In such a system the occupation number (in phonons) of each degree of freedom can be written as:

$$n_\infty = \frac{\Gamma}{\gamma} \tag{1.5}$$

where damping γ and heating Γ, correspond to the heating and cooling rates associated with each heating or cooling mechanism for each degree of motion of the nanoparticle.

In actuality, heating and cooling channels correspond to a variety of mechanisms, with net heating and cooling rates expandable to a series of both discovered and undiscovered effects[10]:

$$n_\infty = \frac{\Gamma_{th} + \Gamma_{fb} + \Gamma_{other}}{\gamma_{th} + \gamma_{fb} + \gamma_{other}} \tag{1.6}$$

where Γ_{th} and Γ_{fb}, correspond to the heating channels associated with heat baths and the feedback loop respectively. γ_{th} and γ_{fb} correspond to the cooling channels or mechanisms associated with heatbaths and the feedback loop respectively. Finally Γ_{other} and γ_{other} respond to other various heating and cooling channels both discovered and undiscovered, with examples being heating through Rayleigh scatter of photons from the nanoparticle[10], heating through coupling of internal and external degrees of freedom[2] and heating through the particles non spherical geometry giving it a set of rotation dependent anharmonic potentials.

Achieving quantum groundstate is therefore a matter of having a sufficiently low total heating rate Γ, sufficiently high cooling rate γ for the desired $E_{n=0}(\Omega)$. Since certain heating mechanisms are intrinsic to the system (photon recoil will always be present if a laser is used to levitate the particle), the groundstate with an optically levitated particle may well be reached by the application of a superior cooling channel or cooling a high frequency degree of freedom. Using a different field (such as a magnetic field[33]) to levitate a similar sized test mass will of course eliminate photon recoil, however undiscovered and inconvenient heating mechanisms may well exist in those systems as well.

As the field of research stands at present, a levitated nanoparticle has not been forced into the ground state, with a number of experimental constraints and physical mechanisms being given as suspected reasons for this. It has been suggested by some in the field that more convoluted operations than simple feedback cooling such as using nonlinear potentials[43] or pulsed operations[44][45] could be utilized to access non classical states of motion[46]. Even without achieving quantum ground state, the current positional resolution, force[47] and acceleration sensitivities[48] is impressive for a non interferometric test mass. Proposals exist to employ this sensitivity for genuine scientific applications in the near future, such as the detection of high frequency gravity waves[49].

1.4.2 Ensemble of energy levels

Whilst the heating channels mention in section 1.4 are associated with heating or cooling rates represented in units of Hz[10], they are at heart stochastic processes, the given heating rate is an average value. The practical effect of this is that even when the particle is in a steady state, its energy fluctuates on short timescales. Motionally, this resolves as the particle undertaking oscillations at many different amplitudes over time, each amplitude corresponding to an energy value of the particle. Experimentally, this can be seen in section 1.7.3.

Each energy level corresponds to a harmonic motional mode. The sum of this ensemble of motional modes gives rise to single peak in the histogram of the particles displacement through the central limit theorem[50] scaling, shown in figure 1.4. This kind of analysis of the particles energy distribution is expanded upon somewhat in section 2.7.3.

In the classical limit the particle should follow Maxwell-Boltzmann statistics while as a quantum harmonic oscillator the particle is likely to follow a Bose-Einstein distribution of energies. Naturally for high occupation numbers the distribution of particle energies should look identical from both statistic distributions, an interesting question is at what energy level of the quantum harmonic oscillator will the behaviour start to diverge. This however is a highly theoretical problem beyond the scope of this thesis.

1.5 Optical gradient trapping, mechanism

1.5.1 Derivation of gradient potential for a high field seeking dielectric polarisable particle.

A parabolic reflective optic focuses a beam to a Gaussian point spread function, the intensity of which is given by[51]:

$$I = I_0 \frac{w_0^2}{w}^2 e^{-2\frac{x^2+y^2}{w^2}} \tag{1.7}$$

In which I_0 represents the total intensity of the laser, w_0 the minimum beam waist of the laser and x and y are planar coordinates orthogonal to the optical axis. The beam width w of the laser at a given point z along the optical axis is given by:

$$w = w_0 \sqrt{1 + \frac{z}{z_R}} \tag{1.8}$$

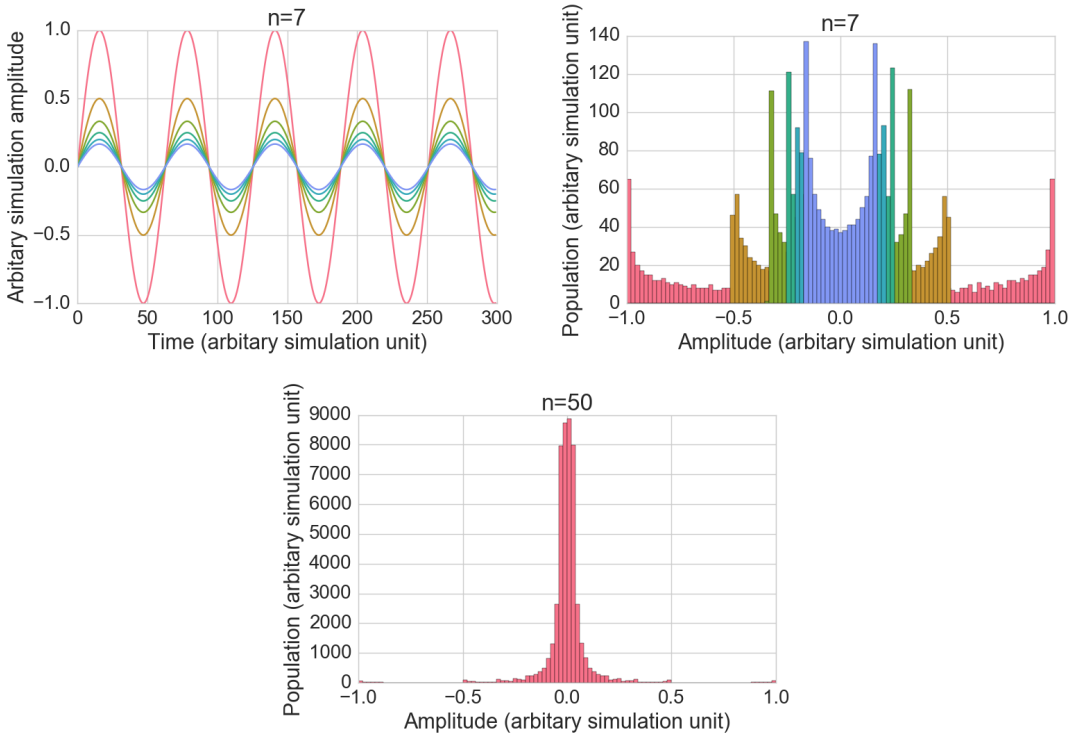

FIGURE 1.4: **Simulation:** Central limit theorem scaling gives rise to a single energetic peak despite an ensemble of motional modes with single defined amplitudes. Amplitudes of various energy levels (top left), resultant positional histogram for each individual mode(top right) and resultant histogram from summation of all the energy modes central limit theorem scaling for a high occupation number (lower).

where z_R is the Rayleigh range, given by:

$$\frac{\pi w_0^2}{\lambda} \tag{1.9}$$

where λ is the wavelength of the light. For a particle with a polarisability χ, the potential U felt in an optical field of intensity I is given by:

$$U = \frac{\chi I}{c} \tag{1.10}$$

where c is the speed of light and χ is the particles' polarisability. Substituting, this corresponds to a potential of:

$$U(x,y,z) = \frac{\chi I_0}{c\left(\frac{z^2}{z_R^2}+1\right)} e^{\frac{-2x^2-2y^2}{w_0^2\left(\frac{z^2}{z_R^2}+1\right)}} \tag{1.11}$$

This is a little more intuitive to look at in terms of forces. Thus we look at the gradient force on the particle along the z-axis:

$$F_z(x,y,z) = -\frac{2\chi I_0 z}{cz_R^2\left(\frac{z^2}{z_R^2}+1\right)^2} e^{\frac{-2x^2-2y^2}{w_0^2\left(\frac{z^2}{z_R^2}+1\right)}} - \frac{2\chi I_0 z}{cw_0^2 z_R^2\left(\frac{z^2}{z_R^2}+1\right)^3}\left(-2x^2-2y^2\right) e^{\frac{-2x^2-2y^2}{w_0^2\left(\frac{z^2}{z_R^2}+1\right)}} \tag{1.12}$$

We can see that for cases in which the displacement in x,y and z are small, the linear (first) term dominates and the particle occupies an x^2 type trap. Therefore at low displacements the system approximates a harmonic oscillator in which displacement is equal and opposite to force. For larger displacements of any spatial variable (x, y, z), the nonlinear terms will be substantial, and form the basis of the coupling mechanism used to relate the degrees of freedom in section 3.

In three dimensions, the force given by the gradient only section of the potential as a function of displacement can be given as a matrix of spring constants (or spring functions in the frequent case the oscillator is nonlinear):

$$k(x,y,z) = \begin{bmatrix} k_{xx} & k_{xy} & k_{xz} \\ k_{yx} & k_{yy} & k_{yz} \\ k_{zx} & k_{zy} & k_{zz} \end{bmatrix} \tag{1.13}$$

In which the diagonal terms k_{zz}, k_{yy} and k_{xx} denote the 3 harmonic oscillators usually present in the system. For small displacements, they can be treated as both linear and decoupled. In the case of large displacements of any spatial variable, the off diagonal terms of the matrix denote the optically enabled couplings between the degrees of freedom. k_{zx} for example giving the coupling between the z and x degrees of freedom:

$$\frac{16\chi I_0 xz}{cw_0^2 z_R^2\left(\frac{z^2}{z_R^2}+1\right)^3} e^{\frac{-2x^2-2y^2}{w_0^2\left(\frac{z^2}{z_R^2}+1\right)}} + \frac{8\chi I_0 xz}{cw_0^4 z_R^2\left(\frac{z^2}{z_R^2}+1\right)^4}\left(-2x^2-2y^2\right) e^{\frac{-2x^2-2y^2}{w_0^2\left(\frac{z^2}{z_R^2}+1\right)}} \tag{1.14}$$

This function vanishes for small values of the relevant spatial variables z and x. It's important to note that this is the motional model enabled solely by the gradient force, the contributions from the scattering term are discussed more strongly in the next chapter. Furthermore, we may freely add terms to this potential by perturbing the particle with external fields, both in time and space.

1.5.2 Optical size parameter

As mentioned previously, our silicon dioxide nanospheres exhibit high field seeking behaviour, we now provide an intuitive framework as to why this is the case.

Stable particle traps exist in a wide variety of parameter regimes and scales, with the specifics depending on the field seeking nature of the particle and the fields used to contain it. For optical field only traps one major figure of merit is the optical size parameter (x)[52]:

$$x = \frac{2\pi r}{\lambda} \tag{1.15}$$

In which r represents the radius of the object, and λ the wavelength of the interacting light. For size parameters $x < 0.1$ the object exists within the Rayleigh regime, in which it may be treated as a dipole responding the electric field of the incoming light, while when $x > 100$ the interaction of the object and light field may be treated as a ray optics problem. In both cases, an optically transparent nanoparticle, in our case silicon dioxide, exhibits high field seeking behaviour.

In the case of the dipole approximation the high field seeking nature can be attributed to the electric field of the light polarizing its charge carriers across its geometry such that the resultant distribution creates a net attractive response in the anti direction of the polarizing field. In the case of the ray approximation however, the high field seeking response results from conservation of momentum as incoming light is refracted through the particles spherical geometry. This is shown conceptually in figure 1.5.

For a 60nm silicon dioxide particle, with which the majority of experiments are conducted with in this thesis, the size parameter is 0.24, as such our system is actually just inside the Lorentz-Mie regime, intermediate between the two previously mentioned approximations.

1.5.2.1 Lorentz Mie simulations

Lorentz-Mie scattering is a method for approximately solving Maxwell's equations for optical size parameters between 0.1 and 100, in which the electric fields inside and outside the sphere are expressed in terms of spherical harmonics and used the compute the scattering and absorption of incoming plane waves of a given polarization[52]. The exact formulation of this is outside of the scope of this thesis. However as it is a solved problem, standard C libraries [53] exist for solving the optical response of objects within

the size parameters regime which converge to the Rayleigh and ray optics solutions respectively at the lower and smaller end of the size parameters. We use these C libraries to compute the scattering profile of our particle to incoming light.

Numerical computation with Lorentz-Mie scattering code indicates an 8% scattering asymmetry for a 60nm particle, 8% more light is forward scattered rather than scattering uniformly in all directions, as would be expected if the particle were completely in the Rayleigh regime. The scattering profiles of particles of various different sizes are given in figure 1.6. In the 60nm case the scattering asymmetry is relatively uniform the particle is mostly dominated by high field seeking behaviour and can be almost considered to be inside the Rayleigh limit of being treated as a dipole. However, the scattering asymmetry rises quickly as a function of size, limiting the system (or rather the trapping window of the system) to smaller sizes of particle than would otherwise be suggested by a naive analysis of the functions given in section 1.5.3.

It may be possible in future to compute a motional model from the particle entirely from Lorentz-Mie computations.

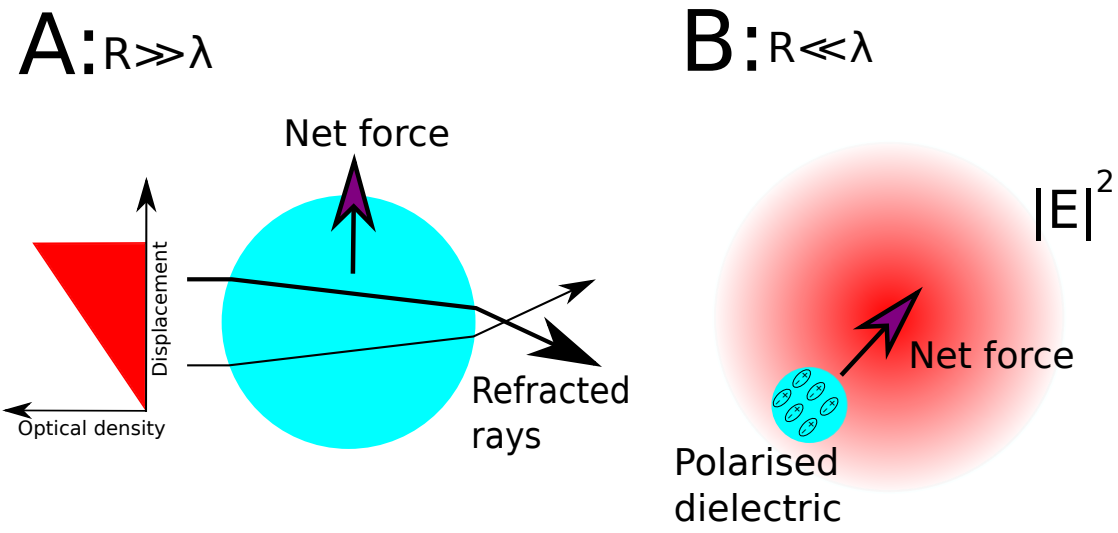

FIGURE 1.5: Conceptual diagram of gradient trapping force mechanism in ray approximation (a), and dipole approximation (b). Both mechanisms represent high field seeking behaviour. The ray approximation holds when the optical size parameter $x > 100$ and the momentum transfer to the particle is moderated by the refraction of the incoming light ray [3].. The dipole approximation for an optical size parameter $x < 0.1$, in this case the momentum transfer from the light to the particle is moderated by the electric field vector of the light [3]. For the intermediate case we exist strictly in the Lorentz-Mie regime in which the momentum transfer to the particle from the light is moderated by both the particles electric field and the net momentum conservation from the light scattered by the particle (which results in a net vector depending on where the greatest point of optical density is with respect to the particle).

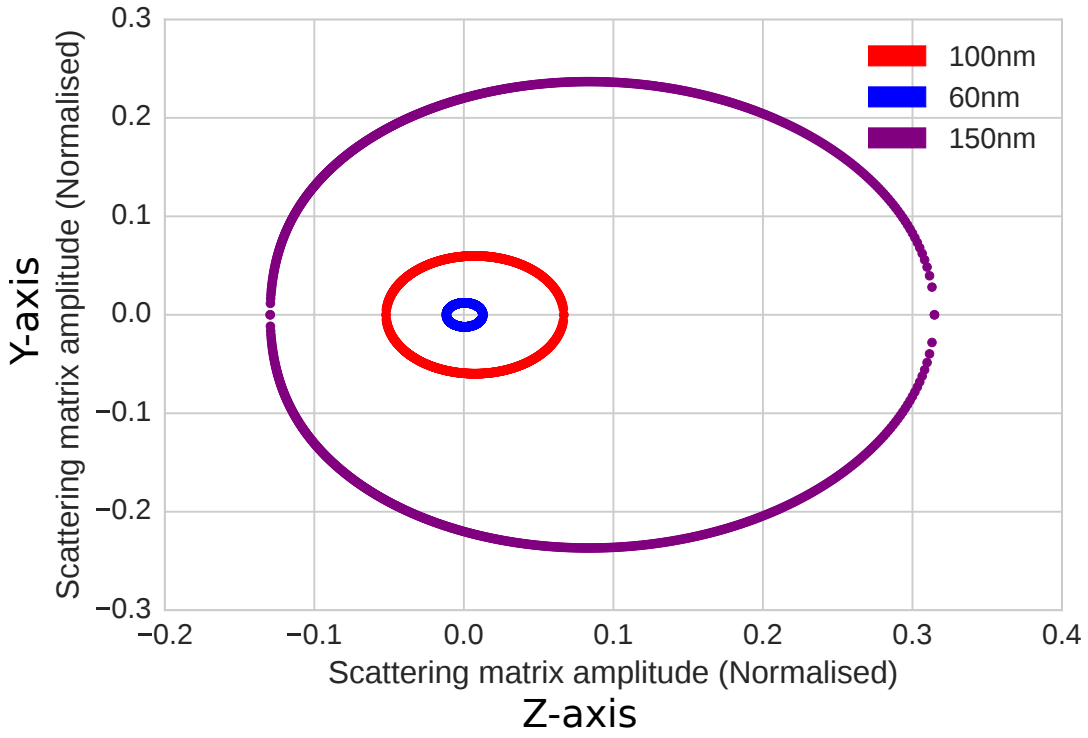

FIGURE 1.6: Mie scattering simulation for Silicon dioxide particles of various radii. Axis are the absolute values of the amplitude scattering Matrices, defined in [4], for the shown angle. Rayleigh scattering is a decreasingly good model for light scattered from the particle as the nanoparticle increases in size. In the case of true Rayleigh scatter, the scattering amplitudes would be symmetric and the function would be a circle, as is almost the case for the 60 nm particle. For particles' much larger than 60nm, it would be very inaccurate to treat the system as being in the Rayleigh scattering limit.

1.5.3 Dipole trapping approximation

Lorentz-Mie scattering is mathematically complex, as such it can be helpful to consider the particle as being in the Rayleigh limit, and as stated in the previous section (fig 1.6) this is almost true (92%) for a particle of 60 nm size.

An optical gradient trap relies on the fine balance between the radiation pressure in the direction of propagation of a focused beam of light and conservation of momentum of the light refracted through a particle present at the focus.

The scattering and gradient forces in the Rayleigh limit along the axis of beam propagation are given by [54][55]:

$$F_{scat}(r) = \hat{z}\frac{n_{medium}}{c}C_{scat}I(r) = \hat{z}\frac{128\pi^5 R^6}{3c\lambda_0^4}\left(\frac{m^2-1}{m^2+2}\right)^2 n_{medium}^5 I(r) \tag{1.16}$$

$$F_{grad}(r) = [p(r,t)\cdot\bigtriangledown]E(r,t) = \frac{2\pi n_{medium}R^3}{c}\frac{m^2-1}{m^2+2}\bigtriangledown I(r) \tag{1.17}$$

where z is the displacement vector aligned to the optical axis and r describes the distance from the center of the focus. n_{medium} gives the refractive index of the medium while m is the refractive index of the nanosphere. $p(r,t)$ is the dipole induced on the nanosphere from the electric field $E(r,t)$ of the laser, while $I(r)$ is the intensity of the lasers light field. C_{scat} is the scattering cross section of the nanosphere and λ_0 is the wavelength of the light generating the optical trap. R is the radius of the particle. Under the conditions listed below, these two forces give rise to a stable potential. Note that the gradient derivation is the same as that in section 1.5.1 but the polarisability term expanded using the Clausius - Mossotti relation:

$$\chi = \frac{3\epsilon_0}{N}(\frac{\epsilon_r - 1}{\epsilon_r + 2}) \tag{1.18}$$

χ being the particles' polarizability, ϵ_0 the permittivity of free space, ϵ_r the dielectric constant of the particle and N its number density.

The following main conditions must be fulfilled in order for a particle to be trapped by the optical intensity maxima:

1. Gradient force must overpower the scattering force in the negative direction of the beam propagation.
2. Trapping time must be less than the time for Boltzmann / Brownian motion to remove the particle from the trap.
3. Kinetic energy of the particle must be less than the potential of the optical trap.

The trap is, in an ideal case, conservative - the momentum/energy of a particle passing through it should remain unchanged (entry to exit) on the condition that the particle has enough initial momentum to clear itself of the energy well. This sets a limit on the maximum kinetic energy that a particle may possess to be captured by the trap, defined by its depth. This sets limits on capturing nano-particles from kinetically violent sources like piezo - electrics or other non - thermalised sources. Many experimental groups use buffer gases to reduce the kinetic energy of their nanoparticles to be low enough to be trapped, and the development of an ultra high vacuum (UHV) compatible source with a high yield, low trapping time and particle charge control remains a major experimental hurdle for the entire field at present. The development of such a source may likely prove critical to proposals for high mass matter wave interference [56] and creating quantum superpositions in space [57].

In contrast the trapping mechanism in our setup relies upon thermalisation of the nanoparticles in solution with the surrounding air, such that a significant proportion

of the nanoparticles velocity distribution is within that of the optical trap depth (the ballistic velocity of the nanoparticle solution leaving the nebuliser before the thermalization process is significantly higher). Trapping via this thermalization mechanism limits the starting pressure in the system to that where the nanoparticle behaves as a particle undergoing a biased random walk in a potential rather than behaving like a driven damped oscillator. Experimental evidence indicates the this regime to above approximately 10 mbar [58][10].

1.6 Motional response to applied forces

1.6.1 Perturbation of the particles motion in the linear regime

While the particle is acting linearly, with respect to its differential equation of motion, we might expect the displacement of its centre of motion to be proportional to the applied force, as in the case for a driven damped oscillator:

$$|z_0| = \frac{F_0}{\sqrt{(-m\omega^2 + k)^2 + (\gamma\omega)^2)}} \tag{1.19}$$

In which z_0 is the displacement induced by the additional driving force. We can also obtain the result for a constant force in time by taking the limit for $\omega \to 0$

A limitation of this result is that the driven damped model assumes constant damping and driving at a single frequency. It is also a poor description of what happens to our particles' motion when the applied force varies significantly in space over the characteristic dimensions of the trap.

1.6.1.1 Force sensitivity in linear regime

In terms of using a levitated particle as a test mass, for either force sensing or fundamental physics applications, the desired parameters for sensitivity can be revealed by looking at the minimum detectable force visible for an oscillator in a thermal bath: [59]

$$F_{min} = S_F^{1/2} b^{1/2} = \sqrt{\frac{4k_B T b K}{\Omega Q}} \tag{1.20}$$

where S_F is the force spectral density, b the measurement bandwidth, K is the spring constant of the oscillator system and, T its temperature, Q the quality factor of the

oscillator $Q = \frac{\Omega}{2\alpha}$, where α is the attenuation rate of the oscillation. Ω is the natural frequency of the oscillator and k_B is the Boltzmann constant.

The immediate implications of this being that a high Q factor, high natural frequency and low external temperature are all important parameters to engineer into a highly sensitive levitated test mass if sensing applications are held in mind.

1.6.2 Motional response in the non-linear regime

1.6.3 SDE (Stochastic differential equation) approach

Since linear approximations of our system evidently break down fairly quickly, it is therefore a better description of the system think of the particle as a stochastic differential equation evolving in a potential, to obtain a more complete match between theory and experiment.

In one degree of freedom, our system is generally well described by the stochastic differential equation:

$$m(\ddot{y} + \gamma\dot{y} + \Omega^2 y) = \eta(t) + F(x,t) \tag{1.21}$$

In which γ represents the velocity coupled viscous damping, Ω the natural frequency of the particle as it oscillated in the trap defined by the driving laser field, $\eta(t)$ Gaussian white noise, m the particles mass and $F(x,t)$ describes the effect of external fields, such as gravity, electrostatic or additional fields applied to the particle, aside from the standard Gaussian focus.

The assumption of using a model of white noise for the random field is examined further in Appendix A.2, where it is found that the particles interactions with background gas collisions do reasonably approximate white noise.

Solving such an SDE computationally is a commonly studied problem through such methods as Euler-Maruyama[60] and stochastic Runge-Kutta[61], and is used frequently to match theory to experiment in later sections.

1.6.4 Langevin Approach

If the external fields are constant in time, then the external force can just be thought of as deforming the particles potential. In this case the system can be more generally defined by a Langevin equation:

$$\frac{dx}{dt} = -\frac{1}{\gamma}\frac{\partial V}{\partial x} + \sqrt{2D}\eta(t) \tag{1.22}$$

In which V is the potential occupied by the particle, γ its environmental damping and D its diffusion constant, set by the shape of the particle.

In the case that the suspended oscillator is in a heat bath of sufficient damping (in relation to the driving term) to be treated as though it is thermodynamic equilibrium, then the potential the particle is in can be directly extracted from its positional distribution, see Appendix B.

In both the stochastic differential equation (SDE) approach or the Langevin equation approach, the outcome can be computed for matching experimental outputs with theoretical potentials. In the case of the Langevin equation this is an analytical solution whereas the SDE is required to be solved numerically.

When $y << d$ where y is the extent of the particles motion and d is the characteristic distance over which the external force varies significantly, then the same linear result for an applied force is recovered as in the case of the driven damped oscillator in a harmonic potential (section 1.6.1). In the case where $y \approx d$ or $y > d$ then the system can no longer be treated as a driven harmonic oscillator and the resultant motion of the system in response to an applied force has to either be computed numerically as an SDE or solved as a steady state solution to a Langevin equation in a potential.

Both the SDE and Langevin approaches are applicable to the particle in its linear and nonlinear motional states, both assuming a random background field and linear damping. The Langevin solution also assumes thermodynamic equilibrium. From the definition of an ensemble in this case thermodynamic equilibrium should always be recovered for the particle when $t \to \infty$ for a random background field [37]. The equivalence between the two methods is exploited later as a method to recover the particles mass and could in principle be used as an equilibrium test for thermodynamics experiments.

1.6.5 Particle force response, linear and non-linear regimes - example

An example from experimental data is given in figure 1.7 in which a $\frac{1}{r^2}$ type spatial potential constant in time is varied in the case of both; being far enough away from the particle that it approximates a constant force over space and, being close enough such that potential varies significantly over the length scale of the trapped particle. The potential for each case is reconstructed from experimental data by the methods given in section 1.7.1.

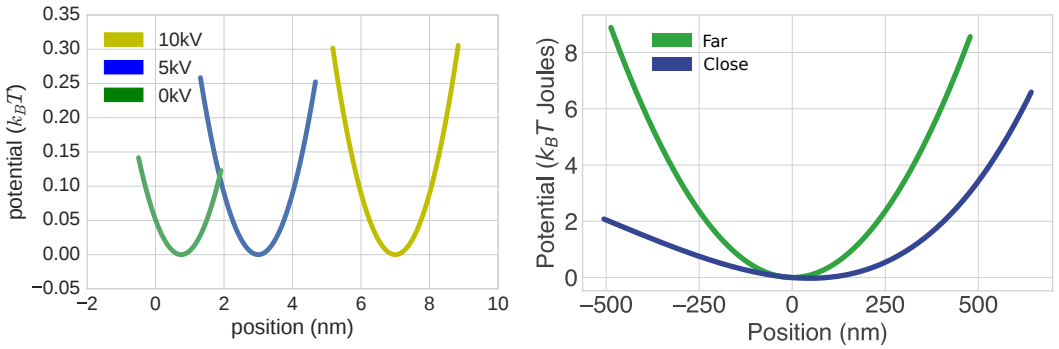

FIGURE 1.7: **Experimental data** Left: Effective potential for a levitated nanoparticle in linear regime responding to a constant force, applied by an electric field - the strength of which does not vary significantly over the length scale of the optical potential. Right: Effective potential for a nanoparticle responding to a Coulomb force that varies substantially over the length scale of the trapping potential.

1.7 Common methods

1.7.1 Potential Extraction (from experimental data)

The potential $U_{steadystate}$ computed from the steady state solution to a Langevin equation of a particle in thermodynamic equilibrium with a random background field undergoing a random walk in a potential:

$$U_{steadystate} = \frac{k_B T}{\gamma} ln(\rho(x)) \tag{1.23}$$

where γ is the damping constant of the damped harmonic oscillator describing the motion of the particle in the trap. At pressures above 10^{-8}mbar [10] the foremost damping effect comes from random kicks of background gas particles with the trapped particle at thermal equilibrium with the environmental temperature at 300K. $\rho(x)$ represents the position distribution of the trapped particle. On the other hand the potential $U_{Dynamic}$ extracted experimentally from the time trace of the motion of the particle in the trap according to:

$$U_{Dynamic} = \int F(t) \cdot dx + c \tag{1.24}$$

where c is a constant of integration, and $F(t)$ is the total time-dependent force acting on the particle. It is important to note that this method of reconstructing the potential does not require the particle to be in thermodynamic equilibrium. $F(t)$ is computed by

taking the finite difference with respect to twice the particles time trace and multiplying it by the particles' mass.

Computing the spring functions and thus potentials of the oscillator for a variety of trapping powers produces an unsurprising result, the gradient of the spring function scales with power and the reconstructed potentials look like x^2 potentials, in which the gradient of the x^2 function also scale with power, figure 1.8.

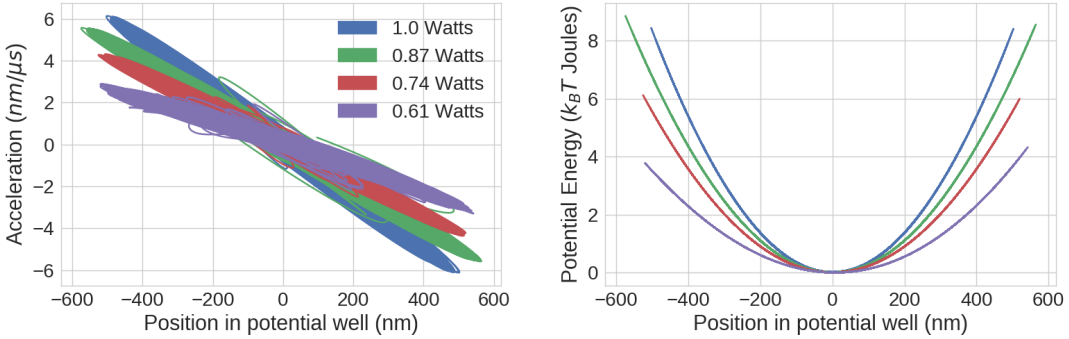

FIGURE 1.8: Acceleration - position or spring functions for different laser powers, along with the potentials obtained by integrating them.

1.7.2 Particle mass extraction

Since the finite differencing of the particles' time trace, gives acceleration rather than force, we extract $U_{kinematic}/m$. Thus, on the assumption that the particle is in thermal equilibrium, we equate the two potentials and make mass, m, the only free fitting parameter in the equation:

$$U_{steadystate} = U_{Dynamic}/m \tag{1.25}$$

We then extract the radius r from the mass m on the assumption that the particle is spherical and that the particles volume follows the relation:

$$V = \frac{4}{3}\pi R^3 = \frac{m}{\rho} \tag{1.26}$$

where V is the particles volume, m its mass and ρ its density, for which we use the value 2200 $\frac{kg}{m^3}$.

The assumption of a spherical particle is supported by the particles motional degrees of freedom being generally uncoupled from each other at low pressure, close to the centre of the trap where the x^2 approximation of the Gaussian potential remains true. The

comparison of the two potentials, $U_{steadystate}$ and $U_{Dynamic}$, is shown in figure 1.9, and we extract a particle radius of r = 60nm (+/- 5nm) for the particle used in the figure. The error bar of the mass is derived from the fitting error.

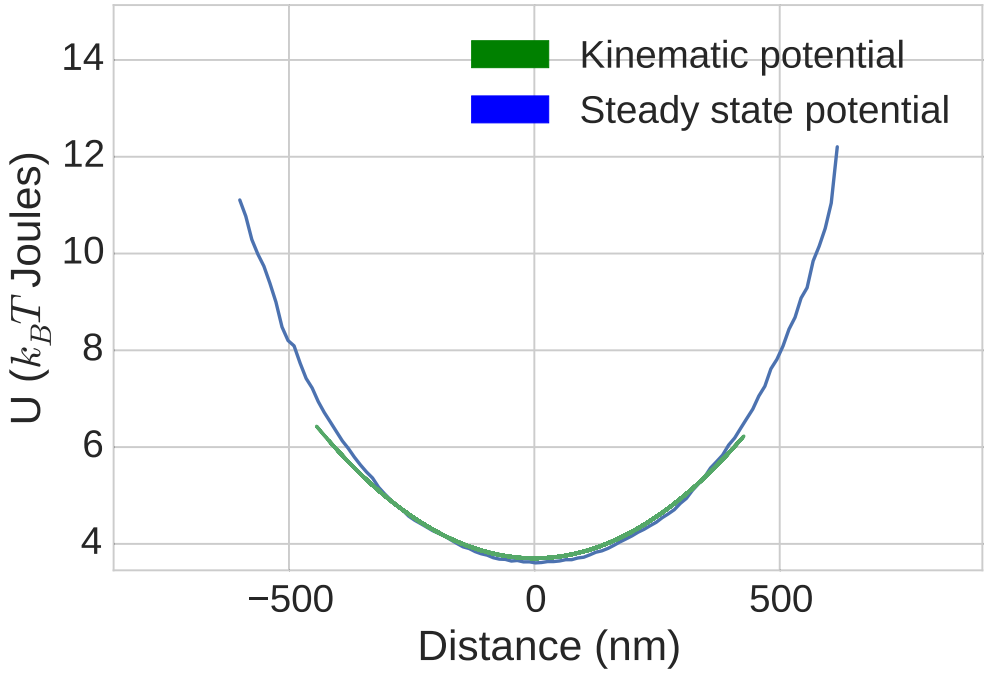

FIGURE 1.9: **Experimental data:** The steady-state, according to equation 1.23, and the kinematic, according to equation 1.24, potentials are fitted to each other with the mass of the particle as the only free parameter. In this way the mass of the particle is extracted from the measured data directly without assumptions otherwise used.

1.7.3 Instantaneous particle energy

The temperature or mean occupation number of the oscillator can be easily computed by fitting a Lorenztian function to the PSD of a degree of freedom of the particles' motion. This however requires both enough datapoints to perform a Fourier transform and for the particle to have experienced enough modes of the heatbath for the particle to be said to be in equilibrium, the strict definition of this is $t \to \infty$ [37], however in practice smaller times are required, as demonstrated in section 1.8.1 and figure 1.11.

It is therefore necessary to be able to compute the energy of the particle at an instantaneous time in its motion, if the energetic dynamics of the particle are to be studied on smaller timescales. As the motion of the particle manifests as a classical test mass undergoing motion we can know a priori from the methods in 1.7.1 this is a trivial task:

$$Total\ energy = Potential\ energy + Kinetic\ energy \tag{1.27}$$

where the potential energy can be computed from equation 1.24 and the kinetic energy from:

$$Kinetic\ energy = \frac{1}{2}m\frac{\partial^2 x}{\partial t^2} \tag{1.28}$$

where m is the particles mass, x its position and t the time at which that measurement of the particle position was taken.

While this might seem completely trivial, it was only recently that such measurements of the particles' kinetic energy were essential to one of the fields first demonstrations of detection of gravitational-nanoparticle interactions [62], and such a method provides a valuable tool to explore the particle dynamics beyond just looking at the frequency domain. An example of the particles energy fluctuating over time is given in figure 1.10.

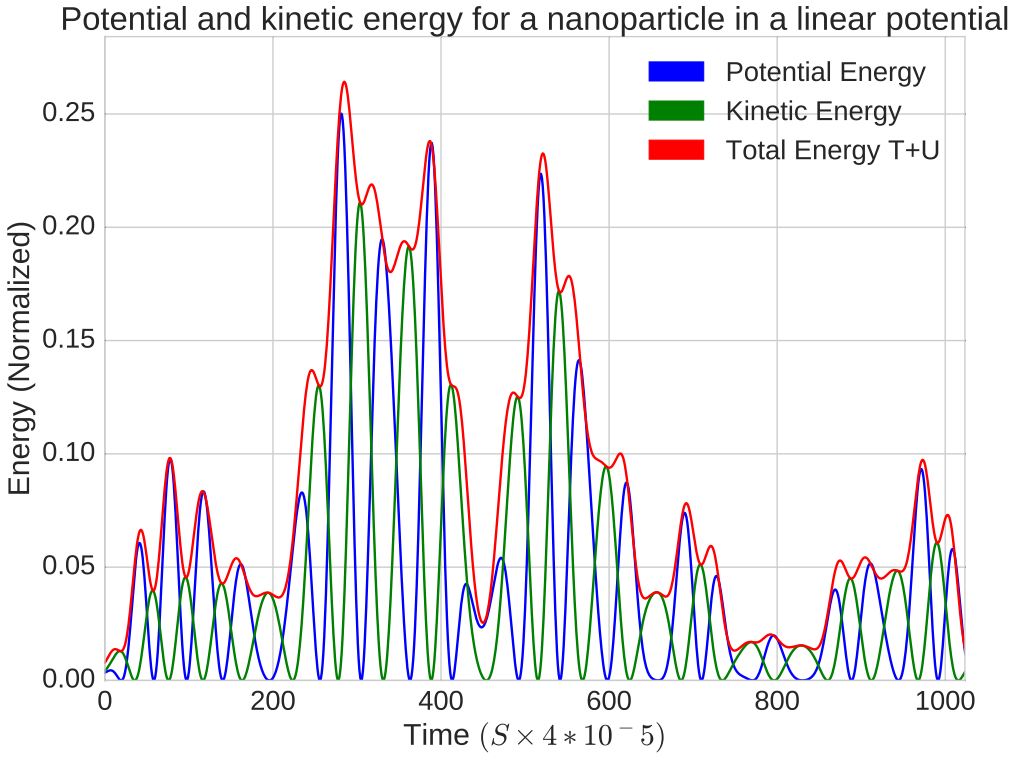

FIGURE 1.10: **Experimental data:** The instantaneous total energy of a levitated nanoparticle in an optical trap at 10^{-2}mbar, significant fluctuations in the total energy of the nanoparticle are observed due to random heating and cooling from background gas collisions at this pressure.

1.8 Experimental limit of thermal equilibrium

1.8.1 Heat bath quality

From the method given in section 1.7.3 we can compute the energy of the particle for an instantaneous moment in time.

The rate of change of the instantaneous energy of a trapped particle was computed for various integration times and laser powers, figure 1.11. For thermal equilibrium the histogram of such a quantity should be symmetrical, as the flow energy into the system should be equal to the flow of energy out of the system. However, for adequately low laser powers and integration times it is not.

The time taken for the histogram of the rate of change of the particle's energy to become Lorenztian can be considered to be the time taken for the particle to experience all states of the heat bath, or alternatively the maximum time for the particle to completely thermalise.

While a long thermlisation time at high vacuum would be unsurprising, the tendancy of the particle to experience a poor heatbath can be made to exist at surprisingly macroscopic times even when it is at a pressure representative of thermal equilibrium. 0.1 seconds at 10^{-2} mbar.

The implication being that we may be able to access a wide range of temperatures at which to perform thermodynamic cycles without the use of an AOM (acoustic optical modulator) or other fast method of time series beam modulation.

1.9 Particle detection

For the vast majority of this thesis the particles motion is detected by interference of light that does and does not interact with the particle respectively, the detection function is discussed at length in papers such as [38]. The interference function this generates varies significantly over space, requiring alignment of the detector to the motional peaks of interest for the desired experiment. The experimental implications of this are discussed at further length in section 3. The detection efficiency of the z peak of motion as a function of distance is reproduced Appendix I for limited values of distance.

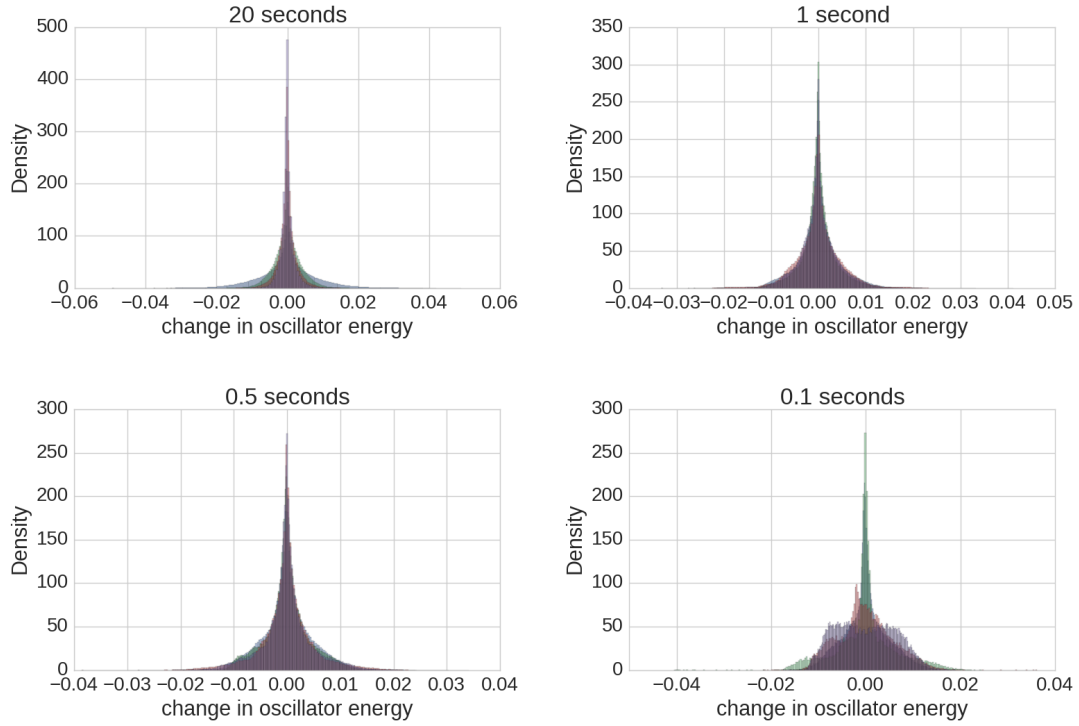

FIGURE 1.11: **Experimental data:** Histogram rate of change of the particles total energy (KE+PE) with respect to time. For long time scales (>0.5 seconds), the particle has experienced all the energy modes of the heatbath and be considered to be in thermodynamic equilibrium. Data taken at 10^{-2} mbar. Laser powers are respectively 1 Watt (green), 0.75 Watts (red) and 0.5 Watts (purple). The variation with power is unsurprising since a slower moving (lower power $\rightarrow$ lower frequency $\rightarrow$ lower velocity) particle will take longer to experience all of the heatbath modes.

1.9.1 Photons-Volts-Meters conversion factor

When the particle is inhabiting a linear trap in thermal equilibrium, this is often achieved by fitting a Lorentzian function the motional peak of one degree of freedom of the particle in the frequency domain[63]:

$$S_{ii}(\omega) = \frac{\alpha_i}{((w_i^2 - w^2) + \omega^2\Gamma_i^2)} + \beta \tag{1.29}$$

In which ii refers to the degree of freedom of the nanoparticle the Lorentzian is being fitted to, ω the frequency, Γ the damping on the degree of freedom, and α and β are fitting parameters. This allows for the extraction of the Volts/metres conversion factor[64]:

$$C^i_{calibration} = \sqrt{\frac{\alpha^i(y)\pi m}{\Gamma k_B T}} \tag{1.30}$$

where m is the mass of the nanoparticle (determined previously through the method in section 1.7.2), T is the particles' temperature, α the fitting from the Lorentzian and k_B is the Boltzmann constant.

It it important to note here that, in contrast to some of the earlier available literature on the subject, the calibration function is a function of displacement from the centre of the trap, rather than just a scalar number.

1.9.2 Conclusion

In conclusion while the optically levitated nanoparticle system is physically complex to fully model, a great deal of the physics that occurs within the system and thus the experimental results within this thesis can be understood somewhat intuitively with the tools presented within this chapter. More specific tools are presented in the following chapters themselves when relevant to the results found within this thesis.

Chapter 2

Surface dispersion interactions

2.1 Chapter overview

In this chapter we will describe the motivation of using a trapped nanosphere to detect surface dispersion forces, briefly detail the theoretical model used to understand the motion of the particle near to a surface and under the influence of perturbing forces, and discuss our experimental results. Finally, we will discuss outlook for future experiments.

2.2 Motivation

A charged particle near a neutral surface will experience an attractive short-range force due to the interaction with its image charge [65][66]. Even when the object brought close to the surface is neutral, forces between the two objects will be effected by correlations between the fluctuations of atomic dipoles that make up two spatially-separated bodies — these are dispersion forces, known as the Casimir force [67] for two macroscopic objects; Casimir-Polder if only one of them is microscopic (atom, molecule, nanosphere, etc) [67][68]; or Van der Waals forces if both objects in the interaction are microscopic[68]. This is shown conceptually in figure 2.1.

These effects are all conceptual regimes in a system of short range physics that exists as a continuum. Clearly parameter spaces exist where several of these forces are relevant at once, and indeed, it is possible to derive the Casimir and Van der Waals forces from each other [68].

A model system in which to study short-range forces is two closely-spaced objects separated by vacuum, as depicted in figure 2.2, where the particle-surface interaction is

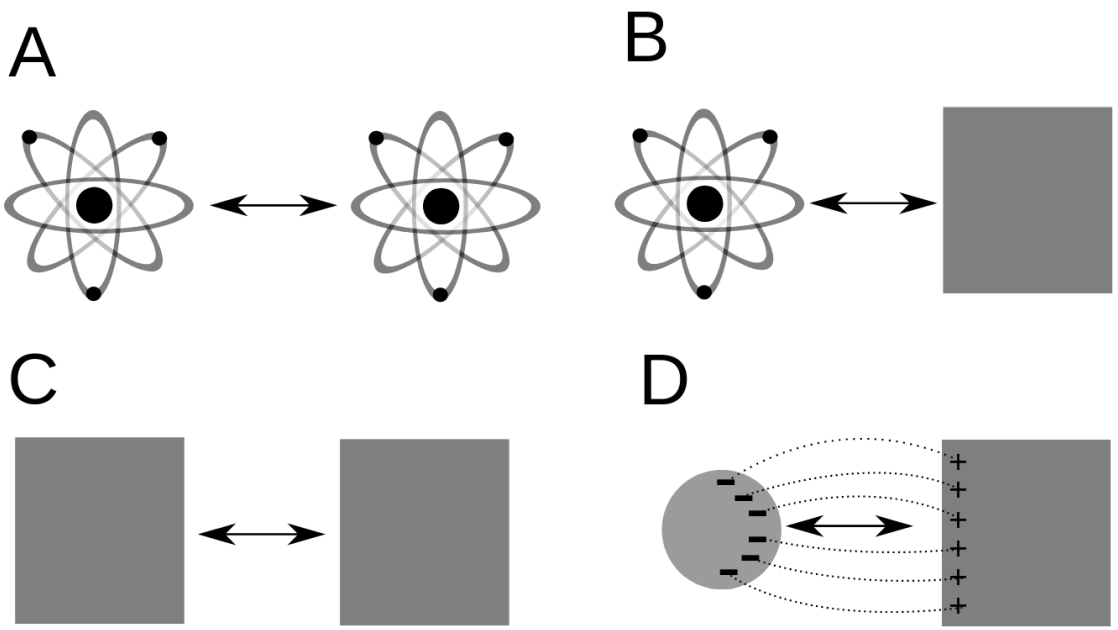

FIGURE 2.1: Conceptual differences between A) Van der Waals, B) Casimir-Polder, C) Casimir and D) Coulomb forces from the method of images charges.

probed for varying distances. Over the years a variety of experiments have been performed with different physical systems (e.g. torsion pendulums [69], cantilevers, and tip probes [70]) to investigate surface forces. Several experiments that utilize controllable cold atoms have been performed to measure Casimir-Polder and Van der Waals forces close to an uncharged surface [71–74]. A levitated nanoparticle seems a obvious candidate with which to conduct similar experiments.

Due to the lack of clamping losses, a levitated nanoparticle should in principle be a equivalent or higher sensitivity test mass to probe interactions such as a Van-der Waals interactions and Casimir forces than the tip of an Atomic Force Microscope (AFM)[75]. While it is unlikely that a levitated nanoparticle will achieve a higher coupling to surface details than a system such as a scanning tunneling microscope (STM) in the absence of quantum state preparation, its mass and Q factor exist in a section of the parameter space not easily accessed by other systems, potentially allowing for interesting tests of fundamental physics as well as coupling to other resonator systems.

Due to the trapped nanoparticles extremely high Q factor and positional resolution at low pressures, the particle is in both theory and practice an excellent detector for forces in the mesoscopic regime. Q factor can be defined as:

$$Q = \frac{f_{resonant}}{\Delta f} \tag{2.1}$$

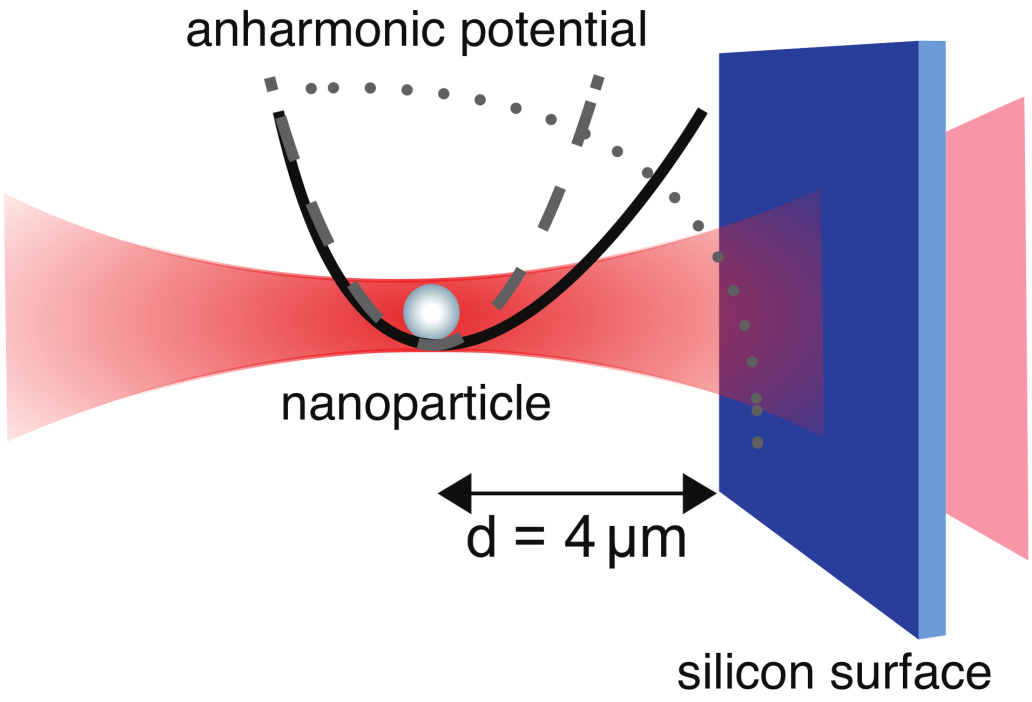

FIGURE 2.2: Schematic of the experiment. The particle is optically trapped close to the surface at various particle - surface distances d (experimentally d can be varied between hundreds of microns to whatever distance the dispersion forces overwhelm the optical trap - typically in the region of a small numbers of microns). The distance is varied by moving the surface on a 3 axis stage while the optical focus of the parabolic mirror, and thus the nanoparticle, remains fixed.

where $f_{resonant}$ is the natural frequency of the oscillator and Δf is the resonance width. This is equivalent to:

$$Q = 2\pi \cdot \frac{\text{energy stored}}{\text{energy dissipated per cycle}} \tag{2.2}$$

With experimental Q factors of 10^{12} being predicted in the literature for particles at high vacuum [18], leading to force sensitivities in the zeptoNewton (10^{-21}) range [18][10].

The detection scheme in our experimental setup grants a positional resolution limit of around 10 picometres[47]. As such it is possible to use it to detect extremely small forces[18] and many force sensing proposals have by given in the optomechanics community [76][10].

Proposals in the optomechanics community have already been made to detect short ranges forces using a levitated mesoscopic particle in both the classical limit [77][76] and with quantum states of the particle that have yet to be experimentally demonstrated in the system [75].

2.3 Dispersion forces

Dispersion forces are defined [78] as 'Effective electromagnetic forces acting between well separated neutral, unpolarised and unmagnetised atom or bodies in the absence of any applied electromagnetic fields'. This definition encompasses van der Waals, Casimir-Polder and Casimir forces[78][79]. The specific terminology of each case usually indicates atom-atom, atom-body and body-body forces respectively[78][79]. The differences are demonstrated visually in figure 2.1.

Furthermore it is important to define the non retarded and retarded distance regimes, the latter of which refers to scales in which the speed of light becomes relevant to the interactions. The retarded regime occurs as the time taken for the field sources to switch states is no longer smaller than the time for two separated field sources to receive information from each other.

In this case we operate in the time retarded thermal regime in which the separation between the levitated nanosphere and the flat surface is large enough that communication of information between the two bodies cannot be treated as instantaneous, and both bodies have an internal temperature above absolute zero. The characteristic distance scale of this experiment is a small number of microns. The particle is also likely to have an arbitrary and unknown charge interacting with its mirror charge in the silicon surface. In the literature this is often termed the macroscopic theory of Van der Waals forces.

The specific balance of distance, charge and temperature of the bodies interacting is of critical importance on the micro-scale, not just for the amplitude of the forces experienced by the actors of system but also the force characteristics. For specific values of the parameters space dispersion forces can exert a net repulsion [77]. These exotic effects are however likely to require specific geometries of test particles such as being non-spherical and a controllable, known rotation. This have been observed by several experimental groups [39], experimentally generating repulsive Casimir forces in such a setting may therefore be feasible in the near future.

2.4 Theoretical motional model of a levitated particle in a dispersion field.

2.4.1 Unpeturbed particle

At large distances from the surface, where the surface is not affecting the oscillation of the particle, the levitated nanoparticle is trapped optically in the focus of a Gaussian laser beam in the Rayleigh limit, within an optical harmonic potential $U_0(x) = (k/2)x^2$, where x is the spatial displacement of the nanosphere while oscillating, and k is the spring constant, which for the optical trap is originated by the optical gradient force and therefore $k = 2\alpha P/(c\pi\epsilon_0 w^6/\lambda^2)$, with α being the polarisability of the nanoparticle, P the incident laser power, c the speed of light, ϵ_0 the permittivity of free space, w is the laser waist at focus, and λ the wavelength of the laser. Here we only consider the one-dimensional z-motion of the particle normal to the surface. More details about the optical trap can be found elsewhere [80] and section 1.5.1.

2.4.2 Expected surface potential for a charged particle

The potential of a charged particle interacting with its image charge $U_{\rm ic}(d)$ in a dielectric substrate with a layer of thickness L deposited on top is [65]:

$$U_{\rm ic}(d) = -\frac{Q^2}{4\pi\epsilon_0}\frac{1}{2}\int_0^\infty dz \frac{R_{01} + R_{12}e^{-2zL}}{1 + R_{01}R_{12}e^{-2zL}} e^{-2zd}, \tag{2.3}$$

with $R_{01} = (\epsilon_1 - 1)/(\epsilon_1 + 1), R_{12} = (\epsilon_2 - \epsilon_1)/(\epsilon_2 + \epsilon_1)$, where ϵ_1 and ϵ_2 are the permittivities of the layer and the substrate respectively. Q is the charge of the particle and d is the distance between the nanoparticle and the vacuum-layer interface, and z is the integration variable. Close to the surface the particle will explore a total potential $U_t(d)$ defined by the superposition of the surface interaction potential and the optical potential, $U_{\rm t}(d) = U_{\rm ic}(d) + \frac{1}{2}k(x-d)^2$.

This regime of a charged body interacting with its image charge on a dielectric plane is referred to as the Lifshitz theory of Van der Waals forces or alternatively the macroscopic theory of Van der Waals forces[79][78].

2.4.3 Comparison of optical and Coloumb forces

Assuming the nanoparticle is thermalised at 300 K and that the energy in the motional axis of the nanoparticles' motion can be computed from the equipartition theorem:

$$< E >= \frac{3}{2} k_B T \tag{2.4}$$

The trap depth for reasonable laser powers is plotted against the the surface potential energy in figure 2.3. Furthermore, as well as looking at the picture in terms of energy, we can compare the relative strengths of the optical and Coloumb fields in terms of force, with the force on the particle at a variable position in a harmonic trap given by [81]:

$$F_{trap} = \omega^2 \times m \times displacement, \tag{2.5}$$

where m is the mass of the particle and $\omega = 2\pi f$ is the angular frequency of the particles' motion. This equation is also plotted alongside equation 2.3 in figure 2.3. We can see that the surface potential is a significant contributor to the total energy of the nanoparticles motion in the tens of microns range depending on the optical trap depth and charge state of the particle.

With the comparison of forces made in the case of a charged particle, we now examine the case of an uncharged surface.

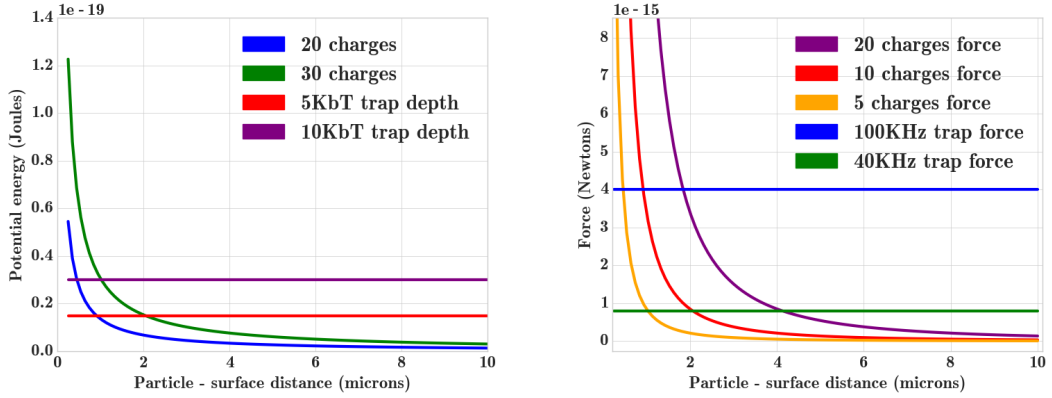

FIGURE 2.3: Left: expected surface interaction potential for particles of various charges a distance d away from a an Si/SiO_2 interface. Right: attractive force applied to the charged particle by its mirror charge interaction with the surface. The Surface Coulomb force will likely overpower the optical trap for a reasonable number of charges while close to the surface. Its important to note that, due to the presence of significant thermal fluctuations in the particle's kinetic energy due to background gas collisions that the required force required to remove the particle from the trap.

2.4.4 Expected surface potential for an uncharged particle

Aside from the Coulomb potential, the nanosphere experiences a dispersion force arising from correlations between the fluctuations of its own atomic dipoles and those in the

surface. Here, the nanosphere is far enough away from the surface that it can be considered as a point dipole, with polarisability $\alpha(\omega)$ obtained from the Clausius-Mossotti relation [82] for a sphere of radius R and permittivity $\epsilon(\omega)$ to be:

$$\alpha(\omega) = 4\pi\epsilon_0 R^3(\epsilon(\omega) - 1)/(\epsilon(\omega) + 2). \tag{2.6}$$

In the Appendix we present numerical results for the Casimir-Polder potential for a wide range of distances, however in order to gain a simple and useable formula we note that the nanoparticle-surface distance (4-11 μm) is large compared to the wavelength of any of the dominant transitions in the optical response of either of the materials (70 nm for SiO_2 and 265 nm for Si). Thus we are in the retarded regime, where the Casimir-Polder potential has the form [83][68];

$$U_{\mathrm{CP}}(d) = -\frac{C_4}{d^4} \tag{2.7}$$

where C_4 is a distance-independent constant defined as [84][68];

$$C_4 = \frac{3\hbar c\alpha(0)}{64\pi^2\epsilon_0}\int_1^\infty dv \left(\frac{2}{v^2} - \frac{1}{v^4}\right)\frac{\varepsilon_1(0)v - \sqrt{\varepsilon_1(0) - 1 + v^2}}{\varepsilon_1(0)v + \sqrt{\varepsilon_1(0) - 1 + v^2}} \tag{2.8}$$

Using the measured optical data for silicon and silicon dioxide presented in the Appendix as tabulated in [83], we find a value of; $C_4 = (7.60 \times 10^{-28}\mathrm{Jm}) \cdot R^3$. In the following we compare the data to the trapping and Coulomb potentials U_{ic} and U_0.

Thus, for a sphere plane geometry, the Casimir-Polder potential U_r for a neutral silicon dioxide particle significantly larger than an atom approaching an infinite neutral dielectric silicon plane surface in the time retarded regime is given by [78][79]:

$$U_R(z) = -\frac{C_4^{Si-SiO_2}}{z^4} = -1.11 \cdot 10^{-27} \cdot \frac{R^3}{z^4} \tag{2.9}$$

where $C_4^{Si-SiO_2}$ is the dispersion constant for the silicon - silicon dioxide interaction in the time retarded regime, which determines the strength of the surface interaction for all variables in the system except for distance between the objects, and is derived in Appendix E. R is the radius of the sphere and z is the distance from the sphere to the surface.

2.4.5 Comparison of charged and uncharged particle surface forces

The potentials for charged and uncharged particles near a neutral planes are plotted comparatively in figure 2.14.

The Columb interaction is significantly stronger than Casimir-Polder forces alone in the distance regime of a small number of microns, as demonstrated in figure 2.14. Given the scaling of the Casimir-Polder forces in this distance regime in the comparison to Coloumb interactions from net charges, figure 2.14. As well as the frequency of trapping charged particles (a significant proportion of particles appear to be charged from the nebuliser source). It seems likely from the fitting the expected relations for a charged and uncharged particle to the experimental data that the particles displaying strong surface-particle interactions in the experimental data are in fact charged, and the force of the particle surface interaction arises from the interaction of the particles net charge and its mirror on the silicon surface.

However, it does not seem unreasonable to in principle observe genuine Casimir-Polder forces in the experiment in the future, based on theoretical computations of the predicted Casimir-Polder potentials for particles of our sizes, figure 2.14, and the particle-surface distances obtained later in the experiment, however based on our current force sensitivity limit it would require trapping larger particles than present and for any stray charges on the particle to be neutralized (charge control of a levitated nanoparticle has been demonstrated in [85], charge may be determined experimentally through the methodology described in [47]).

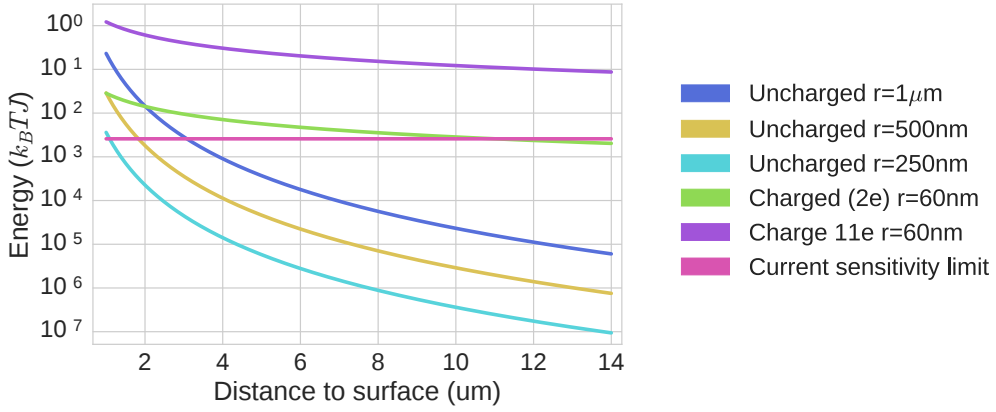

FIGURE 2.4: **Simulation:** Comparative potentials of various particle sizes, charged and uncharged, in comparison to the experimentally obtained sensitivity limit of the system. The surface-particle force from a charged particle is dramatically more than the force from an uncharged particle, unless the particle is of substantial size.

2.5 Experimental methods

2.5.1 Experimental methods - setup

Initially experiments were carried out by optically modulating the particles motion by controlling the divergence of the input beam into the mirror (Appendix L.0.4). While this approach gives a large degree of control over the position of the potential well in which the particle resides in the z axis, it also generates a periodic potential, which rapidly gives rise to double and triple well periodic potentials, discussed in section 4.3.1, where a more detailed discussion of non linearities and bespoke potentials is given.

It was discovered by trial and error that moving the stage rather than the particle caused less disruption to the systems optics, and was thus adopted as the means of changing the particle surface distance to explore the potential.

The setup consists of a 60 nm radius dielectric nanosphere trapped in the focus of a high NA (0.9) parabolic mirror consistent with the methods employed in [80], with trapping laser wavelengths and power of 1550nm and 1 Watt respectively. The experiment is conducted at a pressure of 10^{-2} mbar. A top down schematic view of the optical setup given in figure 2.6. A 3-axis micrometer stage is used to vary the distance between a 200μm thick n-doped double sided polished silicon planar surface and the optically defined nanoparticle trapping site.

2.5.1.1 Potential extraction for each stage position - piecewise potential reconstruction

The surface is moved in discrete intervals, decreasing the distance between it and the levitated particle. At each discrete interval of stage movement the nanoparticles' motion is recorded via the same homodyne-like detection scheme utilized in [80] in which the phase shift between the light that interacts with particle and the light that does not effects an interference corresponding to the particles position. At each of these discrete sites (plotted in figure 2.7), the nanoparticles' oscillatory motion naturally explores a region of several hundred nanometres, with the exact distance being determined by the potential stiffness. This allows us to reconstruct the overall surface potential in piece-wise steps, with the individual extracted steps shown in figure 2.13 and the piece-wise reconstruction given in figure 2.15.

Naturally, the potential we extract directly from the experimental data will be a super-position of the optical trapping potential and the potential from the surface dispersion forces from the interaction of the particle and surface.

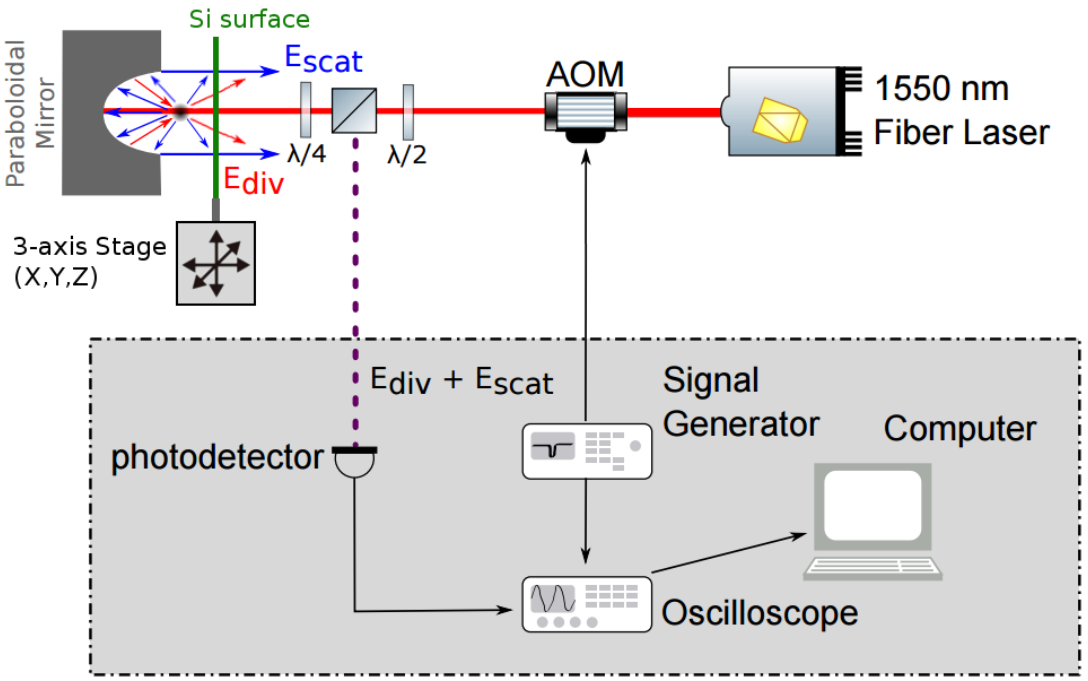

FIGURE 2.5: **Experimental setup.** A fibre acousto-optical modulator (AOM) is used to modulate the light coming from a 1550nm fibre laser, which then passes though a $\frac{\lambda}{2}$-wave-plate, a polarizing beamsplitter (PBS) and a $\frac{\lambda}{4}$-wave-plate before passing through the Si-surface. The Si-surface is mounted on stage in order to be moved in space in all three degrees of freedom. The total distance d of the surface to the nanoparticle is varied between $2\mu m$ and $100\mu m$. After reflection by the parabolic mirror the laser light $\mathrm{E}_{div} + \mathrm{E}_{scat}$ is guided though the $\frac{\lambda}{4}$-wave-plate again before it gets reflected by the PBS. The read-out is done via a balanced photodiode.

2.5.2 Total experimental effective potential

We obtain the spring function, as shown on figure 2.12 for the particles motion by numerically differentiating the experimentally obtained time trace of the particles motion with respect to time. The frequency of the particles' motion is on the order of 50 kHz, while the sampling frequency of the oscilloscope is 2.5 MHz, giving us about 50 data points per oscillation period and therefore a good phase space resolution of the particles' motion.

$$F(x) = -\frac{\partial U}{\partial x} \tag{2.10}$$

We can then obtain the potential structure experienced kinematically by the particle by numerically integrating the spring function with respect to space, in a manner consistent with [58]. This relationship is given by:

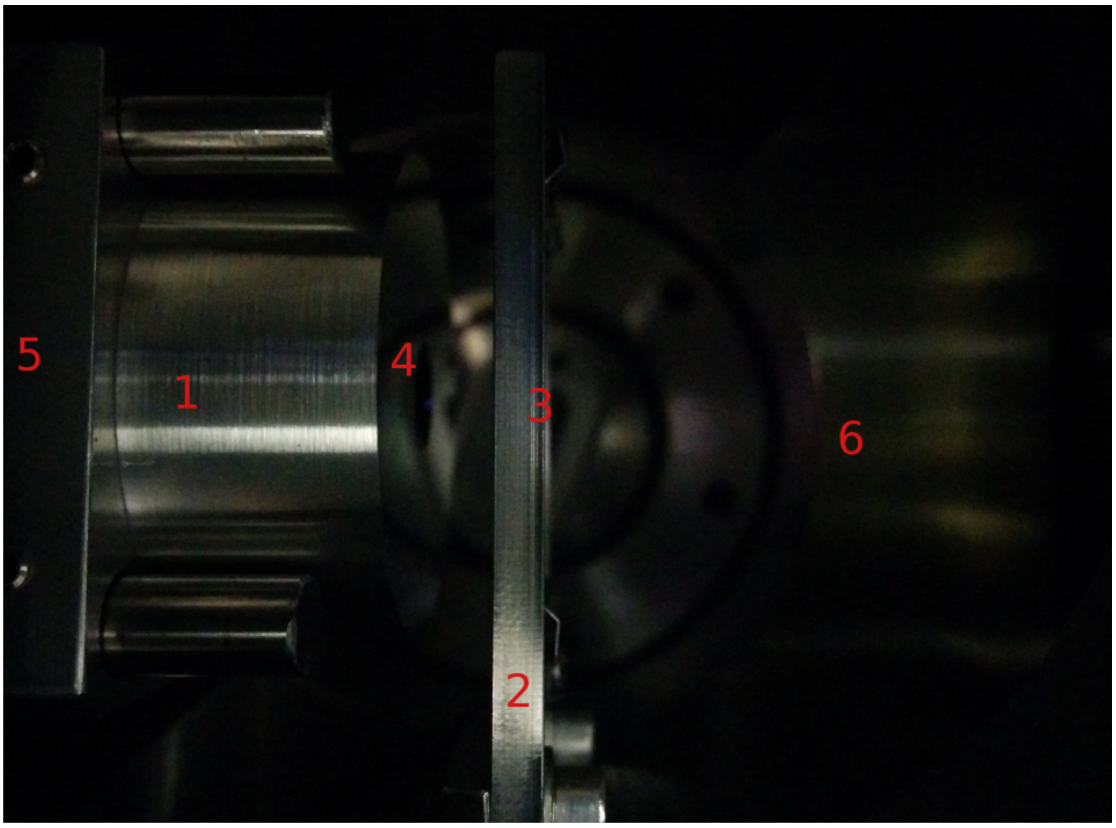

FIGURE 2.6: Photograph of the experiment inside the vacuum chamber. Parabolic trapping mirror (1) and cartesian 3 axes stage (2), holding the Si/SiO_2 wafer (3) - the surface forces of which modulate the motion of the nanoparticle trapped at the mirror focus (4). Mirror mount (5), vacuum chamber (6).

$$U = \int m \cdot a \cdot dx + C \tag{2.11}$$

where m is the particles mass, a its acceleration and C is a constant of integration. Spring functions for the unperturbed and surface perturbed data sets are given in figure 2.12, with the resultant potentials given in figure L.2.

Far from the surface, in the unperturbed case, our levitated nanosphere is trapped in a harmonic potential defined by its high field seeking behaviour with a Gaussian focus in the Mie-Lorentz limit, with an approximate potential given by:

$$U(x) = \frac{1}{2}kx^2 \tag{2.12}$$

As the surface-to-particle distance d becomes smaller the potential experienced by the particle is increasingly perturbed by both optical backscatter and the increasing surface forces from the particle. The changes in the optical power however are generally symmetrical and can be calibrated against the relative frequency drop of the motion in the

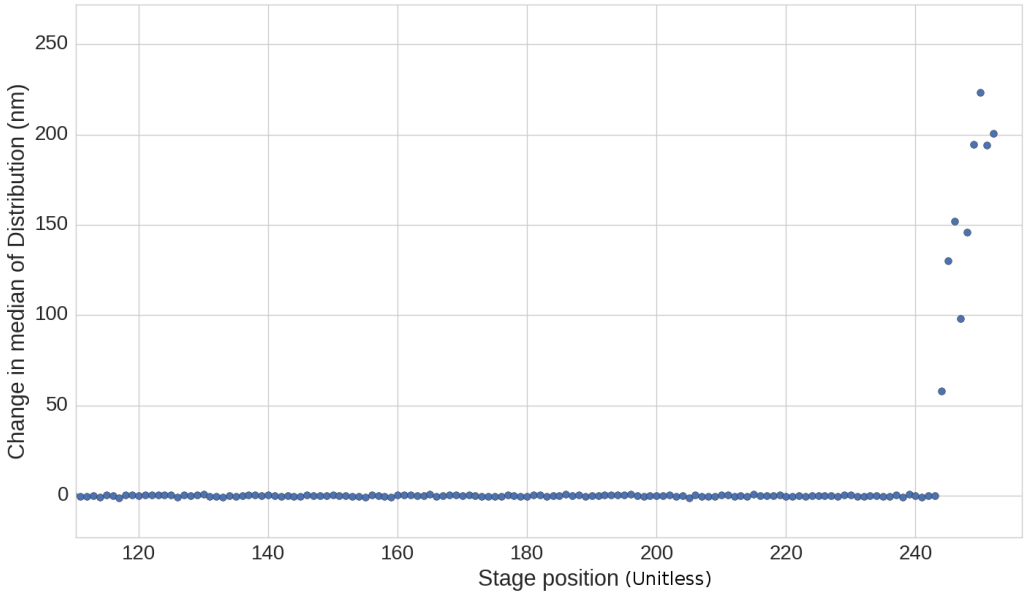

FIGURE 2.7: **Experimental data:** Shift in centre of particle distribution vs stage position. The strong interaction between the surface and the nanoparticle only tends to occur within 10's of microns of the surface (the higher values of stage position correspond to smaller values of particle - surface distance). Each of the datapoints in this graph represents a single stationary position of the stage with respect to the nanoparticle, and the time trace associated with each position can be expanded into a spring function and therefor potential, through the method given in section 2.5.2.

x and y axis. We assume that the optical potential is always symmetrical, composed of even x^2 terms, with the series's higher even ordered terms (x^4 etc) accounting for the Duffing type (this concept is expanded upon in chapter 4) optical nonlinearities experienced in the case of non linear optical potentials.

This assumption can be confirmed by studying the changing structure of the optical potential as a function of laser power, demonstrated in figure 2.8. The parametric driving experiments given in chapter 4 also demonstrate the optical potential remains symmetric even in the case of the nonlinear terms experienced far from the centre of the trapping site.

To extract the non-symmetric surface potential from the total potential we make the ansatz of the Coulomb $(1/x)$-function as a perturbation to the harmonic potential. Then,

$$U_{\text{tot}} = \frac{1}{2}k_{new}x^2 + U_{\text{ic}}(d), \tag{2.13}$$

where U_{tot} is the total potential as experienced by the particle and consists of the harmonic optical trap and the surface interaction shown in Eq. (2.3). Here k_{new} is the spring constant of the optical trap (after symmetric optical perturbations), d is the

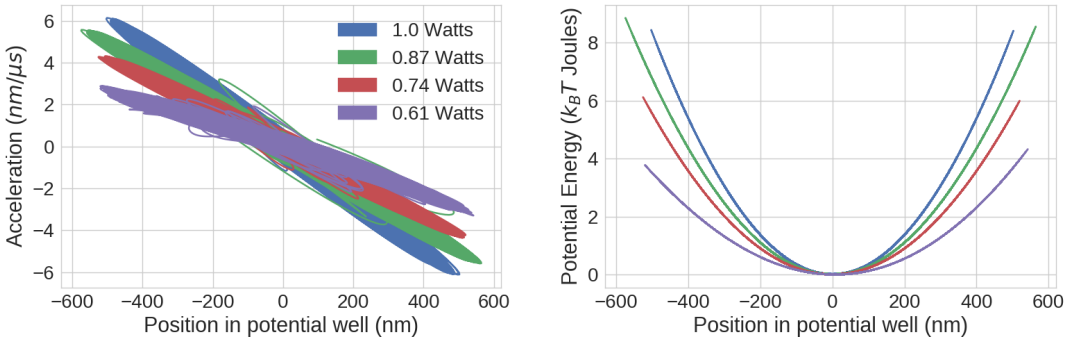

FIGURE 2.8: **Experimental data:** Spring functions and corresponding potentials for various laser powers, and thus ratios of gradient and scattering force. Despite the change in power, the optical potential remains composed of x^2 and higher order symmetrical terms.

distance between the centre of the optical trap and the silicon surface and Q is the charge on the particle. We fit the parameters Q and d such that the output of the function becomes a symmetrical potential, which is usually a kx^2 function similar to the original, unperturbed, optical function far away from the surface, but with a weaker spring function k. Our claim here is that while proximity to the surface does weaken the optical trap it weakens it in a predictably symmetrical way, calibratable by the x and y motional peaks and is not sufficient to explain the anharmonicity experienced by the particle near the surface, whereas a Coulomb image charge model fits well to explain that anharmonicity. It follows naturally that while close to the surface the particle will experience a resultant potential defined by the superposition of the surface dispersion potential and the optical potential. Whilst the full surface potential in the case of a charged particle next to the sandwiched Si/SiO_2 interface we have experimentally is given by the equations in section 2.4.4, it turns out to be possible to simplify this to case of an plane of one material with a distance dependent numerical factor NF, this substitution is made for the ease of fitting to experimental data in a reasonable timeframe, and the (high) validity of the approximation is given in appendixE.

$$U(D)_{effective} = NF \times \frac{-Q^2}{4\pi\epsilon_0\epsilon_3 4D}\frac{\epsilon_2-\epsilon_3}{\epsilon_2+\epsilon_3} + \frac{1}{2}k(x-D)^2 \tag{2.14}$$

where $U_{effective}$ is the potential in the case that it has been perturbed by the surface (harmonic optical trap + $1/x$ type surface Coulomb interaction), k is the spring constant of the optical trap (for a linear trap), D is the distance between the centre of the optical trap and the silicon surface, ϵ_1 is the polarisability of the particle, Q is the charge on the particle. ϵ_2 and ϵ_3 correspond to the nanoparticle and the silicon surface respectively.

Q and D are used as computational brute force fitting parameters such that the output of the right hand side of the function becomes a symmetrical potential, which is usually an $k_{new} \cdot x^2$ function similar to the the original, unperturbed, optical function far away from the surface, but with a weaker spring constant k_{new}.

2.5.3 Dealing with the optical term close to the surface

Naturally, the fact that the silicon/silicon dioxide substrate is not completely transparent means that a standing wave will exist due to the interference of reflected and transmitted light from the surface, and has been reported in[86]. Such a standing wave is also visible in some of our datasets, however the resolution of the mechanical stages the early experiments were conducted with makes reconstruction of an interference pattern difficult. This is most likely due to a combination of different surface alignments suppressing the interference pattern, and of the first experimental runs being performed with stages of much lower position resolution.

Furthermore, the kinematic model applied to the data in this chapter is largely independent of frequency based effects in the system, and the answers it gives fits well with the first principle analysis of comparative force strengths in section. Also, we can use data from the x and y peaks to construct the optical potential function unperturbed by any forces that would just affect the z motion, and thus the physics occurring just in the Z axis. In the case of [86] we notice that the x,y and z data follow the same frequency scaling laws further from the surface, while close to the surface the z frequency increases dramatically, attributed in the paper to the increased optical scattering acting on the particle from the surface, repulsively away from the surface.

In the case of our data we make much the same conjecture, in our case with the net change in frequency in the z axis, as opposed to the x/y plane (accounting for the standing wave), growing increasing negative as the particle approaches the surface. We attribute this to a net negative force acting in the direction of the surface (as opposed to the net positive force in the case of [86]).

2.5.4 Experimental methods - mass extraction

The mass of the nanoparticle is extracted by comparing the potential for the steady state Langevin equation result for our system with the potential obtained by integrating the particle's position-acceleration relation (see figure 2.2d)). The radius is extracted from this based on the assumption that the particle is of spherical shape. Then the radius of the nanoparticle in the experiments was extracted from experimental data to be r =60

nm (±5 nm). More details about the procedure for particle size estimation is described in the general methods section in the first chapter.

2.6 Experimental results

Firstly the centre of the positional distribution shifts towards the surface, demonstrated in figure 2.9.

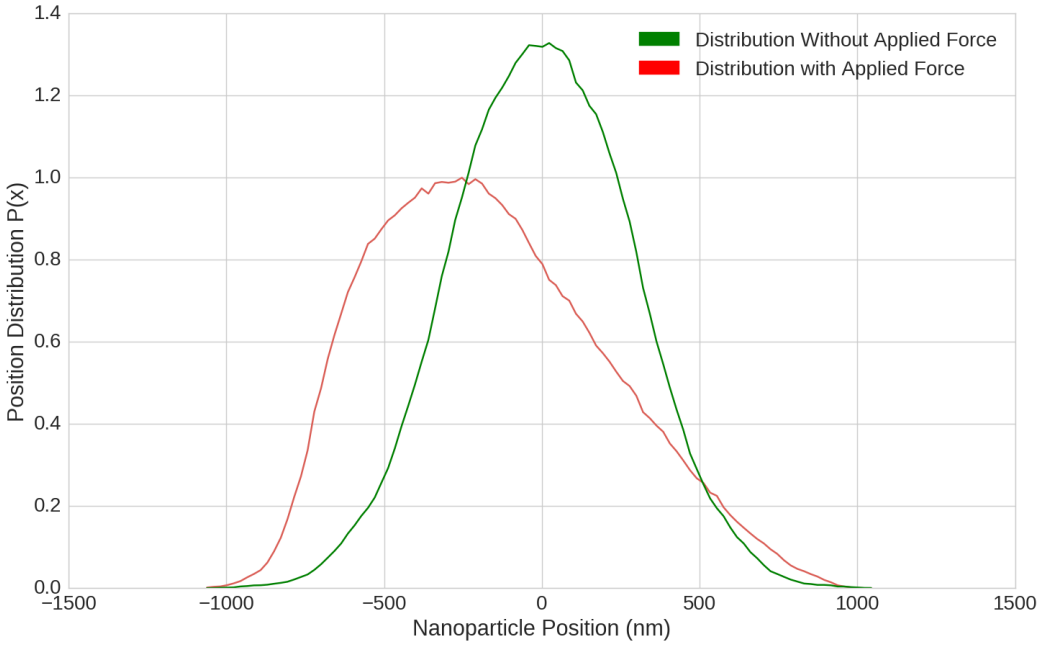

FIGURE 2.9: **Experimental data:** Structural change in particle distribution, far from silicon surface (green), and close to silicon surface (red)

Figure 2.11 shows the phase space of the nanosphere's centre of mass motion far away from the surface (green), and at the closest available position, 4μm (blue), before the surface forces overpower the optical forces and the particle gets lost from the trap. The position distribution of the particle is drawn towards the surface and the motion becomes significantly anharmonic. The unpeturbed stochastic linear motion of the nanoparticle given as the red phase space in figure 2.11 represents the standard thermalised equilibrium state we would expect of a nanoparticle in a harmonic optical potential. Whereas the evolution of the gradient of the outer contour very clearly matches an almost linear potential on the left hand side and an x^2 potential on the right hand side, consistent with the shape revealed by the potential reconstruction in figure L.2.

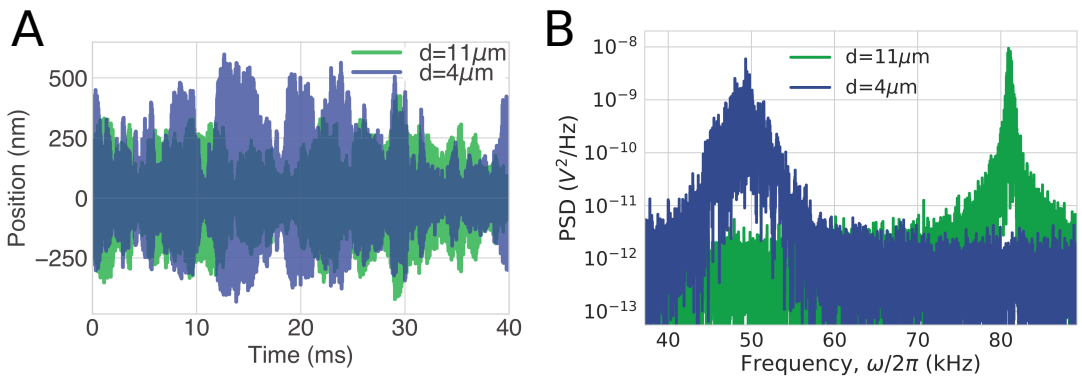

FIGURE 2.10: **Experimental data:** A) Time-trace of the particle position trapped close and far away from the surface. The amplitude of the oscillation grows when the particle is closer to the surface. B)) Power spectral density (PSD) of z-motion of the trapped particle at two different distances. The frequency is lower in the case of the closer PSD since the reflected light from the surface decreases the overall effective quality of the beams' focus.

The shape of the potential changes to an anharmonic one , figure 2.11, with the structural changes in the particles' motional phase space being intuitively related to the shape of the new potential.

We reconstruct the potential $U(r)$ at position r from time-domain position measurements with the methods described in section 2.5.2.

At smaller particle-surface distances d, the trapping potential experiences an increasingly strong perturbation from the surface interaction. Comparing the reconstructed potential with different interaction models shows the best agreement for the case of image charge interaction of charge Q =-11e ($\pm$1e) from fitting the equation 2.3 to the experimental data, as shown in figure 2.6c). The observed particle net-charge is in agreement with typical values in recent experiments with trapped nanoparticles [47, 87]. The observed deviation from the model at small distances could be attributable to electrostatic patch effects, see figure 2.6c). Charge and electric dipole patch effects have been shown to contribute significantly in high-sensitivity surface force measurements [88–90].

To estimate the limit of the experimental sensitivity in this setup, we perturb a suspended nanoparticle with an electric field [47]. This allows us to resolve changes to the potential structure of $2 \cdot 10^{-4} k_B T$. Encouragingly, applying such a resolution to the distance ranges scanned in this experiment predicts we should be able to resolve Casimir Polder forces if the same surface-nanoparticle experiment was to be repeated with a larger particle. We evaluate the experiment to be sensitive to surface forces of 10^{-19} N/$\sqrt{\text{Hz}}$, in contrast to 10^{-10} N/$\sqrt{\text{Hz}}$ in the original atomic force microscope (AFM) paper [91]. This level of force sensitivity allows for detection of genuine Casimir-Polder interactions for a particle of radius 1 μm, while with the best sensitivity demonstrated

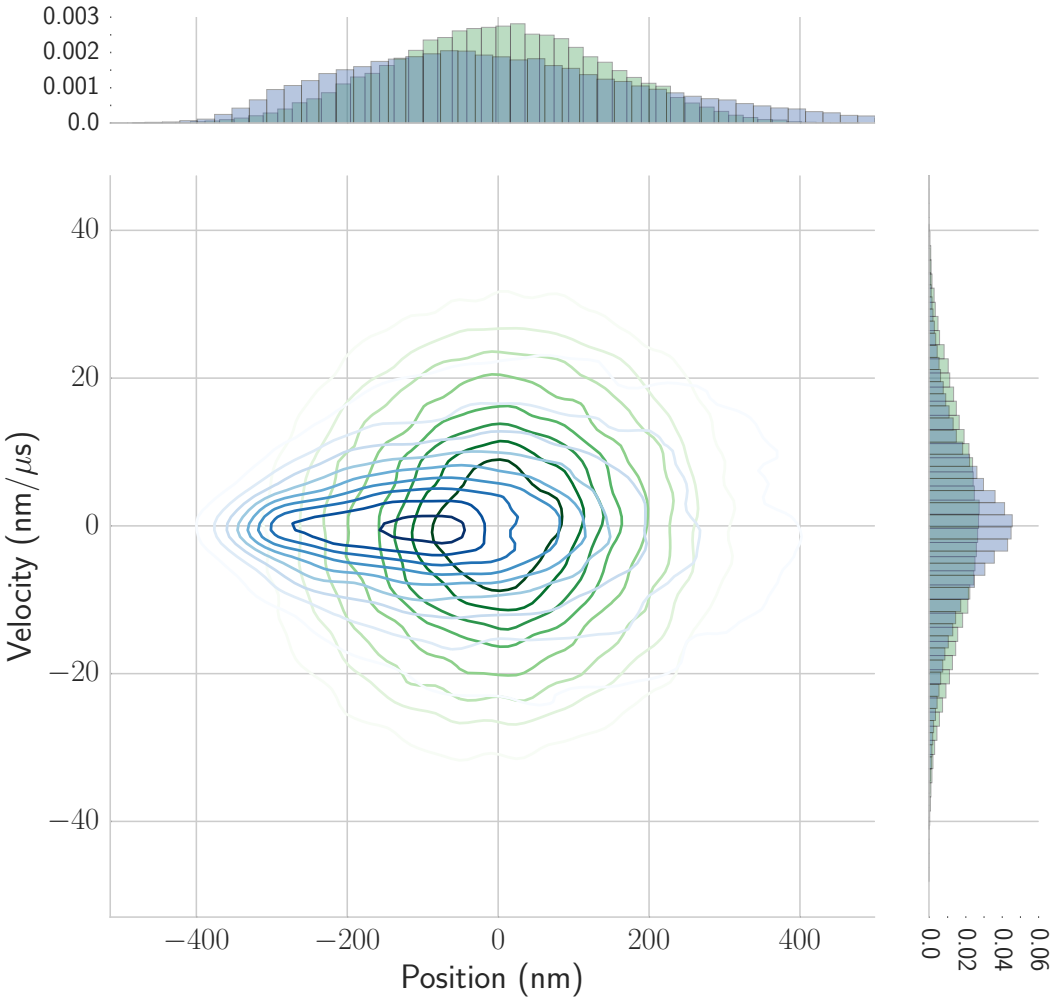

FIGURE 2.11: **Experimental data:** Experimentally obtained phase space contour plot of particles motion, with the motion far away from the surface (11μm+) given in green, and the motion close to the surface (4μm), given in blue. The marginal axis's display normalised histograms of the two distributions.

in this system to date (200 fm/$\sqrt{\text{Hz}}$) [47], the study of genuine Casimir-Polder forces with a 300 nm radius particle appears to be within reach.

The perturbing non-optical surface potential component extracted for each position of the stage is displayed in figure 2.13. Fitting the expected mirror charge self interaction potential, equation 2.3 to these extracted potentials, outputs a particle charge of -11e, concurrent in magnitude with charge numbers on levitated nanoparticle's obtained in recent literature on the subject in similar experimental systems [87].

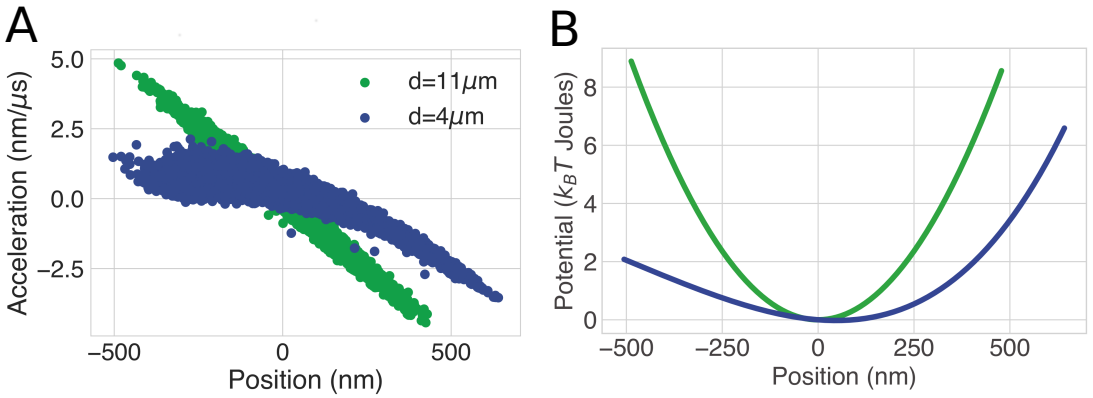

FIGURE 2.12: **Experimental data:** A) The experimentally reconstructed potential as experienced by the particle at the different distances. The potential becomes anharmonic if the particle is closer to the surface. B) Resultant potentials for the nonlinear (blue) and linear (green) motional states of the particle. Obtained by integrating the spring functions in A with respect to space.

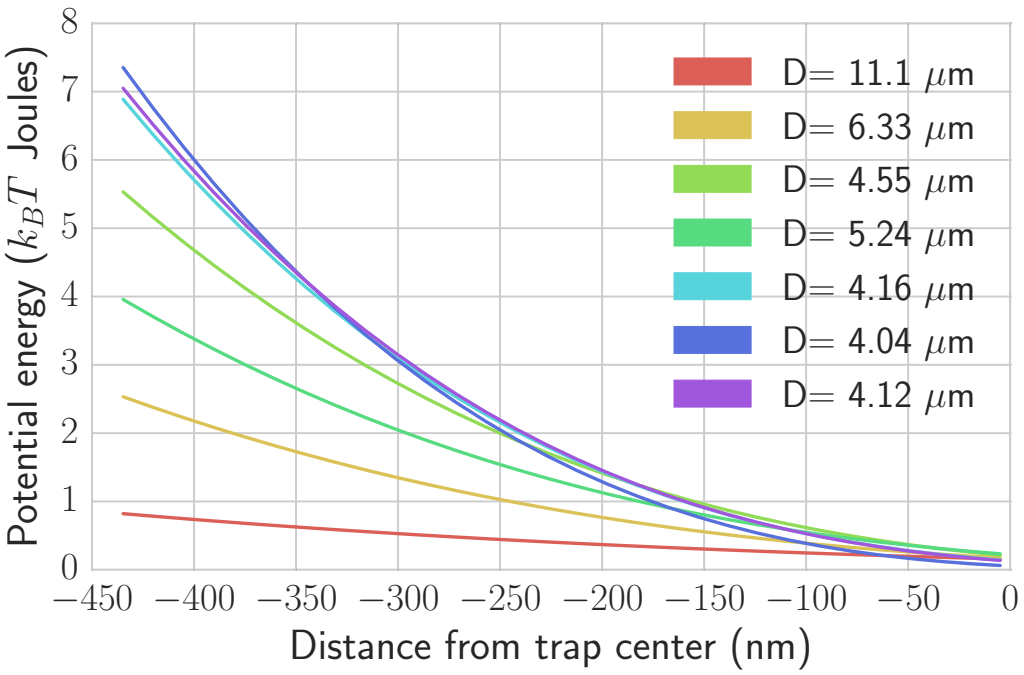

FIGURE 2.13: **Experimental data:** Surface dispersion force potentials experienced by the particle for each position of the 3 axis stage. The crossing of the potential curves at the smallest distance values is most likely due to patch charge effects giving the surface a different value of effective dielectric constant at close distances.

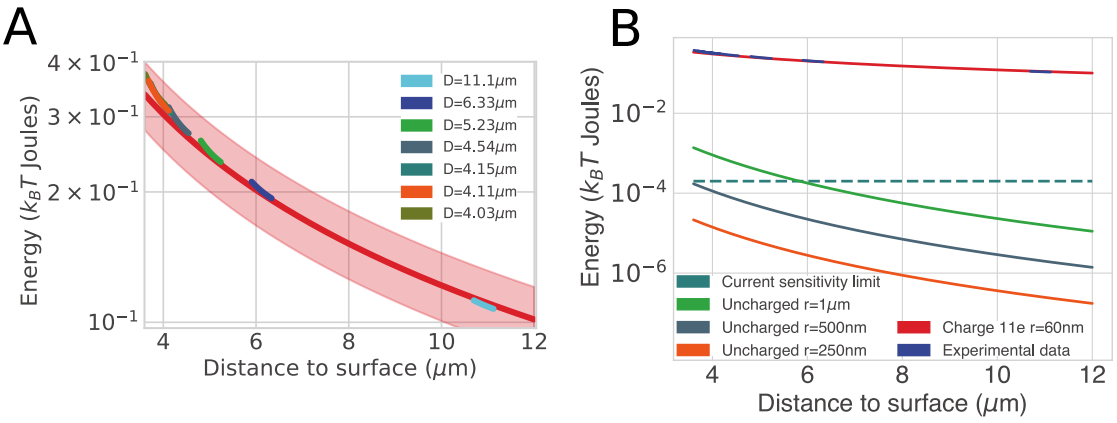

FIGURE 2.14: **Experimental data:** A) Compares the experimental data taken at seven different distances and the theory according to equation(2.3), red line. The pink region indicated the same mirror charge interaction by with ±1 elementary charge e. A slight deviation from the model occurs at distances very close to the surface (¡4μm), in principle this could be explained by patch charge effects. Closer to the surface the best fit with -11e deviates from the experimental data B) Comparative energies of various particle sizes, charged and uncharged, in comparison to the experimentally obtained sensitivity limit of the system.

2.7 Outlook

2.7.1 Requirements for Casimir-Polder force detection

The potential governed by a charged particle interacting with its mirror charge in the silicon surface is several orders of magnitude stronger than the Casimir-Polder forces between a surface and an uncharged particle of the same size.

However, detecting even the dispersion forces for a charged particle demonstrates that the principle of the experiment is sound, puts bounds on the experimental sensitivity to such forces and suggests the next direction required.

The scaling of the Casimir-Polder force in this regime with size and the sensitivity required to see the potential curve from a charged 60nm particle suggests that bringing an uncharged particle of 1μm to a silicon surface will be sufficient to detect Casimir-Polder forces in the present experiment. The theory curves from the start of the Chapter are plotted against experimental data in figure 2.15.

Optically trapping a 1μm particle with a gradient force effect trap however will likely require a specialized beam profile due to the R^6 scaling of the optical scattering force rapidly overcoming the contribution of the gradient force, under which conditions a stable trap is not formed. Even without the Lorentz-Mie contributions, such a trap would be outside of the regular trapping window from the balance of the F_{grad} and $F_{scattering}$ forces.

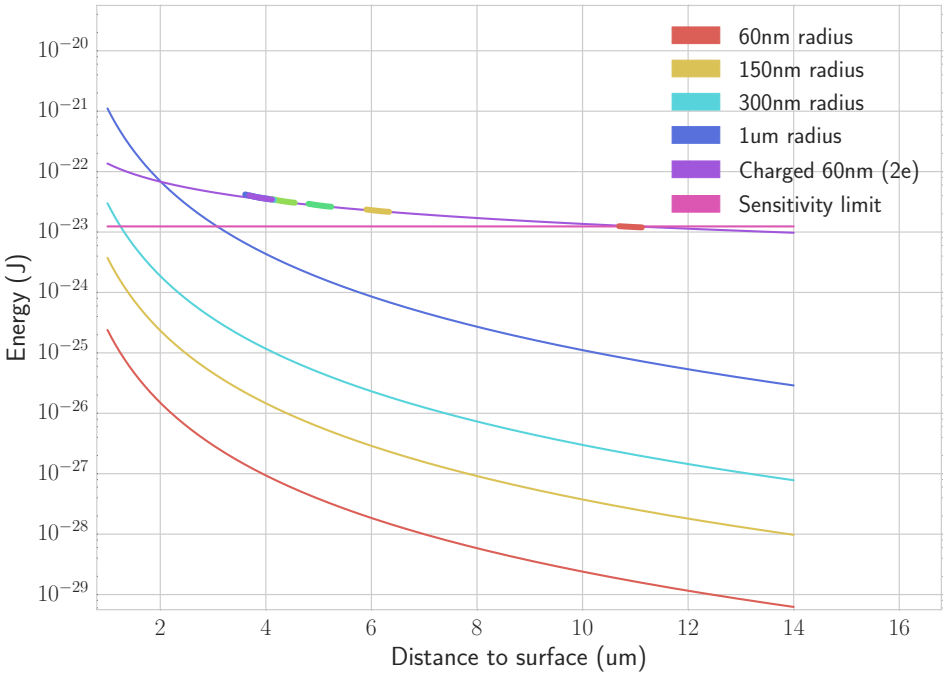

FIGURE 2.15: Extracted potentials from each position of the stage close to the nanoparticle plotting against the expected surface potential from nanoparticle interacting with its self induced mirror charge in the silicon surface.

A spatial light modulator (SLM) defined beam profile could be used to remove central sections of the trapping beam such that the scattering force in the z axis is greatly reduced (z is the weakest axis due to having no opposing scattering force to that focused onto the particle by the mirror over 2π steradians). The scattering forces in the X and Y planes sum to zero over long time scales due to the symmetry of the parabolic mirrors geometry.

2.7.2 2D surface probes

One of the desirable goals of our nanoparticle-surface experiments is to enable the levitated nanoparticle to act as a 2d surface probe, in an analogue of an AFM type system. Since the Coloumb interaction is the strongest surface response in the system presently, we restrict the following discussion to using a charged nanoparticle to map surface structures.

Since the particle naturally explores a region of around 800nm (assuming the beam is well focused, it tends to explore more in the case of poor focusing) in each axes,

an obvious imaging mode might be to use the particles motion in the X,Y degrees of freedom as a natural imaging plane. Dividing up the particle's motion in this plane as a set of virtual pixels and using either the particle population within each pixel (over a set time period), or the average z position of the particle in each binned region of the x-y that each pixel represents. A preliminary attempt at extracting a 2D image from the x-y plane of the nanoparticles motion as it approaches the surface is given in Appendix L.0.1. However, as discussed below, without calibration against an existing and known surface structure, no scientific statement can be made.

Even as a theoretical problem, reconstructing the impact of an arbitrary distributed spatially non uniform potential on the XY plane of the surface on the motion of the particle turns out to be non trivial. As discussed in section 1.5.1, at experimental pressures, the particle hovers between the limits of behaving like a particle undergoing a drift diffusion random walk in a potential and a harmonic oscillator. In each case (drift diffusion and harmonic oscillator), extracting the effect of a perturbing potential in a 1 dimensional system is a solved problem, although this is much easier in the case of the drift diffusion random walk. Furthermore the arguments in section 4 with regards to the positionally reconstructing a potential (as opposed to the force response) only being valid when the particle is in thermal equilibrium may be worth considering in this case.

As the function that transforms the positional density of the particle in time in the XY plane to the surface potential on the XY plane is unclear, it seems immediately logical to gain calibration data in which the particle interacts with an structure of known dimensions.

The calibration structure produced is given in figure 2.16, and is composed of a large (5x5mm) area of metallic crosses thinner than the skin depth for 1550nm light. Thus the light should still be able to penetrate the surface and form a stable trap nearby, however the surface interaction for a thin metal should be much weaker than that for a dielectric. The cross structures are small enough that several should appear in the 800nm normally explored by the particle.

An alternate imaging mode idea might be to use parametric feedback to the reduce the particles position variance to as low as possible before scanning the surface in XY, however this would limit the precision of the final image to the stage accuracy, which is invariably lower that the optical positional resolution on the particle

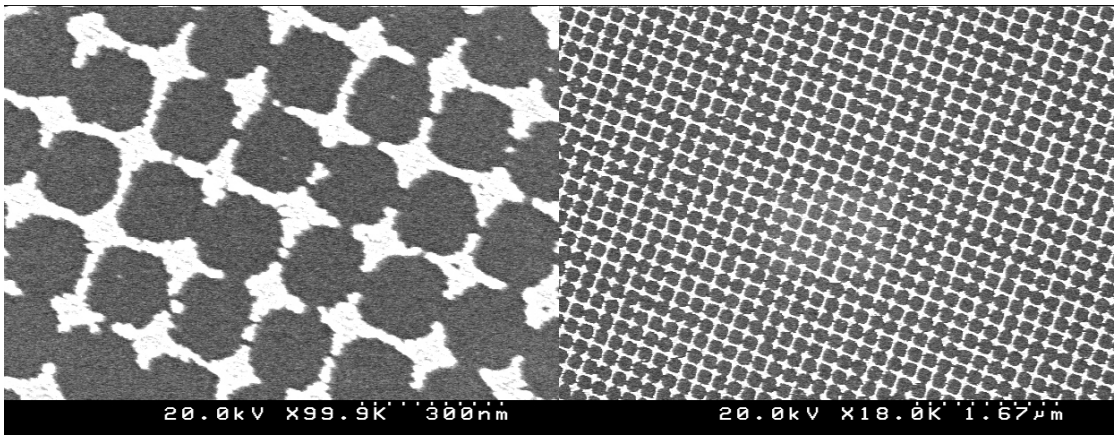

FIGURE 2.16: SEM image of Nanoparticle AFM calibration sample produced at JAIST. Silicon wafer overlaid with sputtered gold below the optical skin depth for 1550nm.

2.7.3 Experimental results - Morse potential behaviour

As well as analyzing the system in terms of phase space and spring functions. It is possible to look at the particle's motional states in both the harmonic and anharmonic potentials in terms of energy.

Kinematically, the relationship describing the energy of the particle is simple:

$$Total\ energy = Kinetic\ energy + Potential\ energy \tag{2.15}$$

The kinetic energy is obtained simply from the particle's velocity data (itself obtained by taking the finite difference with respect to time of the particles' position data) while the potential energy of the particle at each instantaneous moment is computed from its position and the potential energy function obtained by integrating its spring function as detailed above.

Looking at the system in terms of energy allows us to tackle an otherwise unintuitive result in the experimental data. The acceleration-position relationship for the anharmonic potential experienced close to the surface shows, as well as the expected curved structure, significant broadening for the data points corresponding to the particles motion close to the surface, figures L.2 and more obvious in the density plot of the spring functions, given in appendix L.3. Kinematically this acceleration broadening of the particles' motional states close to the surface lacks an obvious driver, with optical speckle or surface outgassing as possible suspects for physical mechanisms.

Structurally, the overall potential of the system appears similar to a Morse potential (A general model describing the potential and energy state of a harmonic oscillator when under the influence of an attractive body), taking the histogram of the particle's

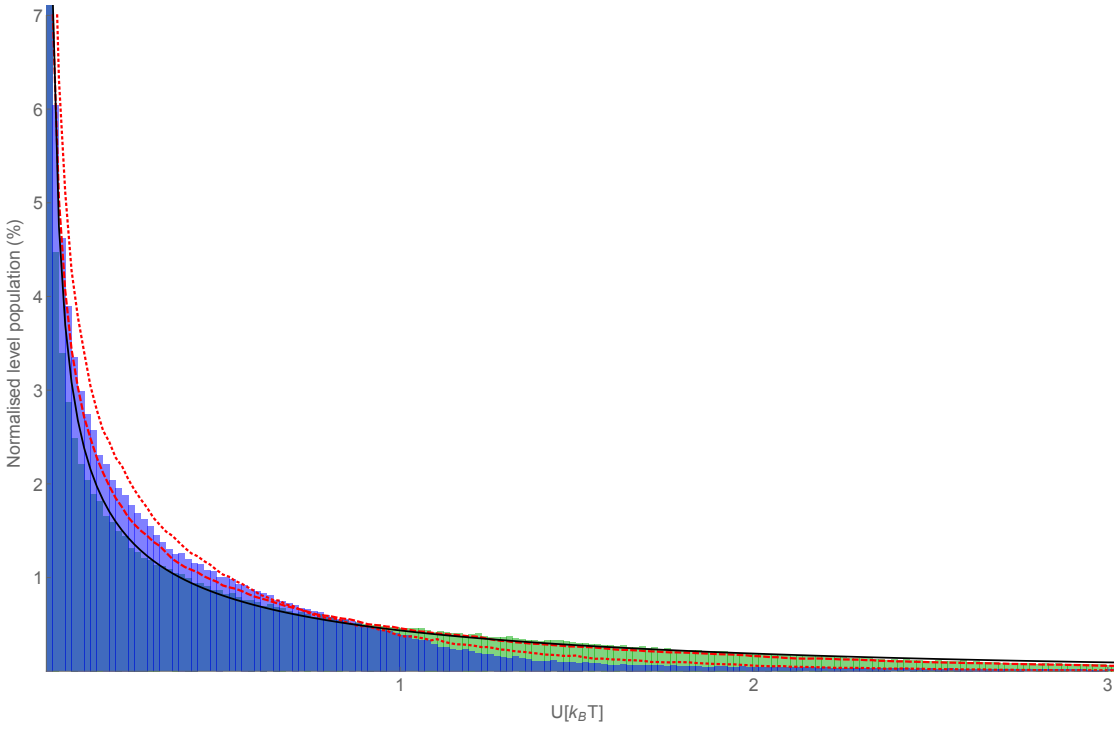

FIGURE 2.17: Normalised histogram of the particle's potential energy for the cases of an harmonic potential (particle far away from surface, green) and an anharmonic Morse-like potential (particle close to the surface, blue). Shown in red are the results of numerical simulation of the particle's motion for harmonic (dashed) and anharmonic (dotted) potentials with 10 000 different realisations with randomised amplitudes. The solid black line is the normalised result of equation (2.19). The Morse-like potential shows a similar behaviour in energy level scaling (and in the population of those energy levels) as compared to the harmonic case until diverging strongly at a high value of n, which is the expected Morse-like behaviour.

total energy, the population also follows the expected scaling relation, figure 2.17. The histogrammed energies for the harmonic potential follow the expected structure for a Maxwell-Boltzmann potential for a harmonic energy level structure.

The shape of the histogram in figure 2.17. can be understood in the following way. For the case of the linear potential, the particle undergoes harmonic motion:

$$x(t) = x_0 \cos \omega t \tag{2.16}$$

which can then be used in the potential energy $U = \frac{1}{2}kx(t)^2$. Making a histogram of the potential found in this way at evenly-spaced times results in a two-peak shape, in contrast to that shown in figure 2.17. This can be described by solving $U = \frac{1}{2}kx(t)^2$ with $x(t)$ given by equation (2.16), giving;

$$t = \frac{1}{\omega} \arccos \left[\frac{1}{x_0} \sqrt{\frac{2U}{k}} \right] \tag{2.17}$$

The time spent within any time interval dt will then be given by

$$dt = \frac{dt}{dU}dU = -\frac{\mathrm{sgn}(x_0)}{\omega\sqrt{2U}\sqrt{kx_0^2 - 2U}}dU \tag{2.18}$$

which, subject to proper normalisation, corresponds to the likelihood of the particle being observed within a potential energy between U and $U + dU$. It is clear that dt has maxima at $U = 0$ and $U = \frac{1}{2}kx_0^2$, resulting in the two-peak structure discussed above (and shown for each individual energy in section 1.4.2). However, this is not seen in the histogram of energies extracted from the experimental data (fig. 2.17), rather a single peak at $U = 0$ is found in both the harmonic and anharmonic cases.

This difference comes from the fact that the motion of the particle in the trap is only well-described by equation (2.16) when the particle is under low damping and low rates of random collisions. The experiment takes places at vacuum of 10^{-2}mbar, meaning the particle's motion is still significantly affected by interactions with the background gas. The interactions with the background gas thermalize the particles energy across many different motional modes. This is incorporated into the description of the system by assuming that the motion may be taken to be averaged over many trajectories, each with a different amplitude x_0, Gaussian-distributed about some mean value $\overline{x}_0$ with a standard deviation σ. In the case of the harmonic potential, we compute:

$$\overline{dt} = -\frac{1}{\sqrt{2\pi\sigma^2}}\int_{\sqrt{2U/k}}^{\infty} dx_0 e^{(x_0-\overline{x}_0)^2/(2\sigma^2)}\frac{\mathrm{sgn}(x_0)}{\omega\sqrt{2U}\sqrt{kx_0^2 - 2U}}dU \tag{2.19}$$

With x_0 (motional amplitude) being the integration variable, and σ being the only fitting parameter. The result for $\sigma = 100$ nm is shown in figure 2.17, alongside the experimental data (for particle surface distances d=4μm and d=11μm respectively) and a numerical simulation in the case of the anharmonic potentials. For the latter case the equations of motion cannot be solved analytically, so there is no equivalent of equation (2.19) for the anharmonic potential and the trajectories are simulated numerically.

It is seen (in figure 2.17) that the modelling of the background gas collisions smearing out the amplitude of the oscillations is consistent with experimental results, especially for relatively high energy. Both results display the required behaviour of having a single peak at $U = 0$, which can be intuitively understood from our averaging procedure as the trajectories pass many times through $U = 0$ but have different maximum values, the peak of equation (2.18) at $U = \frac{1}{2}kx_0^2$ is therefore suppressed in the histogram. This averaging out is consistent with the central limit theorem.

The energy distribution can also be understood by looking at the functions governing energy levels in the potential wells. To stress, we are far from the quantum regime and

the state of the particle is thermal in nature. However, it is still reasonable to use a quantum harmonic oscillator description of the particle here with a very high occupation number n[92]. The spacing of energy levels in the quantum harmonic oscillator is a constant $\hbar n$ between levels. In the case of the morse potential however, the energy spacing is given as:

$$E(n+1) - E(n) = \hbar n - \frac{(n+1)(\hbar n)^2}{2D_e} \tag{2.20}$$

where n is the energy level of the oscillator, $E(n)$ its energy in its corresponding eigenstate and D_e is the dissociation energy of the two mutually attractive bodies described by the Morse potential model, in this case the levitated nanoparticle and the surface. The dissociation energy of a Morse potential corresponds to the amount of energy required to separate the two attractors.

The implications of these two separate scalings (harmonic oscillator and Morse) are that the potential will behave similarly in terms of energy level scaling and populations until a cut-off point where the behaviours will begin to strongly diverge. The Morse potential should also have a different ground state energy facilitated by the perturbing fields alteration to its level structure.

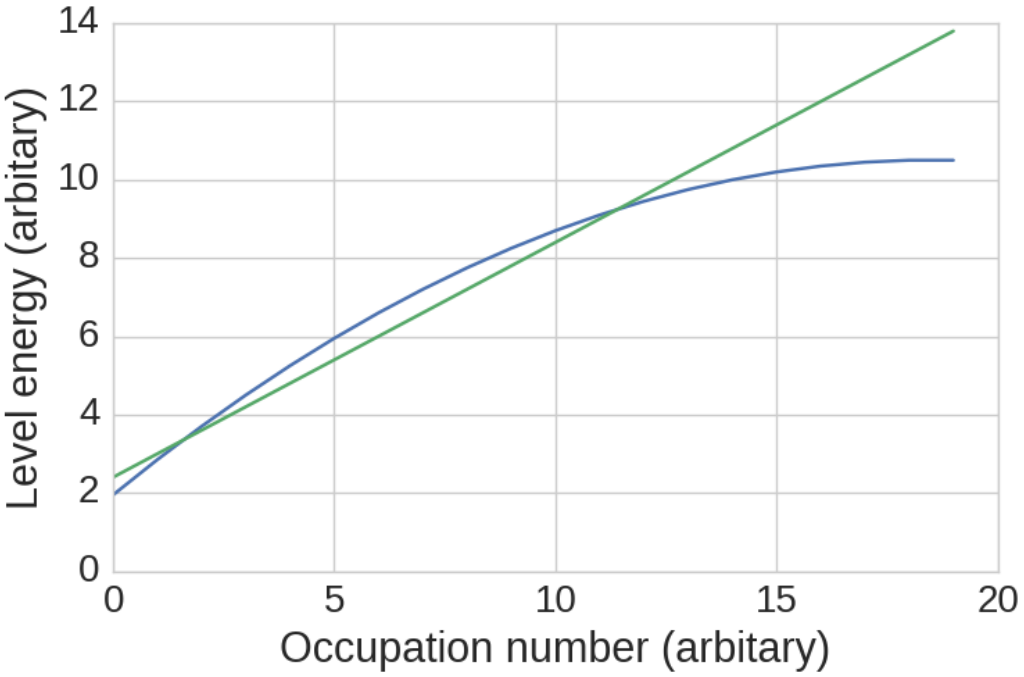

FIGURE 2.18: Energy level scalings for the harmonic and morse potential case. In the case the morse potential has a lower ground state energy the ladders intersect twice. The two functions

The scaling of energy levels in the harmonic and Morse case are given in figure 2.18 in terms of arbitary units, with the Morse case having a lower starting ground state energy. Further analysis of this scaling behaviour could allow us to fit the dissociation energy associated with the surface interaction directly (and act as another distance - surface metric), as well as lifting the energy degeneracy associated with a harmonic potential, potentially allowing for other methods of state preparation if combined with a pulsed operation, as has been proposed for other anharmonic potentials [93].

2.8 Chapter conclusion

In conclusion we have measured the surface dispersion interactions between a charged levitated particle and a section of uncharged silicon. We demonstrate it is possible to extract the particle charge and distance to the surface, obtaining a charge of -11e for our test particle. We compute the current sensitivity of the experiment to surface forces to be 10^{-19} Newtons, although 10^{-21} Newtons should be possible in this geometry as system with the same oscillator but lower pressures and electronic noise floors have demonstrated under parametric feedback [94].

As demonstrated in figure 2.15, trapping a $1\mu m$ particle in the current system at current experimental pressures would likely be sufficient to detect genuine Casimir-Polder forces, however due to the scaling of the opposing trapping forces, this would likely require a hollow beam to accomplish (detailed in section 2.7). Also, given the much stronger scaling relations of the Casimir and Coloumb forces, the charge on the particle will either need to be very low or completely neutralized.

If the force sensitivity could be pushed closer to already achieved values within similar geometries [94] then a 250nm particle would be sufficient for detection of Casimir-Polder forces. This would likely have its own disadvantages however, to achieve the required Q factors for this level of force sensitivity the experiment would have to be conducted at high vacuum, requiring the presence of feedback cooling to sustain the particle and naturally suppressing the nonlinear terms from which the potential extraction is derived. A possible solution for this would be to use a feedback scheme to keep the particle trapped under high vacuum, and use the rough and fine feedback parameters outputted by the Bose function (also called a transfer function) of the lock in amplifier as the nonlinear sensitivity metric.

Finally, we have shown that the nanosphere-surface system forms a macroscopic classical analogue of a molecule-surface system, and follows the expected ladder relations and populates the energy distribution as expected, albeit at extremely high n. It should be

noted that no discreetness is observed in the energy distribution and no such claim is made in this thesis.

We expect this to be an interesting experimental platform for the exploration of a Casimir-Polder physics in the thermal regime, as well as potentially offering the parameters required to investigate rotational symmetry breaking [77] and repulsive Casimir effects.

The careful analysis of the particle position measured in the lateral directions along the surface may allow for topographic images in close analogy to scanning probe techniques.

Future work will likely entail replacing the vibrationally inert silicon surface with a substrate bound resonant membrane oscillator system such as a graphene MEMS device or a silicon nitride membrane. Having two oscillating structure of similar frequencies would in principle allow for strong coupling of the two systems. As membrane structures have already been cooled into their quantum mechanical groundstate[95] by all optical feedback and the distances demonstrated this experiment are within the small number of microns, a sympathetic feedback scheme to cool a levitated nanoparticle via a resonator is not unreasonable. Furthermore the coupling of two, potentially quantum mechanical, systems would allow for similar implementations to nonlinear state generation schemes, such as those proposed by [93].

Chapter 3

Fano resonances

3.1 Chapter overview

A Fano resonance or antiresonance is an interference effect between discrete and continuous states, and is a general wave phenomenon[96] that can manifest in a variety of physical systems, the details of which are explained further in section 3.2. In this chapter we briefly introduce Fano resonance effects, explain how the effects can manifest in a system of coupled classical driven damped oscillators, detail our experimental implementation to generate such a resonance effect and finally discuss our results, in which we experimentally demonstrate a Fano resonance in an optically levitated system for the first time.

Experimentally we parametrically drive system to the non-linear regime of the optical potential: there the translational motions become coupled by the intrinsic cross terms of the Gaussian focus, and the antiresonance appears during the transition to the out of equilibrium steady state. We achieve a similar coupling effect between the degrees of freedom by applying a DC electric field. Furthermore, we show that this coupling opens a new cooling channel, namely, sympathetic cooling, whereby when cooling one translational degree of freedom, the other two degrees of freedom in the system also start to cool. In addition, we give a full theoretical model of the system, discuss the feedback terms, and fit the data using a numerical simulation.

3.2 Motivation

Recent developments in the field of levitated optomechanics include the generation of a variety of non classical or otherwise non linear motional modes, such as mechanical

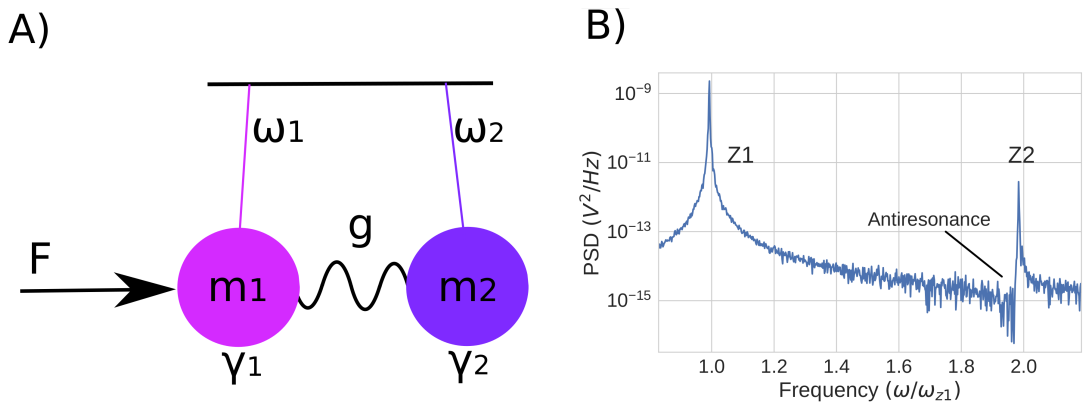

FIGURE 3.1: (A)Basic concept of two coupled oscillators of frequencies ω_1 and ω_2 and dampings γ_1 and γ_2 in motion the first oscillator can be driven at a frequency and phase such that it arrests the motion of the second oscillator in a specific frequency band. (B) Experimentally induced Fano resonance in a levitated nanoparticle through optical driving. In units of the frequency of the first oscillator ω_1. When the oscillator mode ω_1 is coupled to the oscillator mode ω_2 and given the correct driving and coupling conditions, an antiresonance effect is generated.

squeezing [9], high frequency free rotations of nanorods [39] and precession effects [97]. All of these generated states rely on the control, or at least physical understanding of nonlinearities or controlled coupling between degrees of freedom in the system.

Here we demonstrate the implementation of another entry into this manipulation toolbox, controllable Fano-type antiresonance phenomena[98, 99]. These manifest in a variety of characteristic line shapes [100], depending heavily on the coupling parameters used to generate them. Although all of them possess the same basic characteristics of the Fano phenomenon.

The ubiquitousness in nature, across different systems, is not surprising, given that only a few basic requirements have to be satisfied for its appearance. In particular relevance to our case, a Fano antiresonance can be generated in a simple linear system of two driven coupled harmonic oscillators [101]. Other examples can be found in atomic spectroscopy [102], nanomechanical resonators [103] and optoelectronic systems make use of antiresonance phenomena to enable optical switches and frequency discriminators [104–106].

In many systems antiresonance phenomena generate electromagnetically-induced transparency (EIT)[100]. In cold atoms, the existence of this anti resonance mode (referred to sometimes as a dark resonance) has been experimentally demonstrated to enable sub Doppler cooling sufficient to drive an atomic system into its quantum mechanical ground state. EIT has also been demonstrated to enable ground state cooling of a trapped ion [107], as well as to enable sympathetic cooling of an ion chain [108], although not to the ground state. An EIT reliant scheme has also enabled ground state cooling of a

nanomechanical resonator [109]. Furthermore, a Fano resonance reliant cooling scheme has been proposed recently for levitated nanoparticles [110].

3.3 Theoretical model

3.3.1 Fano factor

The general form for a Fano resonance is given by[100]:

$$\sigma(E) = D^2 \frac{(q+\Omega)^2}{1+\Omega^2}, \tag{3.1}$$

where q is the Fano parameter $q = cot(\delta)$, itself a function of the phase shift between the two modes δ. $\Omega = 2(E - E_0)/\gamma$ where E_0 is the resonance energy and γ is the resonance width [100], $D^2 = 4sin^2\delta$.

This can be rewritten in terms more compatible with the experimental output of our system:

$$S_{xx}(\omega) \propto \frac{(q\Gamma + (\omega^2 - \omega_0^2))^2}{\omega^2\Gamma^2 + (\omega^2 - \omega_0^2)^2}, \tag{3.2}$$

where Γ is the sum total of damping processes in the system[111].

3.3.2 Intuitive model of Fano resonances.

As a Fano resonance can in principle occur in any system capable of destructive interference, the antiresonance to resonance lineshaping effect can be observed between two coupled classical harmonic oscillators for the correct values of coupling and driving, shown conceptually in figure 3.1.

In the classical analogy of harmonic oscillators coupled by weak springs, an intuitive view of the antiresonance can be regarded as destructive interference of the forces on one of the two coupled oscillators by the action of the second oscillator. That is to say the driving motion of the second oscillator is chosen such that is cancels the natural frequency oscillation of the first oscillator. Its important to note that the motion of the oscillator is only cancelled at that specific frequency, and that the 'temperature' of the overall frequency mode remains the same.

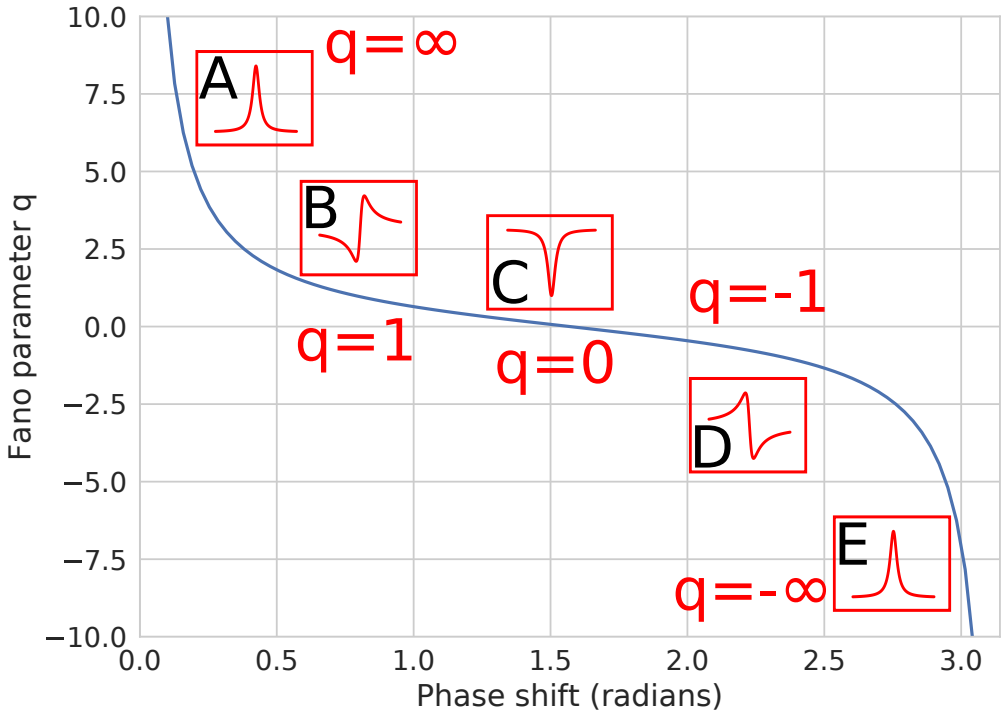

FIGURE 3.2: **Simulation:** Fano parameter q versus phase shift between the modes. A and E represent the regular Lorentzian resonances associated the motion of the unpeturbed particle. B and D represent the Fano resonance windows generated throughout this chapter and C represents an induced transparency mode, similar to EIT, which has yet to be realized in a levitated nanoparticle system.

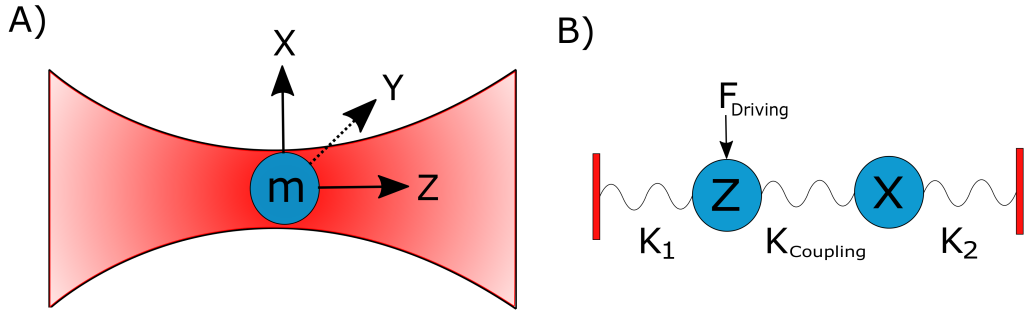

FIGURE 3.3: Two classical oscillators are connected to two different springs k1 and k2, in our case, k1 and k2 represent the coupling of the motion of the oscillator's z and x degrees of freedom to the light field. They are also coupled to each others motion via a third spring $K_{coupling}$, which is, in our case given by the Gaussian cross terms of the non linear components of the trap in the optical case. The lefthand mass is sinusoidally driven by an external force.

3.3.2.1 Intuitive model - derivation

Before understanding the case where both oscillators are driven damped, a more simple formulation can be adopted for which an analytic solution exists. Understanding the system in such approximated terms is important because it provides an intuitive understanding for later results, such as for why the 'handedness' of the antiresonance changes (on which side of the frequency center of the oscillation it occurs), as the system falls changes phase, this turns out to correspond to whether the system being in a cooling or heating mode.

In the first case, we consider two classical oscillators, one with a resonant driving force F, and one left to decay freely. Derivation as follows [96]:

In the simple case of a driven damped oscillator, we find the equation of motion:

$$\ddot{x} + \gamma\dot{x} + \omega_0^2 x = Acos(\omega t) \tag{3.3}$$

where x represents the displacement of the test mass, $\dot{x}$ its velocity, $\ddot{x}$ its acceleration, γ the damping on the oscillator. ω_0 is the natural frequency of the oscillator and $Acos(\omega t)$ is an external sinusoidal driving term we apply by modulating the light field with an acousto-optic modulator (AOM) as seen in figure 3.5.

This has the complementary solution: [101]

$$x_c(t) = e^{-\gamma/2}[q_1 e^{i\Gamma t} + q_2 e^{-i\Gamma t}] \tag{3.4}$$

where:

$$\Gamma = \sqrt{w_0^2 - \gamma^2/4} \tag{3.5}$$

Thus, the solution for the amplitude at a particular frequency can thus we found to be:

$$c(w) = \frac{a}{w_0^2 - w^2 + i\gamma w} \tag{3.6}$$

with modulus:

$$\text{mod } c(w) = \frac{a}{\sqrt{(w_0^2 - w^2)^2 + w^2\gamma^2)}} \tag{3.7}$$

and phase:

$$\phi(w) = arctan(\frac{w\gamma}{w_0^2 - w^2}) \tag{3.8}$$

A key point of interest here is that the oscillator's phase changes by π as the frequency of the oscullator (ω) passes through the resonant frequency (ω_0). This is important to note because it implies that if the resonant drive is in phase with the oscillator when it is on the lower frequency part of the resonance, and out of phase when its frequency is greater than the central resonance frequency. This has later implications for on which side of the peak the anti resonance appears.

In the case of two coupled oscillators we declare the equations of motion to be:

$$\ddot{x_1} + \gamma_1\dot{x_1} + \omega_1^2 x_1 + \nu_{12}x_2 = a_1 e^{i\omega t} \tag{3.9}$$

and:

$$\ddot{x_2} + \gamma_2\dot{x_2} + \omega_2^2 x_2 + \nu_{12}x_1 = 0 \tag{3.10}$$

It is important to note that (in this simple model) only one oscillator (ω_1) in this interaction is driven, as the second oscillator (ω_2) is damping the motion of the first oscillator at a given frequency. In reality both of the oscillators are driven damped, however since the driving force is stochastic in the real world, there will be sections of time in which the above model (of only one oscillator being driven) is true. From [96] we find the amplitudes of the steady state solutions of the two harmonic coupled oscillators are therefore given as:

$$c1 = \frac{(\omega_2^2 - \omega^2 + i\gamma_2\omega)}{(\omega_1^2 - \omega^2 + i\gamma_1\omega)(\omega_2^2 - \omega^2 + i\gamma_2\omega) - \nu_{12}^2} \tag{3.11}$$

$$c2 = \frac{(\nu_{12})}{(\omega_1^2 - \omega^2 + i\gamma_1\omega)(\omega_2^2 - \omega^2 + i\gamma_2\omega) - \nu_{12}^2} \tag{3.12}$$

where ν_{12} is the coupling between the two oscillators.

Comparing the case for the uncoupled driven damped harmonic oscillator to the solution for each of the coupled oscillators in the interaction (The resonance enabled by the coupled interaction has different effects on each of the oscillators.), we can predict the change to the amplitude solution for each of the coupled resonators.

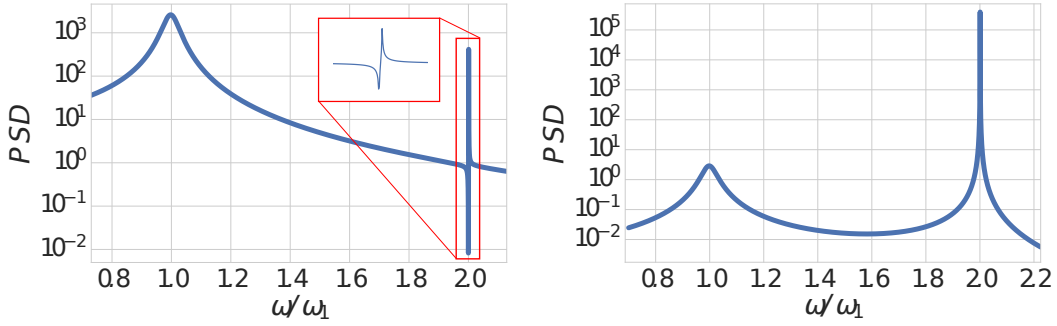

FIGURE 3.4: Theoretically predicted effect of Fano resonance on the first oscillator (left) and second oscillator (right). Once again, both oscillators posses only a single Lorentzian lineshape resonance at their respective natural frequencies before the Fano like interaction takes place.

The first resonator in the interaction splits into two lineshapes, one of which is the antisymmetrical resonance characteristic with fano resonance interactions. The theoretical prediction of this effect can be seen in figure 3.4, the experimental data follows the predicted lineshape. The second resonator also splits into two Lorentzian style lineshapes, one of which is the initial frequency mode, which becomes significantly smaller in amplitude, this can be seen in the same figure.

In this simple analytic model, we assume a linear coupling between two oscillators. However, the actual coupling can be derived for the case of a Gaussian focus, section 3.3.3.1.

3.3.3 Coupling mechanism

3.3.3.1 Coupling from optical cross terms

From previous experiment studies in this regime, it is often claimed that the system may be treated as 3 decoupled classical oscillators below 10 millibar [58].

This approximation however relies on the assumption of a harmonic trap, which for a Gaussian beam is only true at relatively smaller amplitudes. At large oscillation amplitudes the nanoparticle experiences both inherent optical Duffing nonlinearities and cross terms in the optical spring.

The intensity of Gaussian optical beam is given by:

$$I(x,y,x) = I_0(\frac{w_0}{w_z})^2 Exp(\frac{2(x^2+y^2)}{w_z^2}) \tag{3.13}$$

where w_z is the waist of the beam, given by the expression:

$$W(z,R) = w_0 = \sqrt{1 + (\frac{z}{zR})^2} \tag{3.14}$$

This leads to the potential for a particle of polarisability χ given by:

$$U(x,y,z) = \frac{\chi I(x,y,z)}{c} \tag{3.15}$$

Since the spring constant of the oscillation in any direction coordinate q is given by:

$$k_{qq} = \frac{\partial^2 U}{\partial q^2} \tag{3.16}$$

In a 3d system, we can expect this relation to be:

$$k(x,y,z) = \begin{bmatrix} k_{xx} & k_{xy} & k_{xz} \\ k_{yx} & k_{yy} & k_{yz} \\ k_{zx} & k_{zy} & k_{zz} \end{bmatrix} \tag{3.17}$$

with the cross terms xy and yx giving, for example, the coupling between the x and y degrees of freedom. Future work will further quantify this and match the experimentally obtained coupling obtained by fitting the position of the motional peaks to the model given by the classical Fano analogy between two oscillators to the theoretical coupling obtained by the above method.

3.4 Numerical model of experiments

The model previously considered is helpful to gain an intuitive understanding of the system, however it rapidly becomes unsuitable when considering 3 coupled oscillators, the complexities of an experimentally realistic potential, and stochastic effects. Thus, we turn to numerical simulation to fully fit theory to our experimental data. The majority of this section is from presently unpublished work in collaboration with M.Toros and D.Hempston.

Due to the complexity of the Fano resonance effect, the numerical model considered in this section is somewhat more sophisticated that given elsewhere in this thesis. Just as before we consider an optically levitated particle at the focus of a Gaussian focus subject to direct homodyne detection [112]. In this case however, all three degrees of

motion of the particle are simulated, rather than the one-dimensional considerations given in chapters 2 and 4.3.1 so that the displacement dependent couplings between them can be computed. It is extremely important here that the particle be spherical, so that the only couplings between the degrees are ones that we specifically enable, either by driving or coupling with electric fields. Also, each degree of freedom of the particle (before coupling), must have the same phase profile as the simple model considered in 3.3.2.1.

The model is composed by adapting the theoretical description of general anisotropic particles in [38] to the special case of isotropic, spherical particles. The particle has three translational degrees of freedom: we denote the position operator by $\hat{\boldsymbol{r}} = (\hat{x}, \hat{y}, \hat{z})^\top$ and its conjugate momenta by $\hat{\boldsymbol{p}} = (\hat{p}_x, \hat{p}_y, \hat{p}_z)^\top$.

3.4.1 Stochastic master equation

The system is modelled using the following stochastic master equation :

$$\begin{aligned} d\hat{\rho}_c = &-\frac{i}{\hbar}[\hat{H}_{\text{free}} + \hat{H}_{\text{fb}}, \hat{\rho}_c]dt \\ &+ \frac{i\gamma_c}{2\hbar}[\hat{\boldsymbol{r}}\cdot\hat{\boldsymbol{p}} + (\hat{\boldsymbol{r}}\cdot\hat{\boldsymbol{p}})^\dagger, \hat{\rho}_c]dt + \gamma_c \sum_{j=1}^{3} \mathcal{D}[\hat{\boldsymbol{L}}_j]\hat{\rho}_c dt \\ &+ \gamma_s \sum_{\nu=1}^{2} \int d\boldsymbol{n}\mathcal{D}[\hat{A}_{\boldsymbol{n},\nu}]\hat{\rho}_c + \sqrt{\eta\gamma_s}\mathcal{H}[\hat{B}e^{i\Delta\phi}]\hat{\rho}_c dW, \end{aligned} \tag{3.18}$$

where $\hat{\rho}_c$ is the conditional state at time t. We now discuss separately each of the terms on the right hand-side.

On the first line of Eq. (3.18) we have the Hamiltonian ($\hat{H}_{\text{free}}$) and feedback ($\hat{H}_{\text{fb}}$) terms:

$$\hat{H}_{\text{free}} = \frac{\hat{\boldsymbol{p}}^2}{2m} + U(\hat{\boldsymbol{r}}), \tag{3.19}$$

$$\hat{H}_{\text{fb}} = \beta \left(\frac{\frac{\langle \hat{p}_z \rangle}{\sqrt{2m}}\cos(\Theta) + \frac{\sqrt{m}\omega_z \langle \hat{z} \rangle}{\sqrt{2}}\sin(\Theta)}{\langle \frac{\hat{p}_z^2}{2m} + \frac{m\omega_z^2}{2}\hat{z}^2 \rangle} \right) U(\hat{\boldsymbol{x}}), \tag{3.20}$$

where $U(\hat{\boldsymbol{r}}) = \frac{PV\epsilon_c}{2c\sigma_L}|u(\hat{\boldsymbol{r}})|^2$ is the optical potential, P is the laser power, c is the speed of light, V is the volume of the particle, $\epsilon_c = 3\frac{\epsilon_R - 1}{\epsilon_R + 2}$, ϵ_R is the dielectric function, ω_z is the frequency at which the feedback is applied with a phase offset Θ,

$$u(\hat{\boldsymbol{r}}) = \frac{w_0}{w(\hat{z})} \exp\left(-\frac{a_1\hat{x}^2 + a_2\hat{y}^2}{w(\hat{z})^2}\right) e^{ik\hat{z}} \tag{3.21}$$

is the mode function, w_0 is a characteristic length of the Gaussian beam profile, a_1,a_2 quantify the degree of asymmetry in the trapping potential along the x,y axis, respectively. $w(\hat{z}) = \sqrt{1 + (\frac{\hat{z}}{z_R})^2}$, z_R is the Rayleigh range, $k = \frac{2\pi}{\lambda}$, λ is the laser wavelength (1550nm), β is an adimensional parameter quantifying the strength of the feedback term, ω_z is the frequency of the particles oscillation, and m is its mass.

The overall volume that the trap occupies is considered to be conserved such that $a_1 a_2 = w_0^2$

Depending on Θ the system can be either driven, cooled or cooled by the feedback term. Or modulated to display other intermittent motional states (see Appendix F or chapter 6 for more details).

The terms on the second line of Eq. (3.18) quantify the interaction with the gas particles according to the dissipative Caldeira-Leggett model [113, 114] (A quantum mechanical analogue of a diffusion equation), where $\gamma_c = \frac{\pi p_g r_g^2}{\sqrt{8 m_g k_B T}}$, is a characteristic collision rate, p_g is the gas pressure, r_g and m_g are the radius and mass of a gas particle, respectively, k_B is Boltzmann's constant, T is the gas temperature, $\mathcal{D}[\hat{K}]\cdot = \hat{K}\cdot\hat{K}^\dagger - \frac{1}{2}\{\hat{K}^\dagger\hat{K}, \cdot\}$ [115], and $\hat{K}$ is an operator.

On the third line of Eq. (3.18) the first term quantifies the decoherence due to gas scattering, where $\gamma_s = \frac{\sigma_R}{\sigma_L}\frac{P}{24\pi\hbar\omega_L}$ is the Rayleigh rate, $\sigma_R = \frac{24\pi^3 V_0^2}{\lambda^4}\epsilon_C^2$ is the Rayleigh cross-section, ϵ_R is the dielectric function, $\hat{A}_{\boldsymbol{n},\nu} = \boldsymbol{\epsilon}^{*\top}_{\boldsymbol{n},\nu}\boldsymbol{\epsilon}_d u(\hat{x})e^{ik\hat{z}}$ is the Rayleigh scattering operator, ν denotes the polarization, and $\boldsymbol{n}$ denotes a unit vector. W is a zero mean Wiener process with correlation $\mathbb{E}[dW dW] = S dt$, where $\mathbb{E}$ denotes the average over different noise realizations, and $\mathcal{H}[\hat{K}]\cdot = \hat{K}\cdot + \cdot\hat{K}^\dagger - \mathrm{tr}[\hat{K}\cdot + \cdot\hat{K}^\dagger]\cdot$ [115]. The validity of treating the background gas collisions that the particle encounters experimentally as a Weiner process mathematically is explored in Appendix A, where the assumption is found to be mostly justified.

The second term corresponds to the detection, where $\hat{B} = \sum_{k+l+m\leq n} s_{klm}\hat{x}\hat{y}\hat{z}$ is the measuring operator. Although the values of s_{klm} and S could in principle be determined from the experimental setup, i.e. the optical elements and the detector, these values are fixed using the measured signal. It is necessary to include such a detection function since the photons-volts-metres conversion factor (section 1.9.1) is different not only for each Cartesian axis of the levitated particle, but also for any mechanical harmonics or non linear motional modes displayed by each degree of freedom. The second part of this is intuitively consistent with the result that the conversion factor changes with the frequency, and thus mean displacement of the oscillator.

The detected photo-current associated to Eq. 3.18 is given by:

$$dI = \sqrt{\eta\gamma_s}\mathrm{Tr}[\left(\hat{B}e^{i\Delta\phi} + \hat{B}^\dagger e^{-i\Delta\phi}\right)\hat{\rho}_c] + dW, \tag{3.22}$$

where $\Delta\phi$ is the phase of the local oscillator.

To numerically simulate the model we approximate the dynamics using a classical model. We suppose the description of the state is given by its mean position $\langle\hat{\boldsymbol{r}}\rangle$ and its mean momentum $\langle\hat{\boldsymbol{p}}\rangle$, which, loosely speaking, corresponds to assuming that the system is always well-localized. In addition, we assume that the optical detection, as well as photon scattering, do not significantly perturb the system, apart for the classical radiation pressure force. We drive the system using the feedback term to the non-linear regime, where the cross terms of the optical potential couple the translational degrees of freedom. These couplings can be seen explicitly by Taylor expanding the optical potential. At order $\mathcal{O}(|\hat{\boldsymbol{r}}|^2)$ we find the harmonic terms $\frac{m\omega_x^2}{2}\hat{x}^2$, $\frac{m\omega_y^2}{2}\hat{y}^2$, $\frac{m\omega_z^2}{2}\hat{z}^2$, where $\omega_x^2 = \frac{2Pa_1}{c\sigma_L\rho w_0^2}$,$\omega_y^2 = \frac{2Pa_2}{c\sigma_L\rho w_0^2}$,$\omega_z^2 = \frac{2P}{c\sigma_L\rho z_R^2}$ are the harmonic frequencies, and ρ is the density. At order $\mathcal{O}(|\hat{\boldsymbol{r}}|^4)$ we find the non-linear terms $N_\mathrm{x}\hat{x}^4$, $N_\mathrm{y}\hat{y}^4$, $N_\mathrm{z}\hat{z}^4$, where $N_\mathrm{x} = -\frac{PVa_1^2}{4c\sigma_L w_0^4}$,$N_\mathrm{y} = -\frac{PVa_2^2}{4c\sigma_L w_0^4}$, $N_\mathrm{z} = -\frac{PV}{2c\sigma_L z_R^4}$, as well as the following couplings terms:

$$U_\mathrm{xyz}(\hat{\boldsymbol{r}}) = C_\mathrm{xy}\hat{x}^2\hat{y}^2 + C_\mathrm{xz}\hat{x}^2\hat{z}^2 + C_\mathrm{yz}\hat{y}^2\hat{z}^2, \tag{3.23}$$

where $C_\mathrm{xy} = -\frac{PVa_1a_2}{2c\sigma_L w_0^4}$, $C_\mathrm{xz} = -\frac{PVa_1}{c\sigma_L w_0^2 z_R^2}$, and $C_\mathrm{yz} = -\frac{PVa_2}{c\sigma_L w_0^2 z_R^2}$. The potential U_xyz, which couples the translational degrees of freedom, can be exploited to give rise to the Fano effect as well as for sympathetic cooling.

3.5 Experimental implementation

We optically trap a 60 nm radius SiO_2 nanoparticle in the focus of a high numerical aperture (NA = 0.9) parabolic mirror, consistent with the methods employed in [116] [80], with trapping laser wavelength and power of 1550nm and 1 W respectively. The beam has a Gaussian spacial profile. The particle scatters some of the laser light: the backscattered light is reflected by the mirror and directed, using optical elements, towards a beam splitter. There it is combined with a local oscillator, and then detected in a balanced homodyne detection setup figure 3.5.

Coupling by optical driving is achieved at 10^{-2} mbar , while coupling via high voltage (HV) electric fields is achieved at 10^{-6} mbar. A schematic diagram of the optical setup is given in figure 3.5. Both the optical and electrical driving experiments use the same optical path, however in the optical driving case the HV needle is simply not used.

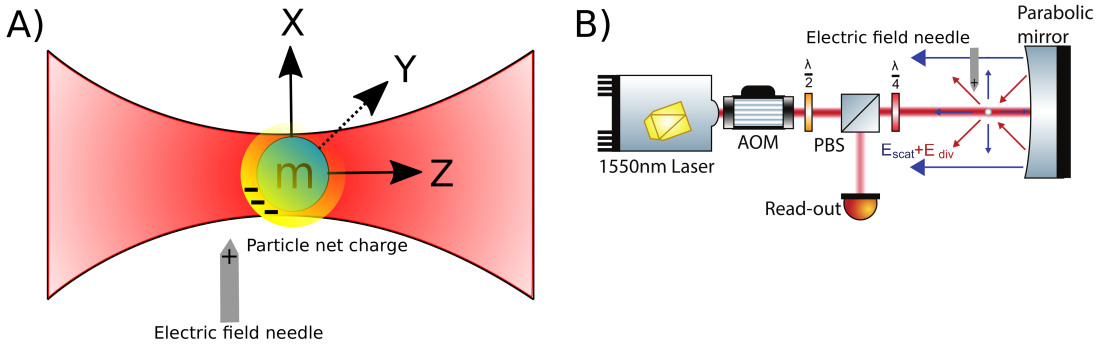

FIGURE 3.5: (A) Conceptual diagram of an optically levitated nanoparticle of mass m, with translational degrees of freedom x,y and z. A high voltage field needle is place such that it is non orthogonal along at least two axes (B) Experimental setup diagram. A fiber acousto-optical modulator (AOM) is used to modulate the light coming from a 1550nm fiber laser, which then passes though a $\frac{\lambda}{2}$-wave-plate, a polarizing beamsplitter (PBS) and a $\frac{\lambda}{4}$-wave-plate. After reflection by the parabolic mirror the laser light $\mathrm{E}_{div} + \mathrm{E}_{scat}$ is guided though the $\frac{\lambda}{4}$-wave-plate again before it gets reflected by the PBS. The read-out is done via a balanced photodiode. In the first experiment the translational modes of the nanoparticle are coupled by the intrinsic cross terms in the Gaussian optical potential experienced by the nanoparticle. In the second experiment the translational modes are coupled by applying a high voltage DC electric field non-normal to the axis of the particles translational modes.

In our system we generate an anti resonance between two coupled motional peaks or frequencies than would otherwise exhibit symmetrical lorentzian lineshape. Via the Fano resonance interaction, both interacting oscillators transform their lineshapes, with the 'first' oscillator in the interaction picking up an additional asymmetrical motional peak with the characteristic Fano like negativity.

The Fano resonance is generated at 10^{-2} mbar by picking two close motional peaks and varying the driving parameters until the correct ratios of oscillator driving and springs are found by systematically trying all possible input combinations until particle loss occurs.

The conceptual motivation for attempting to generate this effect in our system is given in figure 3.3.

3.6 Experimental results

3.6.1 Optical driving - Antiresonances

In the first case we couple the nanoparticles modes into an antiresonance by driving the z degree of freedom at its resonant frequency with an AOM and a phase lock loop. With

zero driving power we find the expected 3 decoupled motional degrees of freedom of the nanoparticle.

When the driving power is increased to substantial levels, we find additional higher frequency modes being generated 3.6. By virtue of these additional modes having a separate phase evolution, as well as their ability to coupled to the prime mode, we make the statement that these modes are genuine mechanical motions of the particle rather than optical frequency mixing in our detection system. Henceforth we use the naming system z1, z2, z3 to describe the fundamental, 1st and 2nd higher order mechanical modes of z.

For a sufficiently high values of optical driving, we find by use of a correlogram that the mode z2 forms an antiresonance lineshape, and becomes highly correlated with the z1 motion, indicating strong coupling between the modes. Furthermore, an additional mode z3 appears, and the temperature of the x degree of freedom is lowered significantly.

While the Fano resonance between two classical driven damped oscillators can be understood by a simple analytical mode, such as that given in [101]. When multiple coupled oscillators are involved however, we find such an approximation to be insufficient, and must instead numerically simulate the equations of motion for the particle numerically, discussed in section 3.4.1. Fitting the output of such a simulation to the obtained experimental data gives the fits located in figure 3.6. Strictly, the model derived in section 3.4.1, describes only the mechanical motion of the particle, and to obtain full fits we include a model for the nonlinearity in our detection system.

3.6.2 Sympathetic cooling

In addition to the antiresonance lineshapes in the Z degree of freedom, by varying the strength sinusoidal driving applied to the z motional degree of freedom, we find a driving strength dependant cooling interaction between the z and x degrees of freedom of the nanoparticle.

As the magnitude of the parametric driving on the z-motional degree of freedom is increased, the magnitude of motion in the x degree of freedom is decreased. An effect similar to sympathetic cooling [117], but between different motional modes of the same oscillator rather than different oscillators.

The dependence of the strength of this sympathetic cooling mechanism is a continuous process as a function of the driving power on the z degree of freedom. For each incremental increase in the parametric drive applied to z degree of freedom we find a

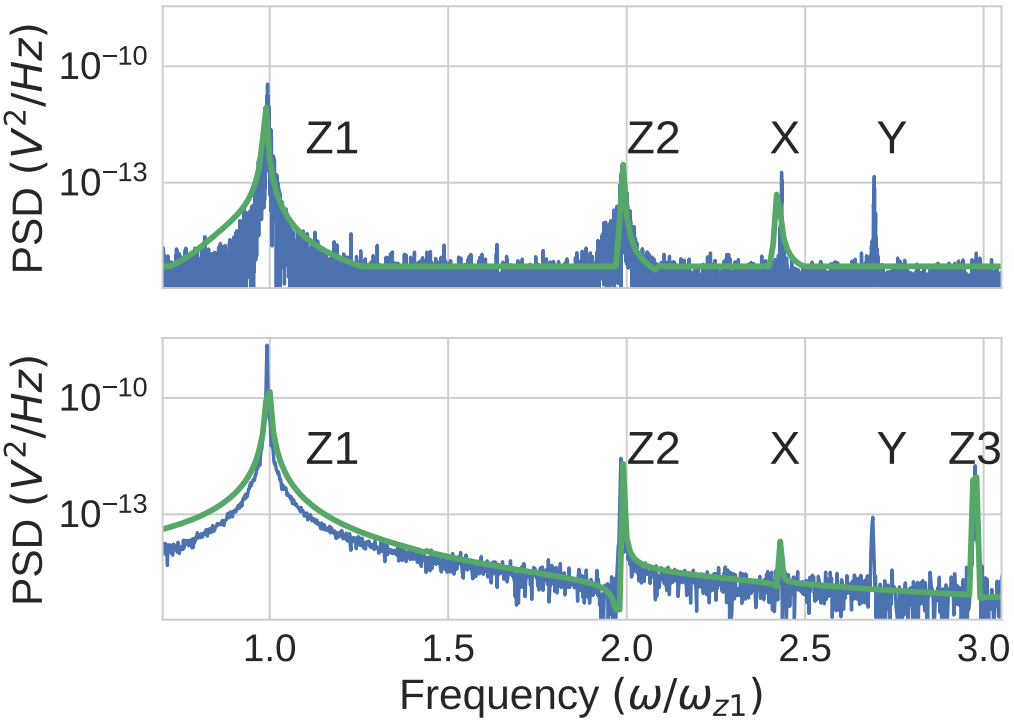

FIGURE 3.6: **Experimental data:** Matching the output of the numerically solved stochastic differential equations of motion, section 3.4.1, with experimentally obtained data for driving conditions before and after the anti resonance conditions are met gives the above fits. Driving conditions before the anti resonance (top) and after the optical driving strength required to generate the antiresonance (bottom). Note the anti asymmetric line shape in Z2 after the resonance combined with suppressing the motion of the particle in a specific frequency below the previously existing mechanical noise floor. Furthermore numerically simulating the equations of motion allows us to replicate the cooling effect upon the X degree of freedom.

corresponding decrease in the energy of the x motional degree of freedom, shown in figure 3.7.

This is in contrast to the conditions required for the Fano resonance to occur, which appears discreetly above a certain value of driving in the z degree of freedom. This is an intuitive result, as when energy oscillator and a lower energy oscillator are coupled, the starting conditions for energy transfer from the high energy oscillator to the low energy oscillator are numerous, while the requirements for an anti-resonance to occur are more specific, summarized in [100].

3.6.2.1 Sympathetic cooling strength

At an experimental pressure of 10^{-2} mbar, the temperature limit of the sympathetic cooling technique reduces the temperature of the x and y degrees of freedom to around 1K each. As is the case with parametric feedback cooling, the ratio of heating and cooling

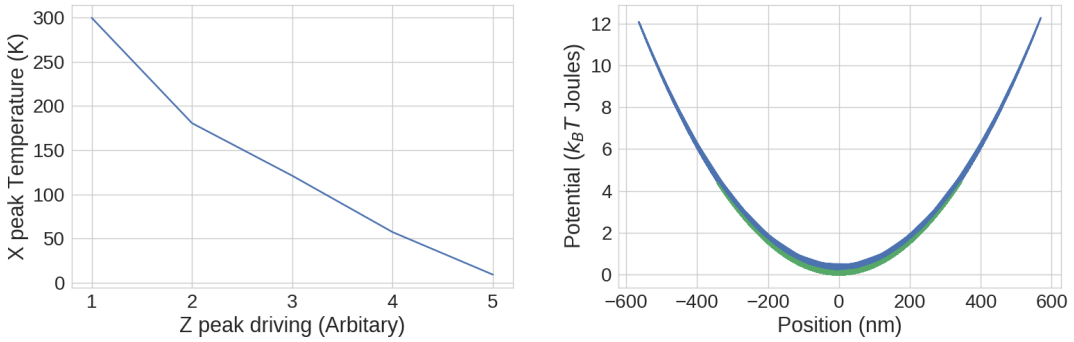

FIGURE 3.7: **Experimental data:** (left) Temperature of x-axis vs optical driving power incident on the z-axis. As driving power on the z motional degree of freedom in increased and the conditions for the Fano resonance approach the amplitude of the prime motional frequency for the x-direction decreases. This can be interpreted as a sympathetic cooling mechanism. Harmonic motion in the x-axis remains harmonic during cooling.(Right) Reconstructed x-axis potentials before and after resonance. Net cooling is obtained, and the trap remains linear after cooling occurs, so the temperatures before and after cooling are comparable.

channels determines the final temperature. Heating due to background gas collisions is the dominant heating process at this pressure [92].

It turns out that the magnitude of the sympathetic cooling factor obtained is heavily dependant on the relative phase of the oscillators in the system. As only the z degree of freedom is controlled externally in the present experiment, the relative phase of the x degree of freedom varies significantly over time. This caused the temperature of the cooled x degree of freedom to varying substantially, on the characteristic timescale of seconds, figure 3.9. The clear implication of this is that the phase of the X degree of freedom would likely have to be controlled externally for the technique to be maximally efficient.

Whilst the final external temperature of the nanoparticle reached in this interaction is unimpressive due to the experiment taking place at relatively high pressure, we can still estimate the actual cooling power by comparing the temperature reached for this pressure against the final temperature obtained by parametric feedback at the same pressure. In [92] an occupation number of $< n_{thermal} >= 2 \times 10^6$ for a pressure of $10^{-2} mbar$, whereas in our case we compute a an average thermal occupation number (for the optimum value of x-y degrees of freedom phases) of $< n_{thermal} >= 4.5 \times 10^6$. While a worse value this is fairly encouraging as it implies the two techniques are at least comparable, and the sympathetic cooling is almost completely undeveloped whereas the stated parametric value remains the (presently published) state of the art system within the field.

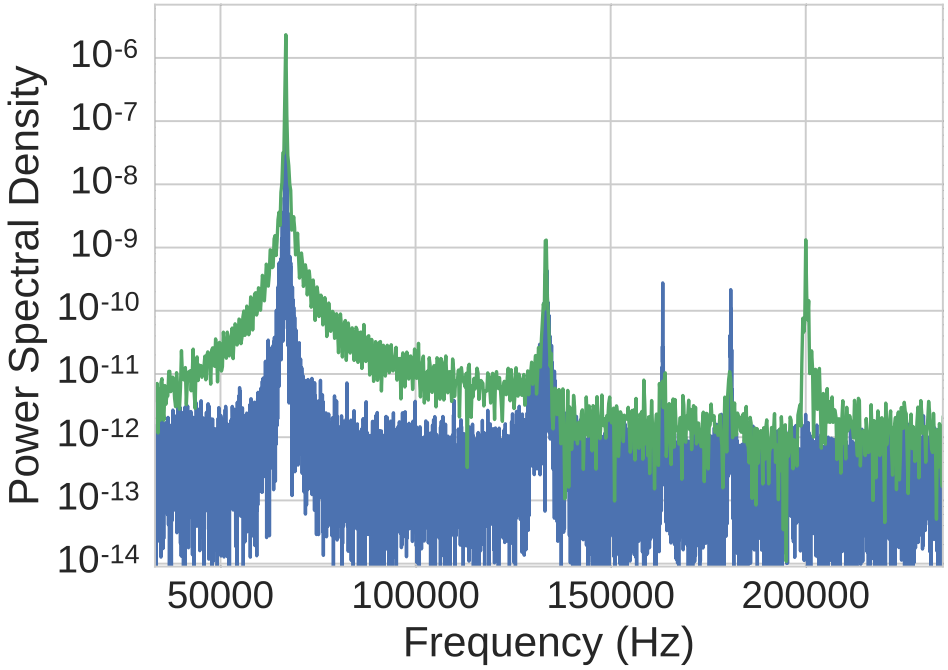

FIGURE 3.8: **Experimental data:** Optical limit of sympathetic cooling at a pressure of 10^{-2}mbar appears experimentally to be at a temperature of around 1K. In this example both the x and y degrees of freedom are cooled substantially by their interaction with the Z degree of freedom. Uncooled dataset (blue), cooled dataset (green). Note that the x and y peaks are substantially lower in the case of the green dataset.

An interesting question for any future research to answer with regards to sympathetically cooling in this way is whether or not the technique can be stacked with other cooling channels. In the formulation used in section 1.4, is the configuration:

$$< n_{th} >= \frac{\gamma_{parametric feedback} + \gamma_{sympathetic damping}}{\Gamma_{Heating channels}}, \tag{3.24}$$

possible, and if it is would it provide a net benefit to the cooled degree of freedom to use both cooling channels at the same time. Also, would the formulation of the system still remain sufficiently valid to treat it as a harmonic oscillator for the purpose of computing the occupation value in such a case.

3.6.3 Electric field coupling

Generating a Fano resonance with the intrinsic Gaussian optical cross coupling is achieved by driving the particle to large motional amplitudes in at least one degree of freedom. Experimentally, this appears to only be sustainable at relatively low vacuum pressure,

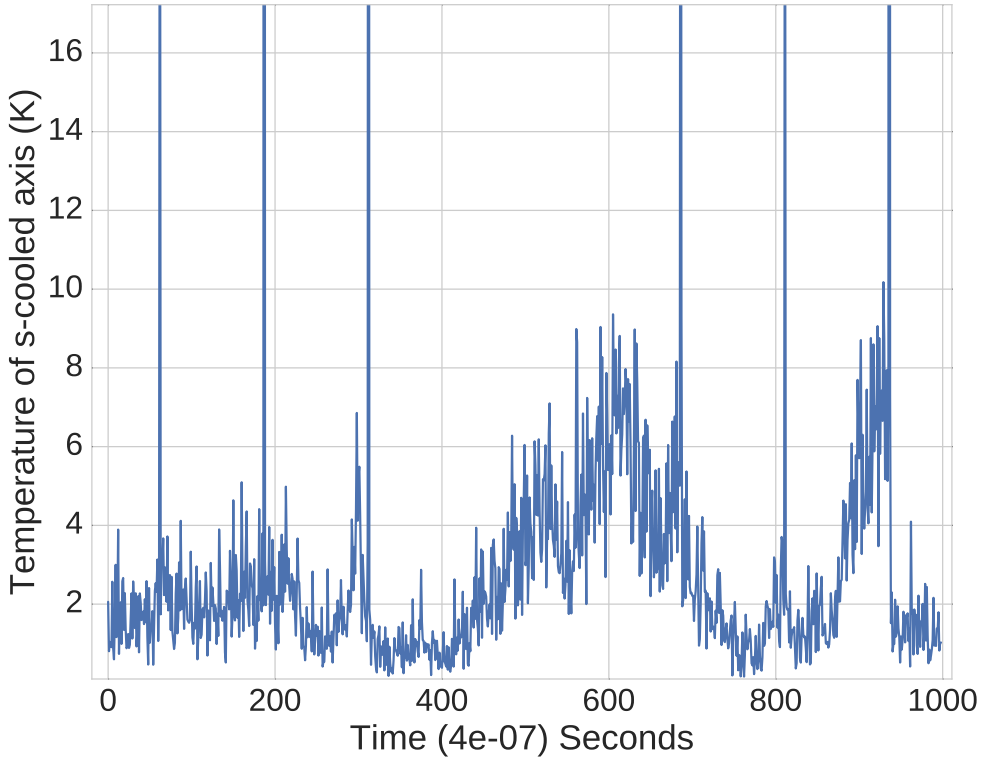

FIGURE 3.9: **Experimental results:** Temperature of the x-y degrees of freedom fluctuates over time for the same value of driving, background gas collisions heat the particle as well as changing the relative phases of the degrees of freedom. As the phases of the x and y degrees of freedom change as a result of background gas collision, they are no longer in a sympathetic cooling solution with the rest of the system, resulting in a fluctuating temperature over time.

10^{-2} mbar, as driving the particle to the required amplitudes to achieve the effect at high vacuum generally results in particle loss. We found experimentally that an anti-resonance effect be also be induced at high vacuum, 8×10^{-5} mbar, by applying an electric field in a similar fashion to [47], using a steel needle that is offset from the center of the trap in z and y, see diagram 3.5. The voltage applied to the needle is swept from 0 to 10 kV and the effect this has on the shape of the z frequency is shown in Fig.(3.10).

Due to the dramatically lowered rate of background collisions the particle experiences at lower pressure, the phase of each oscillator, and therefore the relative phase between the degrees of freedom of the particle changes at a much slower rate, allowing the same type of anti-resonance to be maintained for longer. In principle, this along with the lower pressure implies that the sympathetic cooling effect observed in section 3.6.2 could be applied to competative values to parametric feedback. Furthermore, due to direct control over the coupling value, the depth of the antiresonance effect (and thus the Fano parameter), can be controlled by simply varying the voltage on the applied field.

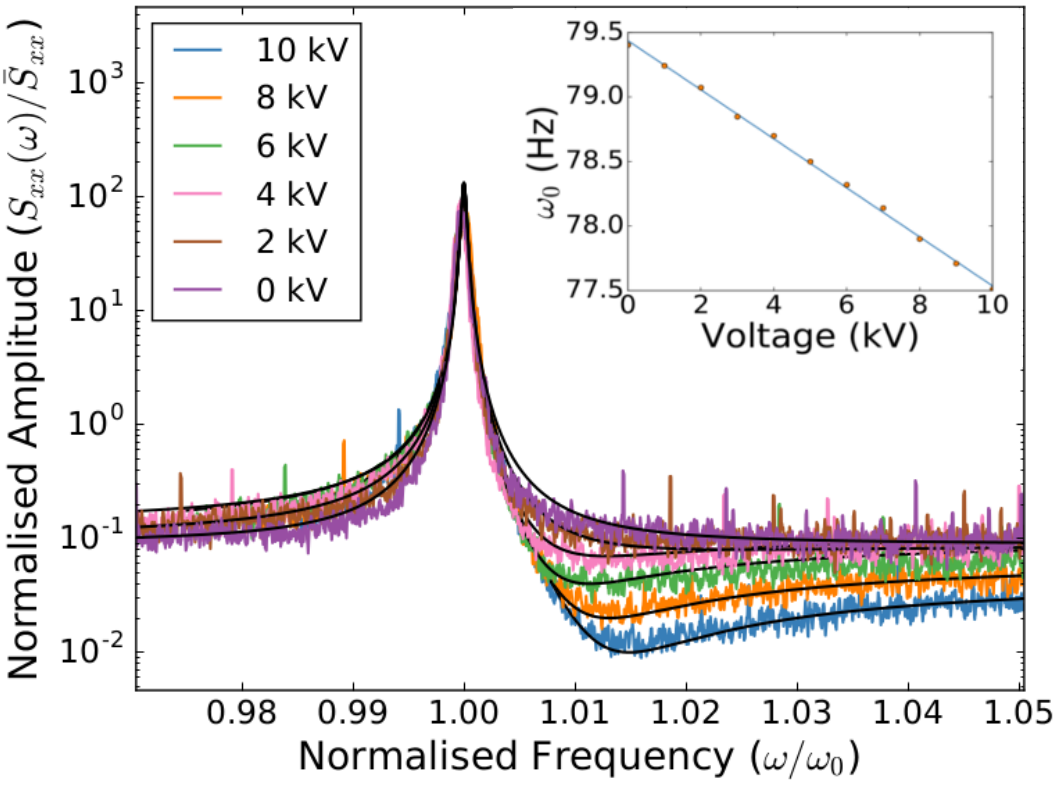

FIGURE 3.10: **Experimental data:** Nanoparticle optically levitated at $10^{-}6$ mbar exposed to electric fields of 0 to 10 kV. Increasing the field strength and thus the coupling between modes leads to a stronger anti resonance effect. From unpublished work in collaboration with D.Hempston. The maximum drop in the power spectral density is 9 V^2/Hz. The function fitted to the data is equation 3.2.

3.6.4 Anti resonance window reversal

As discussed in section 3.3.2.1, the oscillations taking place on the left and right hand side of the resonant peak have opposing phases therefore, if the couplings in the potential are reversed, the opposite mechanics phases of the oscillator will 'feel' each others motion, and the antiresonance will flip to the other side of the peak. This effect can be seen in figure 3.11. A similar effect can also be induced in the optical driving case by choosing the energy evolution of the system, with a let handed anti-resonance corresponding to a system decreasing in energy vs a right handed antiresonance corresponding to a system increasing in energy over time.

3.6.5 Physical interpretation of the PSD reduction at the antiresonant frequency

At the frequency of the antiresonance, the particle's motion is suppressed. Since the system is well described as a driven damped oscillator interacting with a random noise

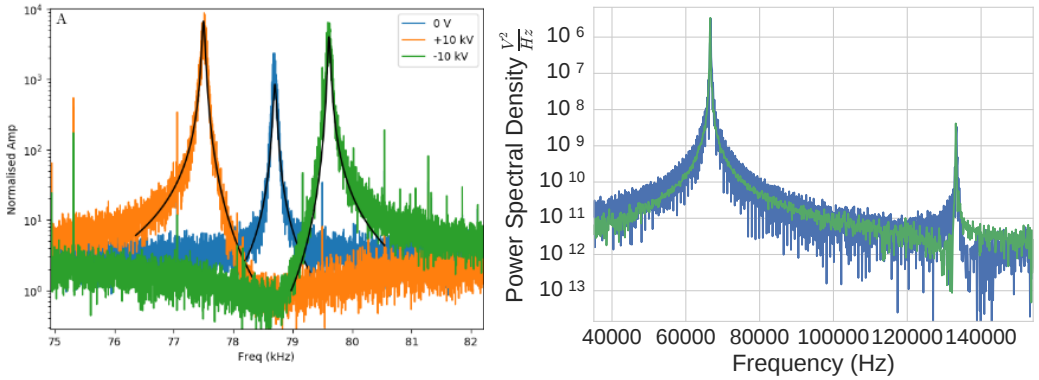

FIGURE 3.11: **Experimental data:** *Left:* Nanoparticle optically levitated at $10^{-}6$ mbar with an High Voltage electric field applied non orthogonally to the degrees of freedom of system. Switching the polarity on the applied field reverse the sign of the coupling terms in the non linear potential and thus flips which side of the resonance the frequency suppression effect appears on. From unpublished work in collaboration with D.Hempston. *Right:* A similar reversal of the Fano resonance window, in the case of optical rather than electrical driving. In this case the couplings between the degrees of freedom are reversed in sign by different relative phases between the degrees of freedom. This corresponds to a phase shift of $\frac{\pi}{2}$ between the z1 and z2 degree of freedom, see waveforms B and D in figure 3.2

field, the particles' motion at each frequency ω is determined by the susceptibility of the oscillator, and the density of background gas collisions at a given frequency.

The noise floor visible in the power spectral density of the particles' motion is composed of noise from several sources. Noise from the experiments optical and electronic components, as well as the random collisions with background gas molecules, are all likely to manifest as their own noise floors.

Since the antiresonance interaction drives the values of the PSD at the antiresonant frequency below the noise floor observed by the Lorentzian resonances in the PSD, its fair to say that the interaction suppresses the random motion of the particle (at that frequency) as well as the non random motion. Therefore, the mechanical noise floor of the particle, is suppressed at the antiresonant frequency, to a degree determined by the strength of the Fano interaction.

3.7 Fano resonance applications

3.7.1 Cooling

The simple Fano interaction described in the section 3.3.2.1 takes places between two mechanical oscillators, however, in the case of the actual experimental system, and

indeed the one simulated by our SDE model, several nonlinear affects manifest at once. One of these being significant coupling between the x and y peaks to Z system, in such a set of conditions that the x and y peaks are cooled sympathetically by coupling to the mechanical motion of the Z system.

As the Z system is extracting energy from the x and y peaks, this in principle represents something akin to sympathetic cooling in optomechanical system, albeit between two different degrees of freedom of the same oscillator, rather than two separate objects.

An obvious and interesting question lies in what might be the ultimate limit of this effect. Initial experiments obtained an order of magnitude of ground state cooling, however since this was an unexpected outcome of the experiment, the best possible outcome is likely to be higher. One particularly motivating element of using mechanical modes to cool other mechanical modes in this fashion is that such a cooling channel would not be limited by photon recoil in the axis that the cooling effect is applied to, the current dominant limit in optical feedback cooling [64]. Indeed, theoretical proposals already exist in the community to cool nanoparticle motion using Fano resonance type effects [110] by utilizing the antiresonance frequency window to suppress heating processes.

The practical application of this resonance effects as a cooling channel however will require replication of the coupling effect at high vacuum (as all efforts to reach the quantum ground state rely on a low contribution from random fields such as background gas collisions), which experimentally has been easier to achieve by using high voltage electrical field rather than optical driving. An important consideration might be that as the degree of the sympathetic cooling is dependent on the coupling between the two oscillators, which is in turn dependent on the strength of non linear cross terms in the potential, anything above a certain strength of nonlinearity will naturally drop the particle. Thus, some careful potential design may be required to sympathetically cool below a certain value.

3.7.2 Sensing

It seems natural to suggest that a sharper line width that the standard Lorentzian will allow better frequency determination of an unknown signal coupled to the Fano resonance peak of the nanoparticle motion.

In the case of, for example a signal of unknown frequency ω interacting with a Lorentzian resonant peak, the precision to which we can identify that frequency by its interaction with the peak in a certain integration time is dependent on the gradient of the response function of the peak with respect to frequency. An experimental proof of this idea is

given in [103], in which a Fano lineshape enhances the minimum sensitivity of a system by an order of magnitude.

3.7.3 Optomechanical logic

In the field of optoelectronics, Fano lineshape effects are often used for frequency switches[104–106]. Since a switching effect is one of the first requirements for a logic gate [118], constructing optomechanical logic elements by using anti-resonance effects does not seem unreasonable.

3.8 Chapter conclusion and outlook

In conclusion we experimentally demonstrate a controllable Fano resonance between two degrees of freedom of a levitated nanoparticle. In addition to the creation of the characteristic asymmetric line shape this also provides a sympathetic cooling channel between the translational degrees of freedom of an optically levitated nanoparticle.

The coupling mechanism between the degrees of freedom is given in the first case by cross coupling terms between degrees of freedom in non linear region of the optical trap, occurring when the distance travelled by the nanoparticle becomes such that the nanoparticle leaves the harmonic x^2 approximation of the Gaussian beam focus. We also induce an antiresonance effect by artificially coupling the degrees of freedom of the nanoparticles motion by applying an electric field with component orthogonal to both relevant degrees of freedom.

As the interference effect is between the motional degrees of freedom of the same nanoparticle, the characteristics defining the line shape, equations (3.11) and (3.12), no longer have any dependence on mass, assuming the particle is to a good approximation spherical, potentially allowing for better future classification of the nanoparticle properties themselves, such as the mass of the levitated object, on which the present error bars are presently fairly large in the field. Furthermore, the more complex lineshape should allow for better extraction of the other physical parameters in the system, such as the fundamental light-matter coupling, a quantity that has thus far been reasonably elusive in non cavity levitated nanoparticle experiments.

Future work will entail identification of the coupling effects between the axis, clarification if the coupling effect is pressure dependant and, if the effect is dependant on background gas collisions, testing to see if coupling with a common optical mode or electric field projected non orthogonal across each axis. If the effect is reproducible at

low pressure with either electric fields or optical driving then coupling via gas collisions seems unlikely.

Chapter 4

Periodic optical multiwell potentials

4.1 Chapter Overview

The generation of a periodic multiwell potential through spatial optical manipulation is detailed and the generated potential structures are matched to ray tracing simulations of the optical setup.

4.2 Motivation

The controllable generation of custom non linear potentials in both time and space is of considerable interest to the optomechanics community at present [18] [119][120][11]. These have applications from the study of fundamental physics [58] to sensing [121] and secure communications [120].

In this section we demonstrate the generation of multiple potential wells in a manner similar to the recently published work [58], and observe the particle hopping between them. In addition, we generate a periodic potential on a scale less than the average thermal motion of the particle and note that it generates an additional nonlinear term in the dynamics of the particle that is not of Duffing (cubic in the position term) type. We characterise this system in terms of its phase-space, Poincare sections, stability, energy evolution and RQA (recurrent quantification analysis) metrics[122].

4.3 Spatial non linearities

4.3.1 Optical double well

4.3.1.1 Conceptual implementation and equations of motion

In the case of a double well, the potential would take the form:

$$V(x) = -\frac{x^2}{2} + \frac{x^4}{4} \tag{4.1}$$

for a driven damped oscillator traversing that well, this leads to the equation of motion

$$x'' = x - \lambda x^3 - \gamma x' + dcos(\omega t) \tag{4.2}$$

in which γ is the the damping on the particle, w is the natural frequency of the system, d is the driving field and the driving frequency is ω. λ is the Duffing parameter and represents the amount of (cubic in position) non linearity in the system and along with the driving forms the parameter space required to search for chaotic motion in a system.

A conceptual diagram of the possible motional modes in a double well system is shown in figure 4.1, motional modes B and C may occur when the potential wells are adequately separated, whilst mode A may occur when the wells are close together.

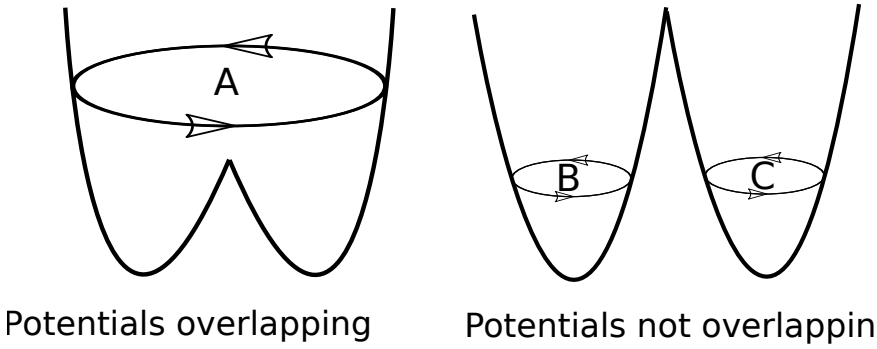

FIGURE 4.1: Conceptual representation of double well potential and the possible motional modes enabled by such a potential structure. When the wells are separated significantly the particle may undergo motion a linear state in either well (modes B and C) or with the possibility to jump between the wells. When the wells are significantly closer than $\lambda/2$ (the range of thermal motion of the particle) the system is better described as a Duffing oscillator (equation 4.2) than linear motion.

4.3.2 Experimental implementation

In order to realize an optical double well in our system we trap a mesocopic optical silicon dioxide nanosphere of radius 60 nm at the focus of a parabolic high NA reflective objective in a manner consistent with [123]. We then increase the divergence of the incoming beam in order to move the centroid of the focus out of the plane of the mirror, moving the nanoparticle while simultaneously perturbing the shape of the focus generated by the mirror in space, demonstrated in figure 4.3. The change in the geometry of the focus is nonlinear, creating multiple trapping sites, with specific values of angle along the optical axis giving rise to multiple traps being close enough to form a double well potential 4.3.

Specifically, increasing the divergence of the optical beam gives rise to a wide family of potentials symmetric around the angle of the optical axis but periodic in normal distance away from it. When the radial symmetry of this system is broken by misalignment of the optical axis from the center of the trapping paraboloid mirror, double and triple wells isolated in one direction of the particle's x,y,z motion become possible.

4.3.3 Numerical simulation - double well

4.3.3.1 Ray tracing simulations - estimating potential structure

While the exact potential structure can be readily extracted using the methods detailed elsewhere in this thesis, as the nanoparticles are trapped using optical only traps defined in a far field focus (and thus its shape and intensity are approximable by ray optics), it should be possible to simulate the optical density and thus potential structure for an arbitrary optical configuration than the Gaussian potential traps used elsewhere in this thesis. Doing so should allow us to see what families of potentials, and therefore nonlinearities and chaotic attractors, we have access to via simple optical operations like playing with the divergence and alignment of the trapping mirror. It will also likely inform future work on using an spatial light modulator (SLM) to construct genuinely bespoke potentials, with more freedom than optical components without spatial phase control allow.

Ray tracing a divergent light field with minor misalignment in the x and y optical axis readily produces a double well potential, of which a top down slice through the x y plane is displayed in figure 4.2 and the histogram of density along the x plane is displayed in figure 4.2.

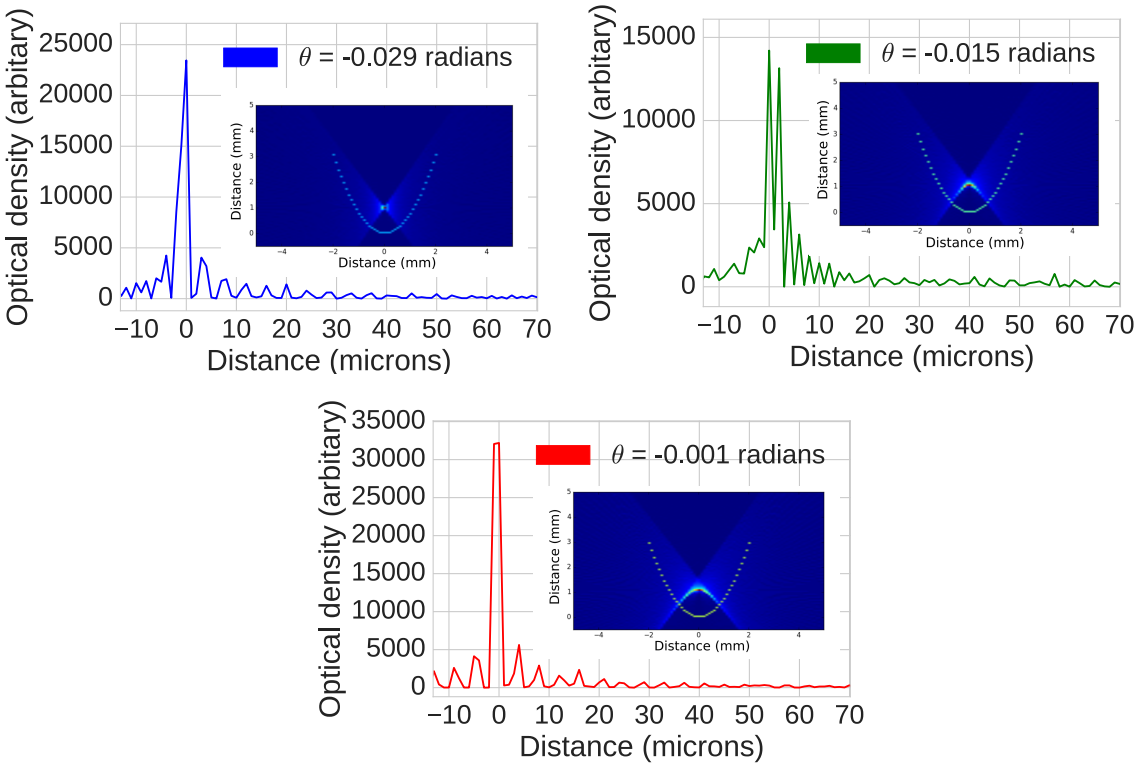

FIGURE 4.2: **Simulation** Ray tracing simulations for a Gaussian beam incident on a parabolic mirror. Initially the beam is completely collimated, leading to a single focus (red). As the angular convergence of the incident beam in increased eventually multiple traps form (green), before the system reverts to a single focus again (blue). A slice of the optical density through the z-x plane is given as the graphed data to visually demonstrate the appearance of multiple traps whilst the heatmaps of the optical density produced by the raytracing are given in the inserts for each value of the collimation angle. As the angular convergence of the beam changes, the average focus also moves out from the center of the parabolic mirror, shown in the inset heatmaps. Density is arbitrary and unitless in this simulation.

4.3.3.2 Stochastic differential equation (SDE) simulations of particle in a double well potential

Is it possible to simulate the motion of our particle for nonlinear potentials numerically, and thus compute the expected phase space distribution for our periodic potential.

Adding a random noise field (represent the stochastic driving of the particle by various heatbaths) to the previous equation of motion derived for a Duffing oscillator in a double well gives us:

$$x'' = x - \lambda x^3 - \gamma v + dcos(wt) + \eta(t). \tag{4.3}$$

where $\eta(t)$ gives the magnitude of the random noise field. By treating this as a stochastic differential equation (SDE), we can use a stochastic extension of the Runge-Kutta method of solving ordinary differential equations (ODE's) to simulate the particles motion in the double well. Tuning the nonlinearity, Duffing and driving parameters allows us to roughly match the output of simulation and experiment.

4.3.4 Analysis of experimental data from multi well potential.

The experimentally time trace of the trapped particles motion (figure 4.3 top) suggests the potential wells are physically separated in space, with the particle jumping between them. Analysis of the Fourier transform, figure 4.3 bottom, of the motion of the trapped particle in the centre macroscopic well, indicates that the overlap of the mutliple focii has generated a periodic potential in the center well, similar to the double well experience by a Duffing oscillator.

The phase space of the nanoparticles motion in the multliwell potential shows the expected multiple peaks in the positional distribution of an otherwise thermal state, figure 4.4.

4.3.4.1 Simulated equation of motion vs Experimental results.

Comparing the simulated and obtained phase spaces for a particle in a double well potential, we find similar phase space distributions, figure 4.4.

The lack of complete matching in phase space is due to oversimplification of the potential structure, which we show in section 4.4 to be triple welled, rather than the double well structure assumed by a duffing nonlinearity. Future work could well entail the numerical acquisition of the potential structure from experimental data to feed into such simulations.

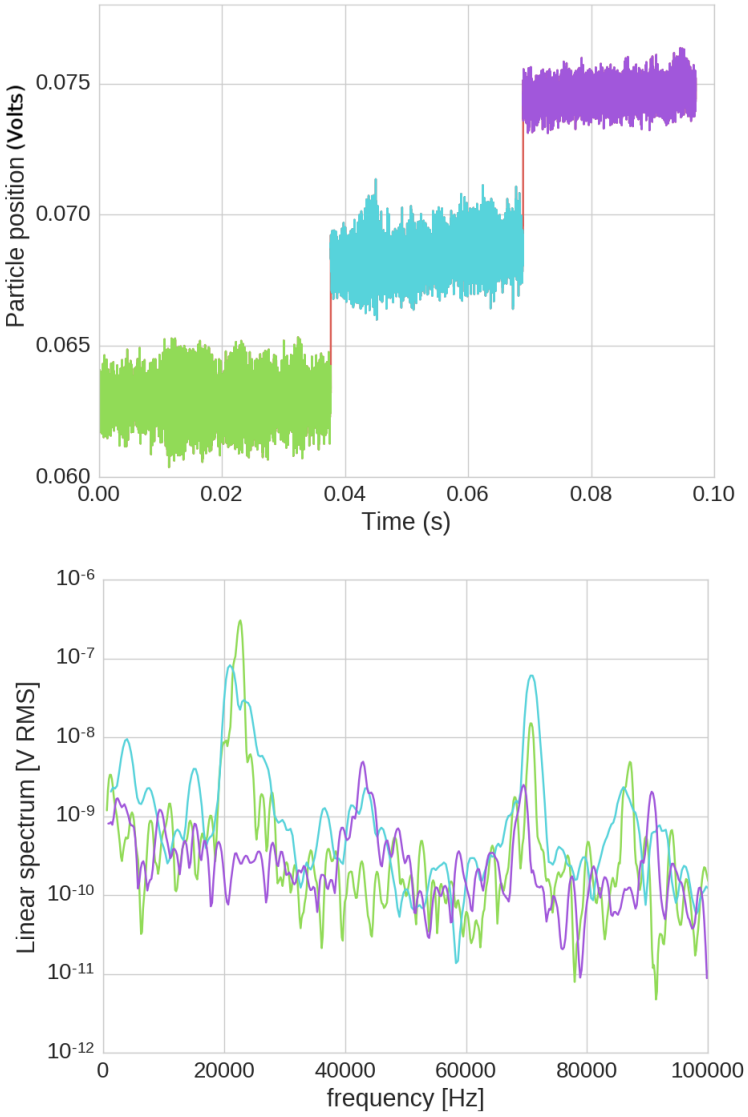

FIGURE 4.3: **Experimental data:** Positional time traces of a particle jumping between potential wells and the resultant Fourier spectra. The central level displays the Z frequencies associated with the upper and lower levels. Noting that the colours are conserved between the upper and lower sections of the plot, the trap physically in the middle of the other two traps (blue) displays two z frequencies, often characteristic of a double well system. The green and purple traps are both linear single welled systems, whilst the blue time trace is the triple well system mapped out in figure 4.5. The displacement is given in volts for the upper dataset as the volts $\rightarrow$ metres conversion factor differs for each potential well.

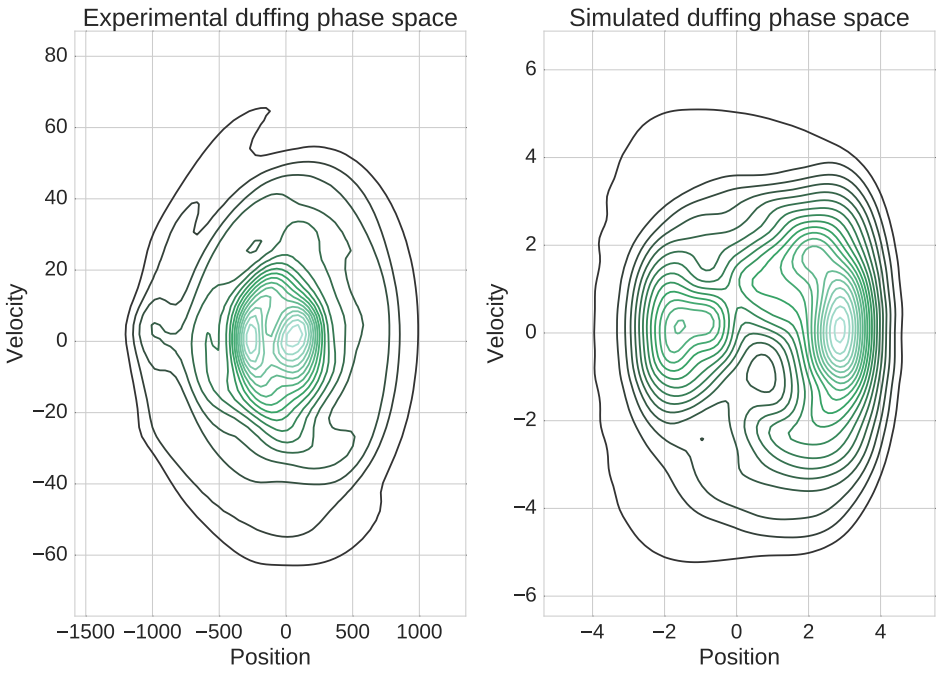

FIGURE 4.4: Experimentally generated double well system (left) and SDE simulation for the same (right). Both systems demonstrate the same multi peaked behaviour. The swirling behaviour in the simulated case is characteristic of many driven Duffing oscillator system and is a likely result of insufficient damping in the simulation. Complete matching is of course unlikely without feeding in the experimentally reconstructed triple well potential structure.

4.4 Potential reconstruction for an optical periodic potential

The potential experienced by the particle can be readily worked out by the methods previously mentioned in section 1.7.1. As mentioned before, computing the particles potential from the solution to its Langevin equation requires that the particle be in thermodynamic equilibrium. This might lead to the conclusion that computing the particles potential from $U = -\int F dx$ is always preferable. However, this method turns out to fail, or at least require substantially more data points given to it to compensate for the noise in the system for certain shapes of potential - namely periodic ones.

As before, for the Langevin method of computing the potential, we use the expression (with constraints of a steady state, thermodynamic equilibrium, non-time varying potential):

$$U(x) = -k_B T P_s(x) \tag{4.4}$$

where k_B is the Bolztmann constant, T the temperature of the system (usually taken to be 300K) and P_s is the positional distribution of the nanoparticle.

Applying this definition to experimental data obtained from a regular x^2 potential and a periodic multiple well potential from, we extract the structures in figure 4.5, obtaining single well for a non perturbed state in a regular Gaussian focus and a multiple well potential for a focus perturbed by the method described in section 4.3.3.1.

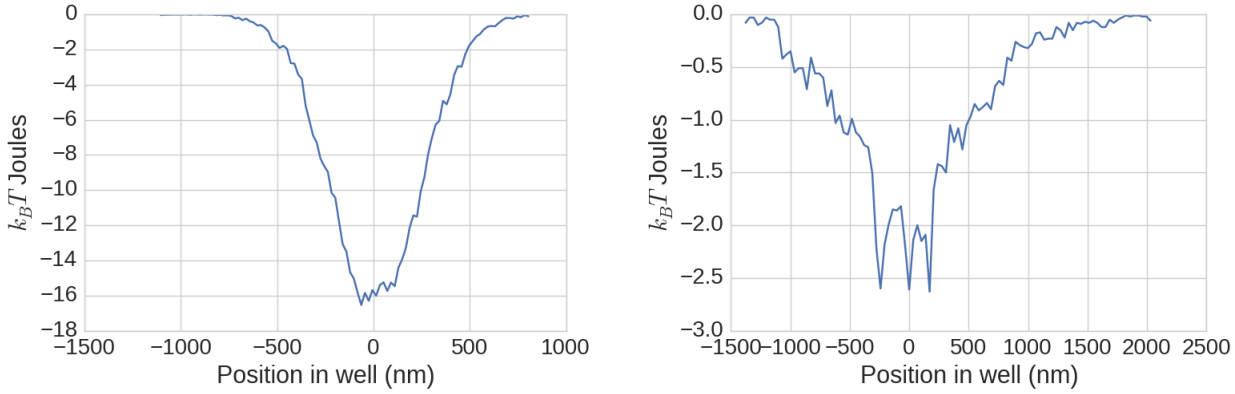

FIGURE 4.5: **Experimental data:** Potentials extracted for linear and periodic potential wells, using the steady state solution from the Langevenin equation to reconstruct the potentials.

We can then compare this to the result given by the kinematic potential, $U = -\int F dx$, in figure 4.5.

Naively one might expect to get the same result for the potential by these two methods, and for the linear case (with an unperturbed potential) this gives the correct result, figure 4.5, with some spread from the fluctuating noise field. In the case of non linear traps produced by applying an electric field (figure 1.7) or surface force (figure 1.7 2) the two methods also produce the same result. In the case of a periodic potential however, the functions produced by each method (kinematic and Langevin) look very different.

FIGURE 4.6: **Experimental data:** Acceleration position function for linear and non-linear potentials

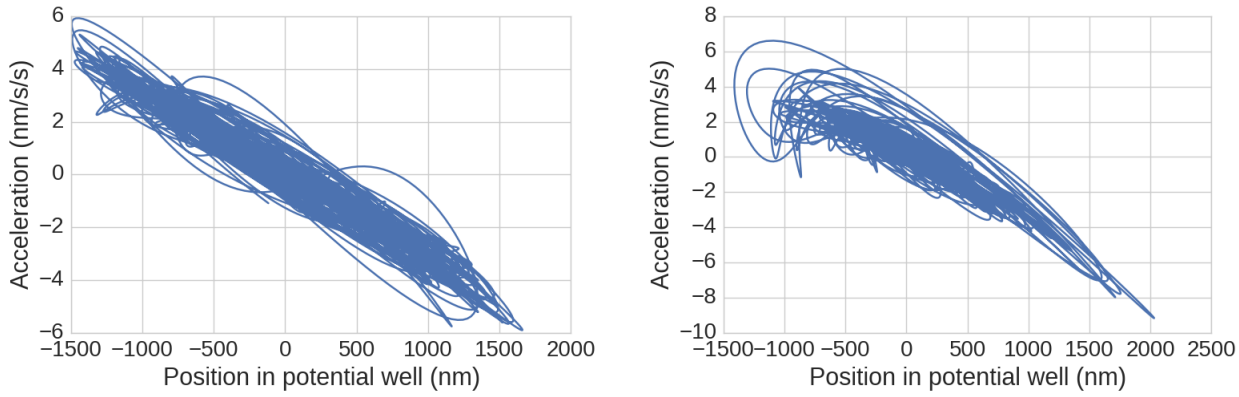

Possible reasons for this include the particle not being in a steady state or a bias in the direction of the stochastic fluctuating background field. It is very possible that different methods of reconstructing the potential function in different regimes of pressure. It is also possible that the spring function simply fails on symmetrical period shapes or that it requires the force originating from the potential to be significantly larger than the force from any random collisions with background gases. Furthermore it could also be that the component of the spring function that represents the periodic potential is simply washed out by noise.

4.5 Conclusion

While the choice between methods of reconstructing the potential remain to be validated to specific regime and appears to be inconsistent for periodic potentials (although only periodic potentials), having an a priori map of the particles potential allows us to calculate the instantaneous energy of the particle at any point during an oscillation, for an arbitrary shaped potential, as discussed in section 1.7.3.

Knowing this allows us to extract the energetic effect of the particles interacting with stochastic background fields, comprised of random gas collisions, and thermal fluctuations in the optics. A nonlinear system can, depending on the type of nonlinearity engineered, show a higher sensitivity after interactions with these effects, as demonstrated in section 5.0.4. This concept is expanded upon somewhat in chapter 5.

Due to the shift in systems response, different nonlinear potentials should provide different non linear amplification effects to different components of the background spectrum. Shifting or scanning through a range of bespoke potentials (like, for example the tunable Duffing nonlinearity demonstrated in section 6) could allow the background field to be scanned along its frequency and memory spectrum to a higher degree of accuracy than a linear system would allow

In principle, for a sufficiently non-linear system and long enough integration time this could let us distinguish the effects of different heat baths in our system, in a fashion similar to how the heating rate from Rayleigh scattering was extracted in [10], in which the limiting factor of the system was demonstrated to be Rayleigh scattering of photons from the test mass - in essence, the heatbath of the laser.

Chapter 5

Nonlinear system/term identification

In all the systems experimentally generated in this thesis, a common theme is the matching of a numerically simulated stochastic differential equation to the particle dynamics. While reconstruction of the potential is certainly possible for a state with no time domain driving. It is not always trivial, especially in the case where there are significant time domain operations being done on the particle, such as in the case of the bifurcation scan , section 6, or Fano resonance, section 3. Therefore, it would be helpful to make use of techniques common in the analysis of nonlinear systems to assist in the process.

Additional tools to understand and characterise the nonlinear states generated in the system are detailed. We then explore the types of nonlinearity available in the levitated nanoparticle system.

We also put nonlinear optomechanical systems into the context of force sensing, simulate the impact of a weak DC field on a levitated system with increasing nonlinear motional terms and suggest a an experimental demonstration of the same.

5.0.1 Attractors

An attractor is a set of values within a single basin of attraction towards which initial conditions with the basin of attraction evolve asymptotically towards. A strange attractor is one whose structure is fractal[124]. The dynamics of the motion within such an attractor are often chaotic, although this is not required. The relevance to our system is that the Duffing oscillator displays chaotic motion for certain driving values.

5.0.2 Poincare Sections

A Poincare section is a dimension reducing map that transforms an n dimensional space into an n-1 dimensional space by taking a slice or *section* through that phase space[125], a visual representation of this process is given in figure 5.1. For a 2d phase space of position x and momentum p a Poincare section can be a slice through x at a constant value of p or a slice though p at a constant value of x.

A Poincare plot or return map is a type of recurrence plot often used to quantify how self similar a process is and can be used to distinguish period, random and chaotic behaviour.

5.0.2.1 Poincare definition

To generate a Poincare plot, we take a time series:

$$x_t, x_{t+1}, x_{t+2}, x_{t+3}, x_{t+n} \tag{5.1}$$

and then sequentially plot the points (x_t, x_{t+1}), (x_{t+1}, x_{t+2}), (x_{t+2}, x_{t+3}) and so on. To analyze our system with this technique, we take the $v = 0$ (velocity $= 0$) slice of phase space as our Poincare section and then take the position of the particle as it passes through this Poincare section on successive orbits as our time series for our Poincare plot.

A completely periodic system will always return to the same point of a Poincare plot. A system undergoing a random walk in a biased symmetric potential should manifest as a circle.

5.0.3 Stability Analysis

For a Poincare section composed of the points:

$$S = (x_t, x_{t+1}), (x_{t+1}, x_{t+2}), (x_{t+2}, x_{t+3}) \tag{5.2}$$

we define the absolute distance R from the centre of the recurrence plot for each in the Poincare plane. As the stability of the original system is closely related to the stability of the Poincare section S. Therefore we construct the function:

FIGURE 5.1: Conceptual explanation of Poincare section. An orbit of phase space dimension n is reduced to (n-1) by taking an intersection surface through the phase space of the n dimensional system.

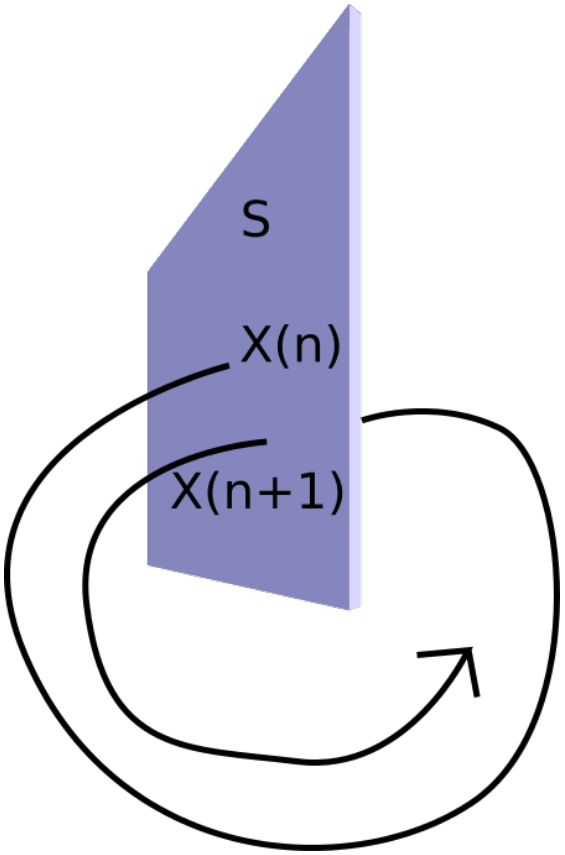

$$f(x) = \frac{\partial R}{\partial n} \tag{5.3}$$

in order to study the rate of change of the stability of the system.

It follows naturally that a perfectly recurrent, periodic and noiseless and linear system (A harmonic oscillator with no damping) would never change its distance metric for points on the Poincare section, while a very nonlinear system would rapidly change its stability metric.

Analyzing the stability of the system should allow us to identify the regions where the particles orbits moves from one basin of attraction to another. More importantly, it allows us to extract an additional quantifying metric for the system with which to compare against our simulations when attempting to match terms. In the case where two attractors cross the boundaries of each others basins of attraction a physical system may demonstrate intermittency, in which a system alternates between periodic and chaotic behaviour. These laminar phases of chaos should show a much greater sensitivity to initial conditions that the systems periodic states. Therefore we can look for changes

between topological phases of a nonlinear system by studying the rate of change of the distance metric of the Poincare section.

5.0.3.1 Poincare simulation - experiment comparison

We simulate a nanoparticle in a Duffing potential using the stochastic differential equation generalization of the Runge Kutta scheme [126], and comparing it to experimental data, figure J.1 in the Appendix and 5.2. We use the amount of Duffing nonlinearity and strength of the stochastic term as variables. We note that, in general, the addition of white/Gaussian noise causes expansion of the Poincare geometry, while the increase of the duffing term causes structural warping. Furthermore, the type of structure in the Poincare diagram is tied to the type of nonlinear term in the equation of motion. While, as shown in 4.4 it is possible to produce a similar phase space from two different potentials, the same is not true of producing very similar Poincare sections 5.2. To display the poincare section and stability analysis output on the same plot, we take every time the stability of the system goes over its mean value as a 'positive transition', and every time the stability of the system goes under its mean value as a 'negative transition'. Its important to note that while it appears to be possible to change the Duffing parameter and noise values such that the Poincare section appears *mostly* similar, it was not found to be possible to alter these values to make the spatial distribution of positive and negative transitions of the stability metric the same in the case of the experimental and simulated data. The take home of this fact being that this is an excellent figure of merit to distinguish one kind of nonlinear term from another kind.

Full extraction of the underlying potential (and thus identification of all the nonlinear terms) of the experimental system and possibly use of a non-Gaussian noise model would likely yield a much closer match of Poincare section and stability metric. Applying this analysis method to nonlinear systems generated in future would possibly allow the extraction of the underlying nonlinearity, or identification of its attractor.

FIGURE 5.2: Poincare Sections with areas of rapid change in the stability metric highlighted, note the spatial clustering of such regions. Stability metric (blue) and rate of change of stability metric (green). The key element of interest here is that the compression the Poincare section is different depending on the type of applied nonlinearity. It is therefore difficult to 'fake' for example the triple well (which has a nonlinear term more complex than a simple duffing parameter) by simply changing the duffing and damping parameters of the simulation. This is therefore a useful method of analysis when attempting the recreate the nonlinear terms present in experimental data by simulation, as it is possible to 'fool' oneself by just using a phase space analysis.

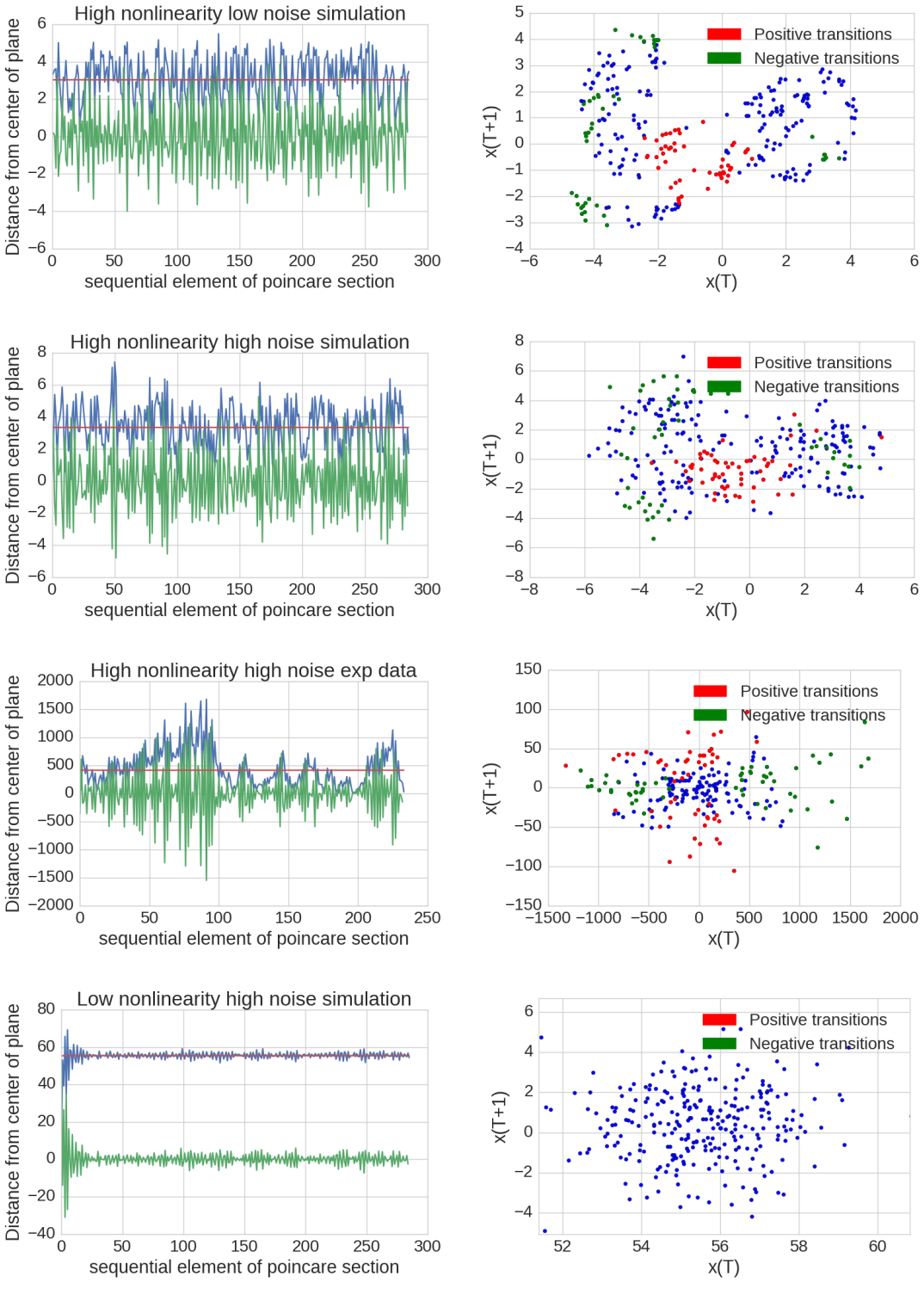

5.0.4 Enhanced sensitivity in non linear systems

In the cases of both spatially nonlinear potentials and time driven non linear states, the system exhibits critical points in which the particle is more sensitive to initial conditions than in a linear state, this principle is one of the founding requirements for chaotic motion. Correct harnessing of this regime of motion has been demonstrated both theoretically and experimentally in other systems to lead to an increase in frequency dependant sensitivity. Bespoke potential design for the design of chaotic motional states with the desired sensitivity to initial conditions and phase space folding for readout could lead to an interesting force sensing protocol as it would allow for some degree of frequency targeting in a similar manner to the stochastic resonance result achieved by [63], with a potential gain of an order of magnitude over a linear optomechanical system [127].

It should be noted however, that any increase in the susceptibility function for the oscillator in a given frequency band, will increase both the signal and the noise associated with that frequency band, leaving the ratio of the two unchanged. However, an important distinction here is that only the *mechanical* noise in the system will be amplified, ie the impact of random background fluctuations on the particle. As this scales with pressure and the electrical an optical noise floor is relatively high in our system, enhancing the detection sensitivity of the system with nonlinear potential remains viable for the near future. Figure 5.5 demonstrates this effect by showing the systems energetic response to the random background interactions the particle feels as it responds to collisions with gas particles.

The creating of nonlinear system with tunable nonlinearity driving parameter for the recovery of an otherwise hidden weak signal by an optomechanical test mass will form the basis of a future experiment.

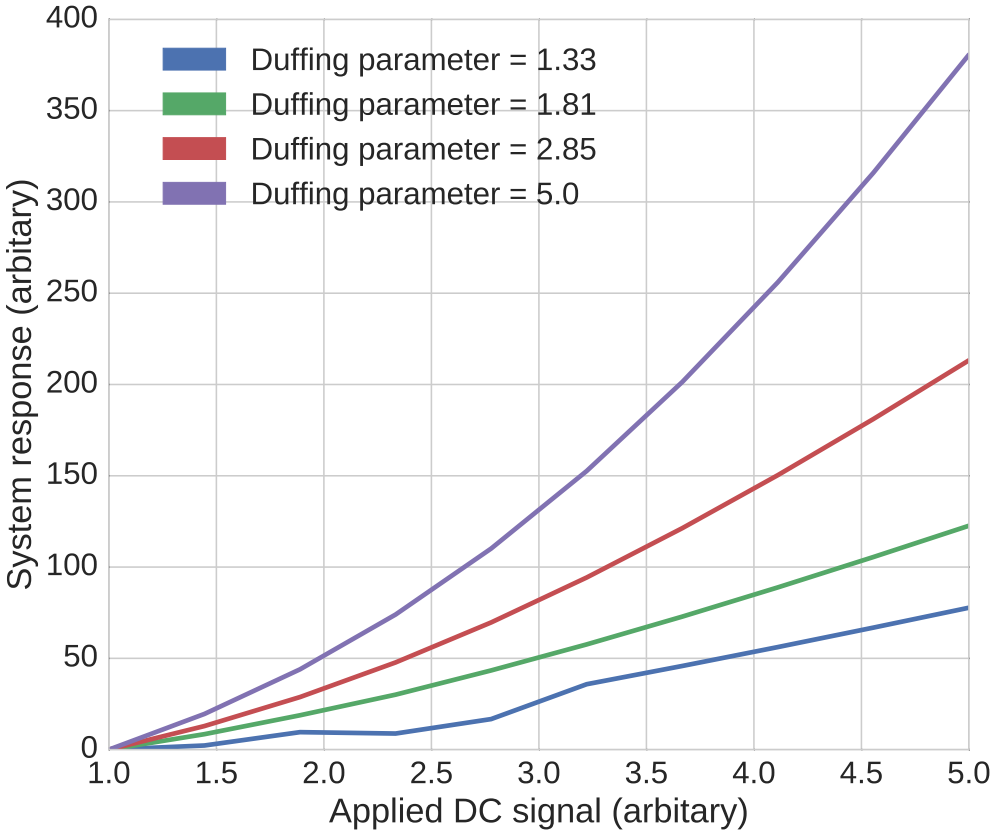

FIGURE 5.3: A simulated levitated nanoparticle with a controllable duffing nonlinearity (such as that we generate experimentally in section 6) response to DC fields of increasing strength. For the same positional resolution a system with a stronger nonlinear component shows a detectable response to a weaker DC field.

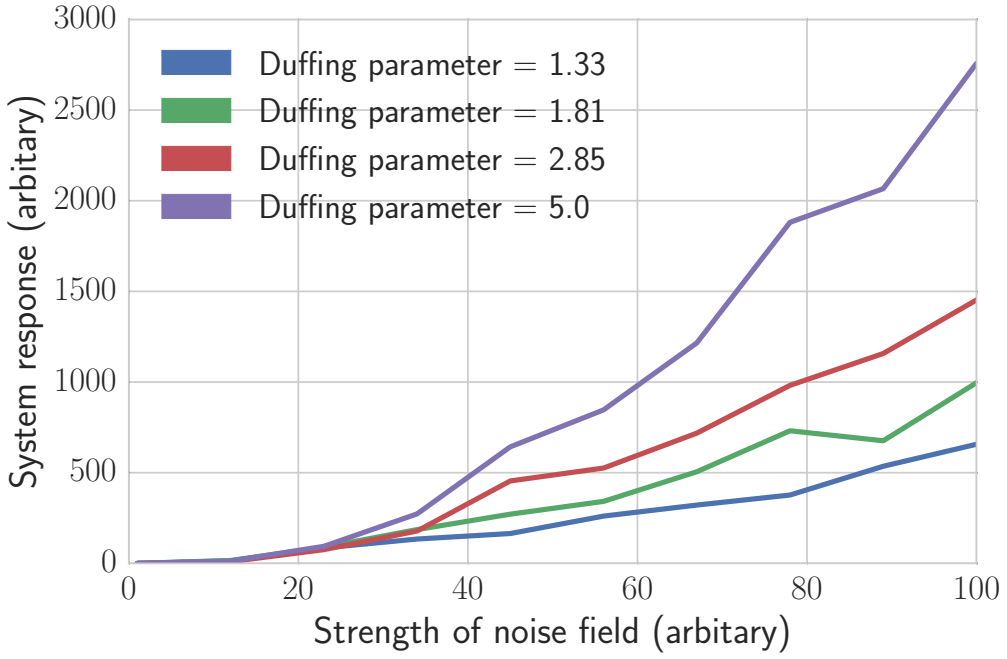

FIGURE 5.4: A simulated levitated nanoparticle with a controllable duffing nonlinearity (such as that we generate experimentally in section 6) response to randomly varying fields of increasing strength. For the same positional resolution a system with a stronger nonlinear component shows a detectable response to a weaker random field. As detection of weak random fields is unlikely to be valuable outside of the somewhat niche field of dark matter searches [5][6][7][8], the simulation is reproduced here purely for parity with the available experimental data available later in 6.10, and also in 5.5.

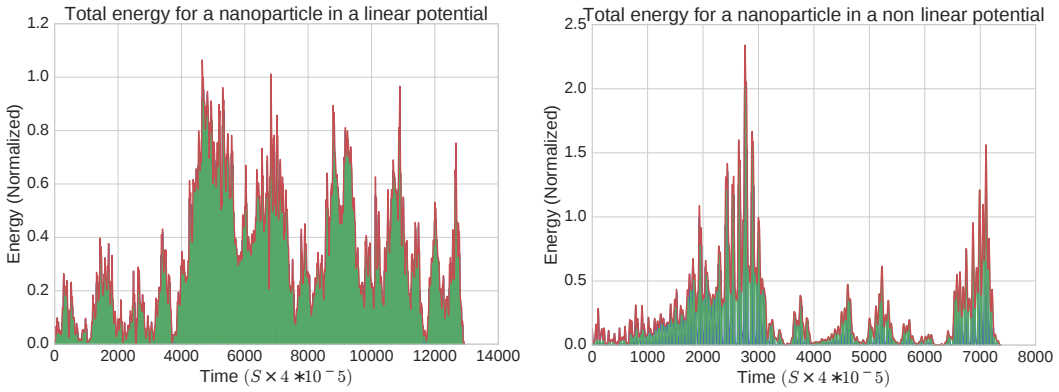

FIGURE 5.5: The same levitated nanoparticle trapped in a linear and a spatially defined nonlinear potential (the optical multiwell from 4.3.1) shows substantially increased sensitivity to the random background field of the gas particles in a specific frequency band denoted by the specific nonlinear terms that define the potential. Its important to note that simply increasing the susceptibility function of the oscillator amplifies all its noise sources along with any desired signals. However, of key importance is that this only amplifies *physical* noise sources that actually interact with the particle. Such a technique would therefore be useful for overcoming the *detector noise* when attempting to sense a weak field or signal, but not the *pressure noise*. This result is consistent with the simulation in 5.4.

5.1 Type of available nonlinearity

For any system with a nonlinear potential, different motional types exists for different driving parameters.

In the case of the spatial double well, the well separation gives the magnitude of the duffing parameter in the equation of motion. Bespoke optical gradients should give access to other types of nonlinearity, although not all chaotic attractors have physical solutions realizable within our system. Specific spatial parameters should also give access to chaotic behaviour.

In the case of an unperturbed Gaussian optical potential, for example, in the x or y degrees of freedom. The availble nonlinearities are somewhat limited 1.5.1, with only the linear, and Duffing terms showing up in the diagonal terms of spring constant matrix:

$$k_{xx} = -\frac{4\chi i_0}{cw_0^2\left(\frac{z^2}{z_R^2}+1\right)^2}e^{\frac{-2x^2-2y^2}{w_0^2\left(\frac{z^2}{z_R^2}+1\right)}} + \frac{16\chi i_0 x^2}{cw_0^4\left(\frac{z^2}{z_R^2}+1\right)^3}e^{\frac{-2x^2-2y^2}{w_0^2\left(\frac{z^2}{z_R^2}+1\right)}} \tag{5.4}$$

with the first term giving rise to the standard linear potential and the second term representing a Duffing nonlinearity. This matches well with the easy availability (and thus high incidence) of effective double well solutions created in the driving parameter phase scan, section 6. However, even a small spatial peturbation to a potential can give a great deal of unexpected nonlinear terms, for example in the case of the z degree of freedom, we find the following:

$$\begin{aligned}&\frac{8\chi i_0 z^2}{cz_R^4\left(\frac{z^2}{z_R^2}+1\right)^3}e^{\frac{-2x^2-2y^2}{w_0^2\left(\frac{z^2}{z_R^2}+1\right)}} - \frac{2\chi i_0}{cz_R^2\left(\frac{z^2}{z_R^2}+1\right)^2}e^{\frac{-2x^2-2y^2}{w_0^2\left(\frac{z^2}{z_R^2}+1\right)}} + \\ &\frac{16\chi i_0 z^2}{cw_0^2 z_R^4\left(\frac{z^2}{z_R^2}+1\right)^4}\left(-2x^2-2y^2\right)e^{\frac{-2x^2-2y^2}{w_0^2\left(\frac{z^2}{z_R^2}+1\right)}} - \frac{2\chi i_0 e^{\frac{-2x^2-2y^2}{w_0^2\left(\frac{z^2}{z_R^2}+1\right)}}}{cw_0^2 z_R^2\left(\frac{z^2}{z_R^2}+1\right)^3}\left(-2x^2-2y^2\right) + \\ &\frac{4\chi i_0 z^2\left(-2x^2-2y^2\right)^2}{cw_0^4 z_R^4\left(\frac{z^2}{z_R^2}+1\right)^5}e^{\frac{-2x^2-2y^2}{w_0^2\left(\frac{z^2}{z_R^2}+1\right)}}\end{aligned} \tag{5.5}$$

Whilst most of these terms are small in comparison to the linear and Duffing terms, it demonstrates that adding additional modes to the system is in principle quite easy.

Clearly, engineering an optical intensity profile with the desired non linear modes should be possible.

We can also drive the system into nonlinear states by perturbing the system in time with an additional driving frequency or phase, as with the spatial case, specific values of the driving parameter should give access to chaotic motion. It is not unreasonable that spatial and temporal non linearities will give access to different types of nonlinear states and chaotic attractors. These kind of nonlinear states would be interesting for our system due to the theoretical interest in using non linear light matter interactions to prepare non classical states of massive oscillators.

5.2 Chapter outlook

5.2.1 Symbolic regression

In short, identifying specific nonlinear terms is a non-trivial process, although the terms governing different parts of the dynamics are more readily separable under certain phase spaces or transforms than others.

Analyzing the Fano resonance data involved effectively guessing the form of the required coupling and potential structures required to see the effects, and then brute forcing the specific values of the coefficients to the equations therein.

Taking this one step further and brute forcing the terms governing the dynamics entirely turns out to be a fairly recently solved problem. Symbolic regression is a form of genetic programming by which terms representing a dynamical system are selected from a library, with a parsimony parameter (a favourable evolutionary weight on the number of terms in the genetically produced equation of motion) to prevent the equation of motion bloating into an overly long construct, this is the key difference that separates the technique from, for example, just fitting a high order degree polynomial to the reconstructed potential. While we might be tempted to associated unsupervised machine learning models with just generating a large matrix that merely mimics the output of the system rather than giving us any insight into the underlying dynamics, such a technique was recently applied to recover the governing equations from similar systems to those analyzed in this thesis. [128][129][130]. In intuitive terms, the differential equations of motion of the system are brute forced from relatively naive assumptions.

In principle, this technique could be highly useful for reconstructing the equations of motion, and therefore the shape of clusters of agglomerated nanoparticles. One example is given in figure 5.6, with more in appendix C. Cluster 5.6 is likely to be a mostly

spherical particle with some precessional or rotational cross terms and is therefore likely solvable with small or no perturbations to existing models, however the cluster in figure is highly nonlinear with no discernable cartesian degrees of freedom. For this kind of nano-object, automated model generation would likely be very helpful.

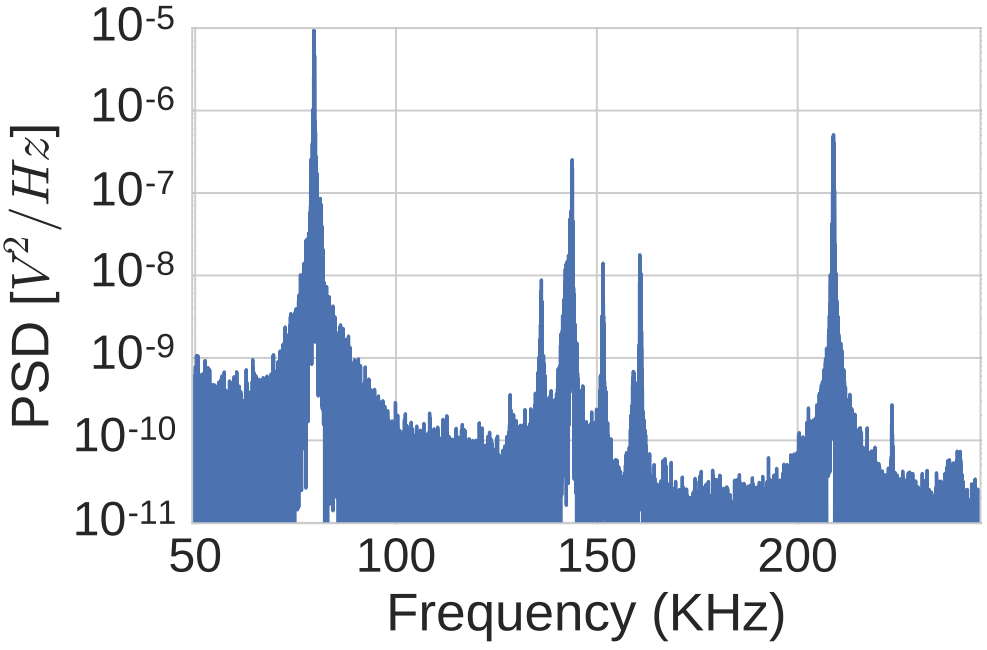

FIGURE 5.6: A mostly spherical cluster, in which 3 main Cartesian degrees of freedom are still visible, with additional nonlinear terms being generated around the x peak of the system.

Regardless of the shape, it should in principle be possible to break down the motional spectra of such objects into a system of coupled linear harmonic oscillators. While a cursory glance at section 3 tells us this is not always the best explanation behind the underlying physics (modelling the motional modes of the z degree of freedom in the case of the Fano resonance is not the most fundamental underlying physical model), it is a close approximation.

5.3 Summary

In summary we present a set of figures of merit by which the nonlinear elements of the experimental systems studied in this thesis can be compared, such as energy evolution, Poincare section and Poincare stability.

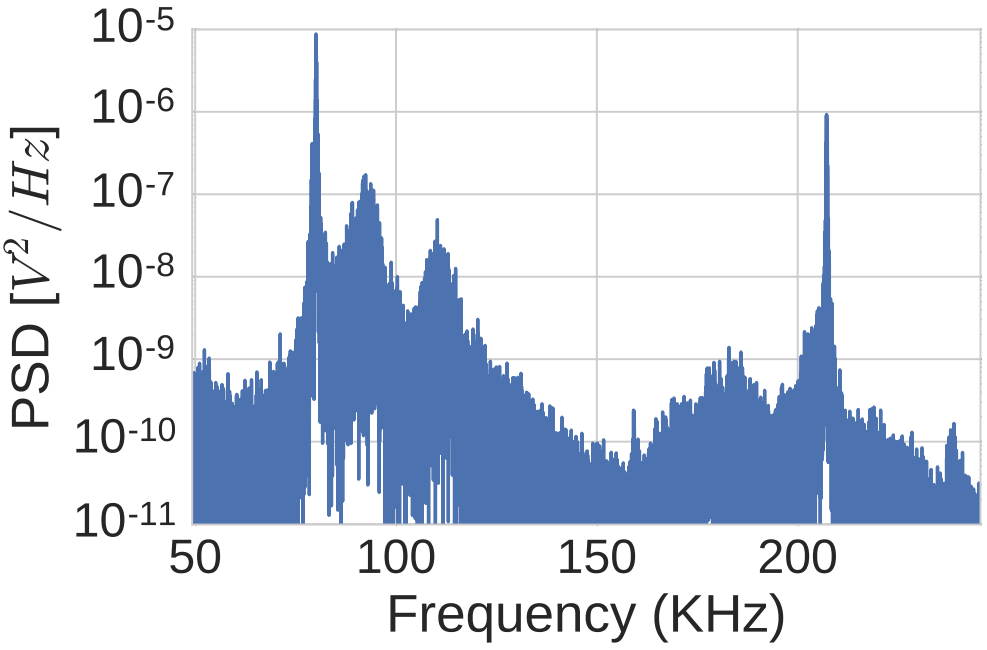

FIGURE 5.7: A highly non spherical cluster in which the normally found 3 main degrees of freedom are not visible and the motion is visibly highly nonlinear.

The key take aways from this chapter are firstly that the nonlinear motional terms that can be easily engineered in this system can be more sensitive than the linear terms to perturbations - a useful aspect for sensing applications. Secondly that by applying a Poincare section or by looking at the Poincare stability of the system the different types of nonlinear motional terms can be easily distinguished from one another, to a degree that is not possible from just analysising the phase space.

Chapter 6

Time domain parameter scan - bifurcation

6.1 Chapter overview

We systematically explore the systems available nonlinearities with temporal driving across a large parameter space. By varying the driving parameters systematically across an extremely wide range of possible inputs, we recover the cooling solutions for the spatial restricted phase spaces already reported on commonly in the literature [10], highly driven ring states, temporal driving effected double wells, as demonstrated in figure 6.9, which are themselves similar to those produced spatially earlier in the thesis, figure (4). Finally, initial experimental evidence of bounded chaotic motion is shown.

The nonlinearities generated are contrasted with current theoretical proposals within the optomechanics community to generate non classical states of resonator systems at high occupation numbers.

6.1.1 Mapping non linear response - bifurcation plots

Ideally, we could map the nonlinear states physically realizable in our system by varying the driving parameters systemically and looking at the stability of the output states.

This kind of analysis is often known as a bifurcation plot, it requires both systematic control of the input driving variables and collecting large amounts of data, which requires system stability over long timescales. These two requirements exclude this type of analysis for the spatially defined nonlinearities generated in section 4 as they tend to be less stable. As dynamically driving the particle into nonlinear motional states has a

high chance of causing particle loss, the following experiments are performed at relatively high pressure, 10^{-2} mbar. Driving experiments were attempted at 10^{-6}mbar, however the particle was typically lost as soon as the system reached a nonlinear mode.

6.1.1.1 Bifurcation plot example problem

As an example of how the technique works we can look at the bifurcation plot of a simple, well understood system. We choose one that transitions between linear, nonlinear bistable and chaotic behaviour. The logistic map, which is a polynomial recurrence relation of order 2, often used as an example of a simple system that displays all such behaviours. The recurrence relation for this system is defined as [131]:

$$x_{n+1} = r x_n (1 - x_n) \tag{6.1}$$

in which x_n represents a number between 0 and 1 and x_{n+1} represents the number on the next iteration, r is the driving parameter varied in the plot 6.1. The plot 6.1 shows the value of x_n that the system converges to over a long time period against the driving parameter r. Recovering the same structure that is commonly reported in the literature with our own computational tools is encouraging for applying a similar analysis to our own experimental data.

Note that certain values of the driving parameter r tend towards one stable solution, while other values tend towards multiple stable solutions and other values tend towards no stable solutions at all. The relevance of this example to our case is the transfer of the system from stable to chaotic solutions and back again as a function of the driving parameter. Computing a similar map of our system gives insight into the stable non linear solutions possible in our system, as well as categorizing the regions where the system acts chaotically, as both of these are of theoretical interest to the community[132].

6.1.1.2 Computation of limit cycles in an experimental system

In the case of the example problem, finding the the stable solution for is simple as we have the complete equation of motion and can simulate the system for all its initial conditions, furthermore the example system has no stochastic elements. Computing the limit amplitude for a simulated system is therefore comparatively easy.

Analytically we would define the steady state that the system tends to over time as a stable limit cycle. A limit cycle can be defined by the solution vector:

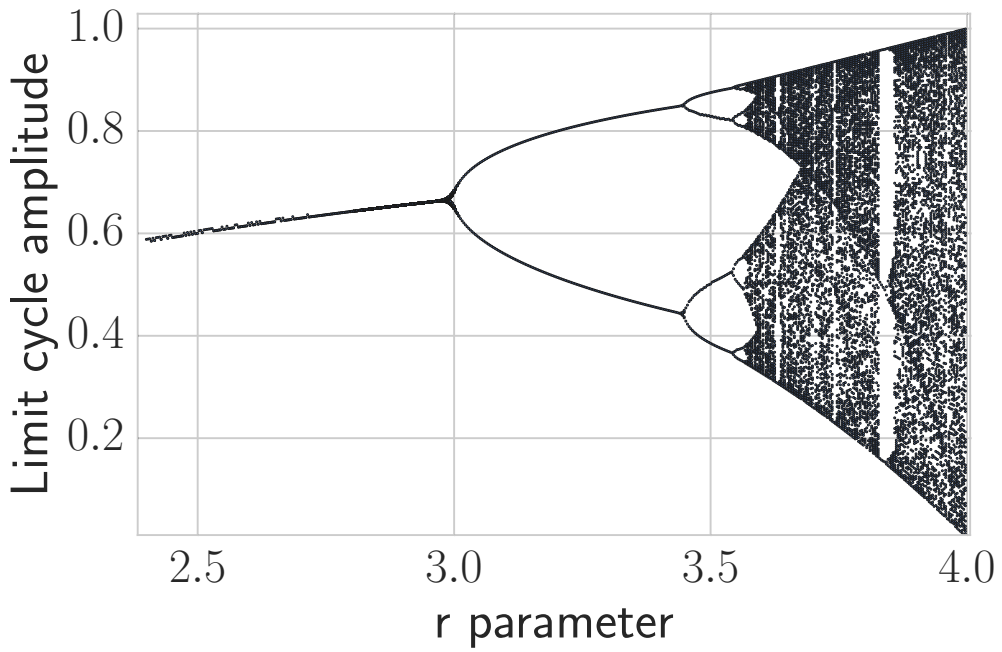

FIGURE 6.1: Bifurcation map for an example system, the logistic map: $x_{n+1} = rx_n(1 - x_n)$ in which r represents the driving parameter and x an arbitrary amplitude. This system demonstrates several behaviours characteristic of nonlinear systems, such as period doubling bifurcation (when the systems one convergent solution splits into two possible solutions depending on the initial conditions of the system), bi-stability and chaotic behaviour (the vertical line sections of the plot). Both r and the limit cycle amplitude are unitless. The full time traces for specific r values that give single, bistable and chaotic behaviour are given in appendix G to aid in the readers understanding.

$$X(t) = (x(t), y(t)) \tag{6.2}$$

such that:

$$x(t + T) = x(t) \tag{6.3}$$

$$y(t + T) = y(t) \tag{6.4}$$

In other words a curve that is recurrent in some plane.

A stable limit cycle is a curve that fits the above conditions and orbits on either side of it in phase space drift towards it. An unstable limit cycle repels nearby curves and a semi stable limit cycle exhibits both behaviours. Example in figure 6.2.

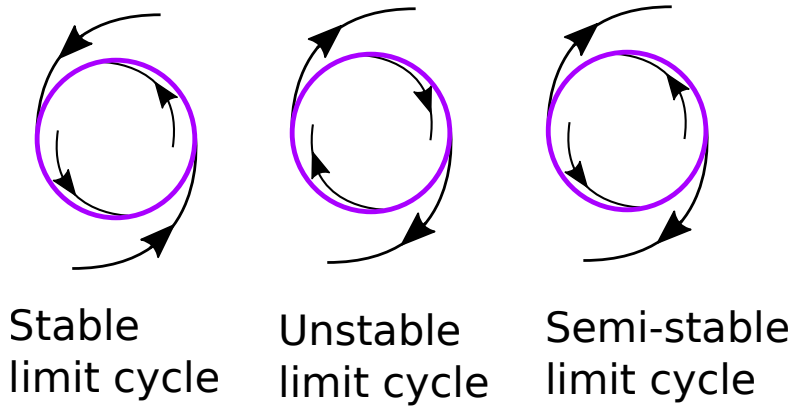

FIGURE 6.2: Example of stable, semi stable and unstable limit cycles (black), with the behaviours of nearby trajectories shown in blue. In the stable and unstable cases nearby trajectories flow towards and away from the orbit associated with the attractor respectively, in the semi-stable case both behaviours are displayed.

In the ideal case our system can be treated as a 3 decoupled harmonic oscillators in a white noise bath, experimentally, this is often not the case. The experimental system contains unknown coupling between the degrees of freedom, a non symmetrical particle and optical non linearities.

Computing the limit cycle behaviour in an experimental dataset requires a compromise of definitions. Pragmatically, we have to compute the 'steady' states of the system, which will likely include critical points as well as limit cycles.

The intuitive consequence of this definition mapped onto our system, is that a thermalised linear particle in the driven damped oscillator regime trapped in a harmonic potential would have one semi stable limit cycle (defined as we have defined it) and that a particle trapped in the double well scheme visualized in figure 4.1 would have two semi stable limit cycles (one for each potential well) that the system oscillates between. Therefore we compute the limit cycles in our system by looking for peaks in the positional histogram for a time series. The same method is used to compute both the example problem in figure 6.1 as well as the experimental data from the nanoparticle in section 6.1.2. On the premise that we recover the same result for the example problem as is given in the literature, it should be that this is a good method with which to analyze the experimental data from the nanoparticle as well.

The key point here is that exactly the same method of analysis is used in this chapter to generate the bifurcation maps, for both the example problem of the logistic map and for our experimental data. As the correct result for the already known and well studied problem (the logistic map - figure 6.1), we can assign at least some minimal trust to the result given to us by applying the same method to our data.

6.1.2 Experimentally produced bifurcation plots for a levitated mesosphere

6.1.2.1 Temporal driving specifics

Controlling the drive parameter of the system in the spatial nonlinearity case requires stable control of the system for a wide range of well separations and structures. While this may be possible with either the intrinsic lens geometry perturbations in section 4.1 or a spatial light modulator, it is not currently experimentally available.

Scanning across a driving parameter in the time domain however is experimentally simple, especially at pressures that damp the particles motion significantly while still being under those of the drift diffusion regime. Heavy damping in this case grants us an element of robustness in exploring the particles more non linear modes. Conducting a driving scan at lower pressures causes particle loss very easily, and recovering from non linear modes is experimentally very hard.

In this case we choose the driving parameter to be phase, noting that all the terms in the expansion of the Gaussian potential have the same scaling with laser power (section 5.1) it is likely to be an uninteresting parameters to vary. We then systematically study the particles motion while scanning across it. Locking an optical parametric feedback loop to the principle z motional peak of the particle as described in Appendix F.1 allows the driving phase associated with the drive on principle z motional frequency peak to be varied computationally. Applying the definition of a limit cycle to the data obtained by phase varying operation obtains an experimental bifurcation plot for our system, given in figure 6.3.

6.2 Bifurcation scan - experimental results

The limit cycle amplitude of the system as a function of the phase on the parametric drive is given in figure 6.3. At 0 phase the particle exhibits cooling behaviour consistent with experimental results thus far in the field (one limit cycle, small phase space), as the driving phase is increased, the system is driven to higher and higher amplitudes until it takes on full duffing behaviour.

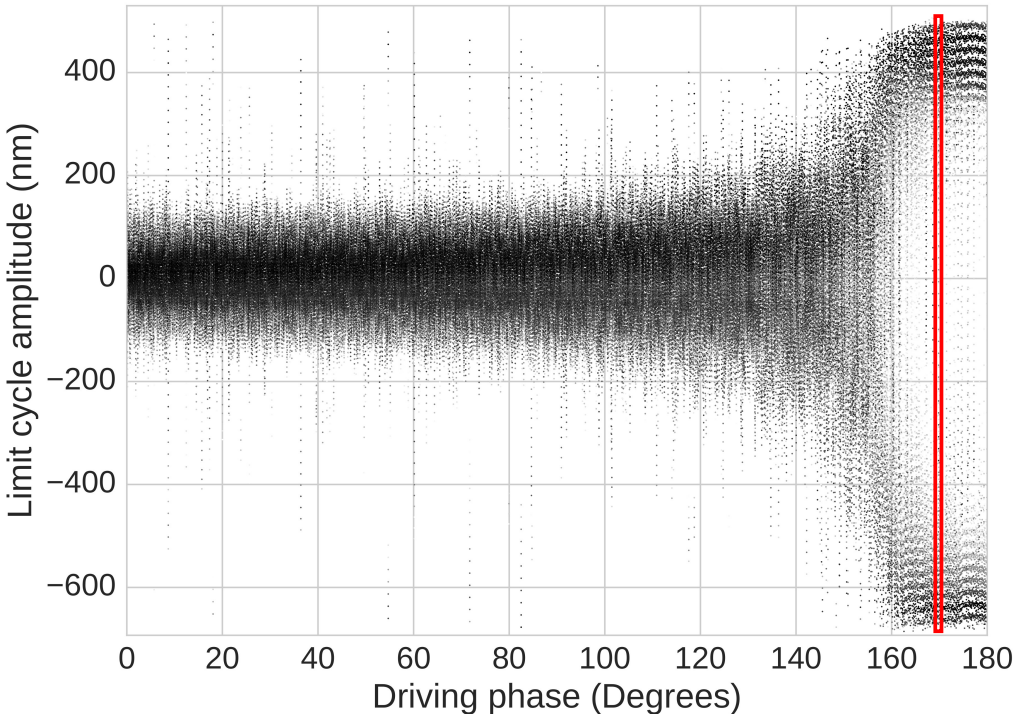

FIGURE 6.3: Bifurcation plot for complete phase scan of the system. The system visible transitions from having one central motional mode at one end of the phase spectrum, with extreme duffing behaviour (with two main motional modes) observed at the right hand end. The central region of the phase scan demonstrates many interesting 3 level systems such as van der pol oscillators and intervals of chaotic behaviour. The section marked by the red box is the dataset shown in figure 6.5. The size of the dataset makes the region difficult to see without zooming in as such.

6.2.1 Effect of critical value changes to motion - period doubling bifurcations

Scanning across different values of the driving parameter, it is easy to see the system transition between different motional types when the driving parameter crosses a critical value [132]. A change in driving phase for example causing a period double bifurcation, with the timetrace given in figure 6.4. This occurs in the 'fork' of the bifurcation plot of figure 6.3.

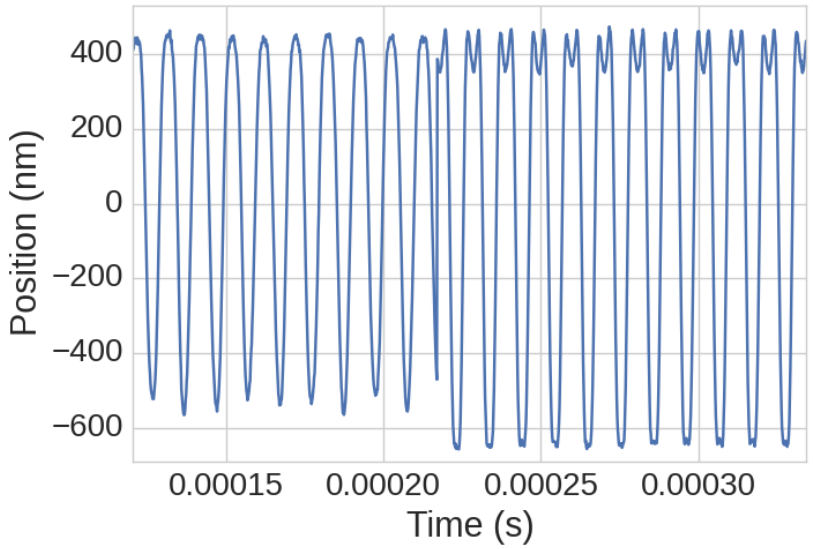

FIGURE 6.4: Period doubling bifurcation occurs to the motion of the nanoparticle upon a change in driving phase.

6.2.2 Chaotic motion

The main purpose of the bifurcation plot is to identify the critical points in parameter variation that allow the system to transition between different behaviours. It also provides a high level overview of the main non linear modes in the system, identifying the driving conditions for linear, nonlinear and possibly chaotic behaviour. The latter of which there is some community interest in generating in optomechanical systems[132].

Simple requirements for the generation of chaotic motion could be the following: 1) A nonlinear potential and 2) A pair of arbitrary driving parameters [133]. Therefore to create chaotic motion all we have to do is to generate a nonlinear potential with sufficiently low noise and find the correct driving parameters. Chaos is shown in literature to be theoretically possible in an optomechanical system in [132] by varying driving phase and power. In our case we only vary on driving parameter due to experimental constraints.

As the dataset is large, zooming into specific parameter sections of the bifurcation plot yields interesting information about the motional modes of the system. Figure 6.5 demonstrates transitional behaviour between the bimodal limit cycle behaviour characteristic of a duffing oscillator and the vertical limit cycle amplitudes often characteristic of chaotic motion. Several vertical line segments characteristic of this are displayed throughout the bifurcation scan, however the ones vertically interrupting the otherwise separated horizontal lines on the right hand side of the graph are the most stark. The

separated horizontal lines are indicated of Duffing behaviour, while the vertical lines interrupting such a structure are where the system is behaving chaotically.

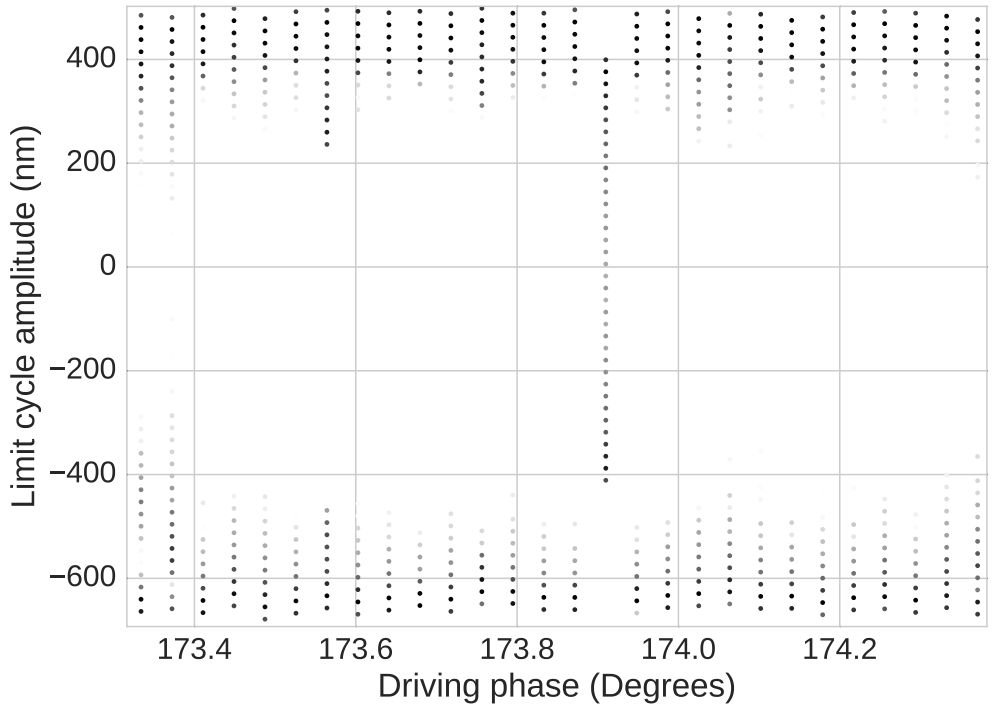

FIGURE 6.5: Data shown is the expanded version of the data in the red box shown in figure 6.3. The size of the dataset makes the regions of chaotic motion difficult to see without zooming in as such. Transitional behaviour between bimodal duffing oscillator and chaotic behaviour (vertical line sections) for limited values of driving phase.

As well as duffing like systems, the particle displays 3 level, van der pol oscillator like behaviour, with only part of the particles motion transitioning between deterministic and chaotic behaviour, as displayed in figure 6.6. The vertical structures in the limit cycle amplitude indicate chaotic motion, the oscillator is exhibiting strong response to initial conditions. The chaotic element of the motion is mostly bound to one side of the potential.

The phase space plot of the particles motion in one of the sections of chaotic motion is given in figure 6.7. With the FFT of said motion being given in figure 6.8.

In experimental systems it is often a significant challenge to separate the effects of random noise from the effects of chaotic motion. In many of the highly complex and noisy system we expect to occur in the natural world, simple measures such as a the Lyapunov exponent are often no longer sufficient for the analysis of chaotic motion [134]. This sensitivity of the Lyapunov exponent to noise is explored in appendix G.1, in which it is shown that it is positive to falsify a positive Lyapunov exponent by adding noise to the system, thus making it a poor discriminative tool in this case. Statistical

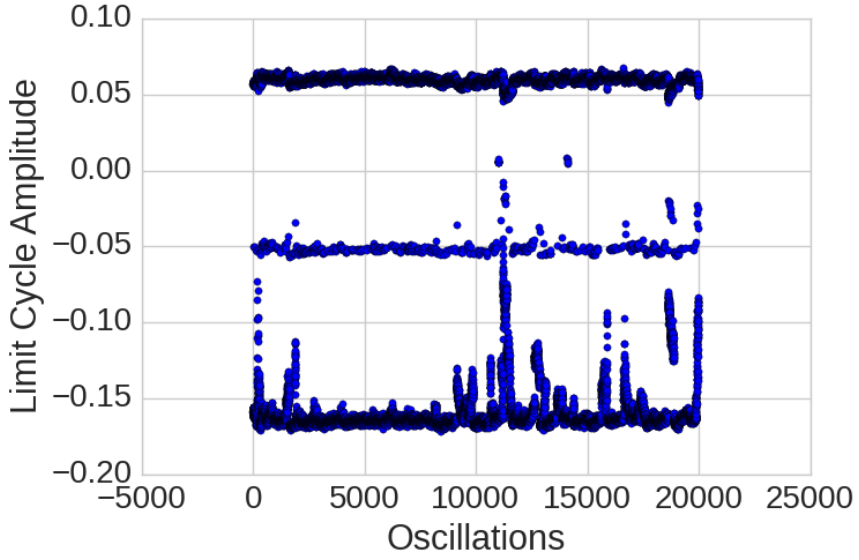

FIGURE 6.6: 3 level behaviour, only the lower two sections display the vertical population of states consistent with the switch to chaotic like motion.

tests such as recurrent quantification analysis (RQA) often provide insights into such systems, with geometric analysis of the substructures generated in the recurrence plot of chaotic systems providing analytic measures of the density and dynamics of chaotic states present in a system [135]. RQA turns out not to be a terribly useful method of analysis for our system specially other than telling us nonlinear potentials tend to be more chaotic, however an analysis of the double well system from section 4.3.1 is produced in Appendix H for completeness.

To be clear, we can not state with certainty that chaotic behaviour is recovered from existing results, only that similar structures appear in the bifurcation plot of the experimental system - which is itself generated by the same method (and indeed, the same python code) that detects chaotic behaviour when applied to the example problem.

6.2.3 Parameter scans as a possible library of state generation tools

As well as looking at the system in terms on limit cycle behaviour, we can analyze the system in terms of phase space for specific values of driving phase that appear to be interesting from the output of the bifurcation scan. It is for example of interest to a number of groups in the optomechanics community at present to study the transitional behaviour between multi level systems. Looking at the system in terms of its bifurcation allows for easy identification and characterization of double well systems by their well separation. An example of a highly separated double well system with a controllable

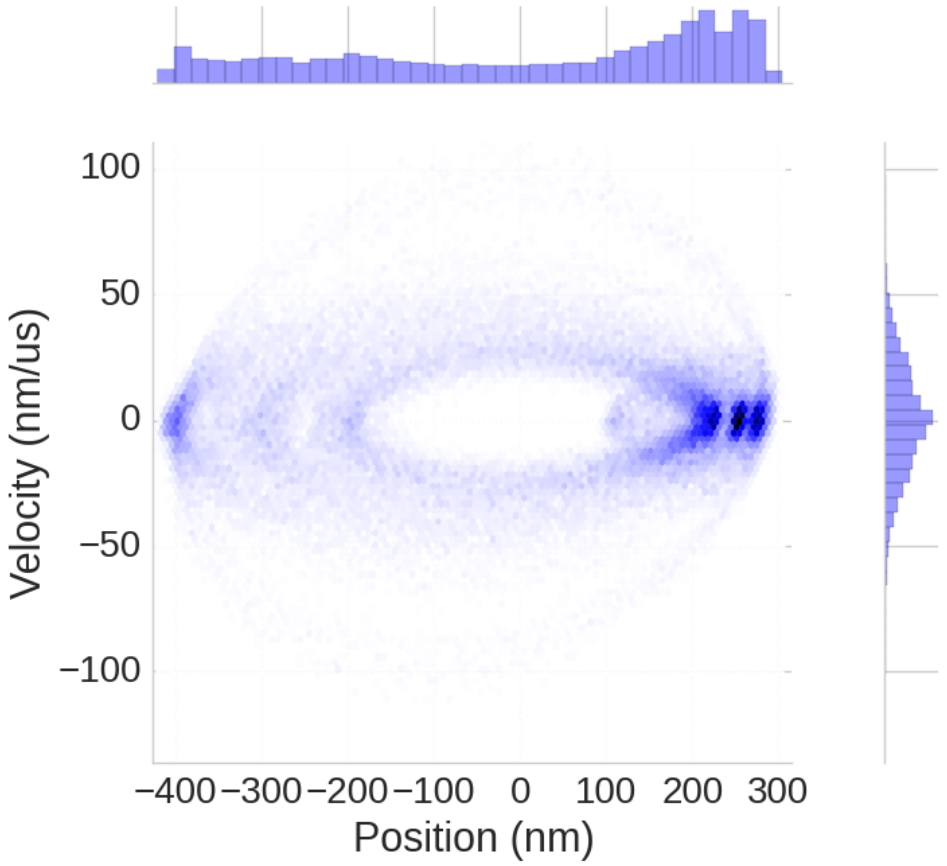

FIGURE 6.7: Phase space from the vertical structure region of figure 6.6. This verticality in the bifurcation plot is sometimes indicative of chaotic motion in other systems. Particle rapidly transitions between several effective potential wells.

separation given in figure 6.9, in this case we can choose the separation of the well by carefully selecting the value of the driving phase, using the results of the bifurcation plot/scan as a guide. While still strictly classical, these highly separated well systems provide an obvious classical analogue to a superposition state and may provide part of a tool kit of future state preparation, as other double well systems have been predicted too[93].

It is unlikely that any one guessed nonlinear operation or driving will provide a route to non-classical state preparation and it is also highly probable that many of the operations requested by the theoretical community for the ideal exotic state preparation scheme will not be available in the experimental system. Building a dictionary of available nonlinear behaviours may provide a route to a 'closest answer' scheme of marrying theory to experiment for exotic state generation.

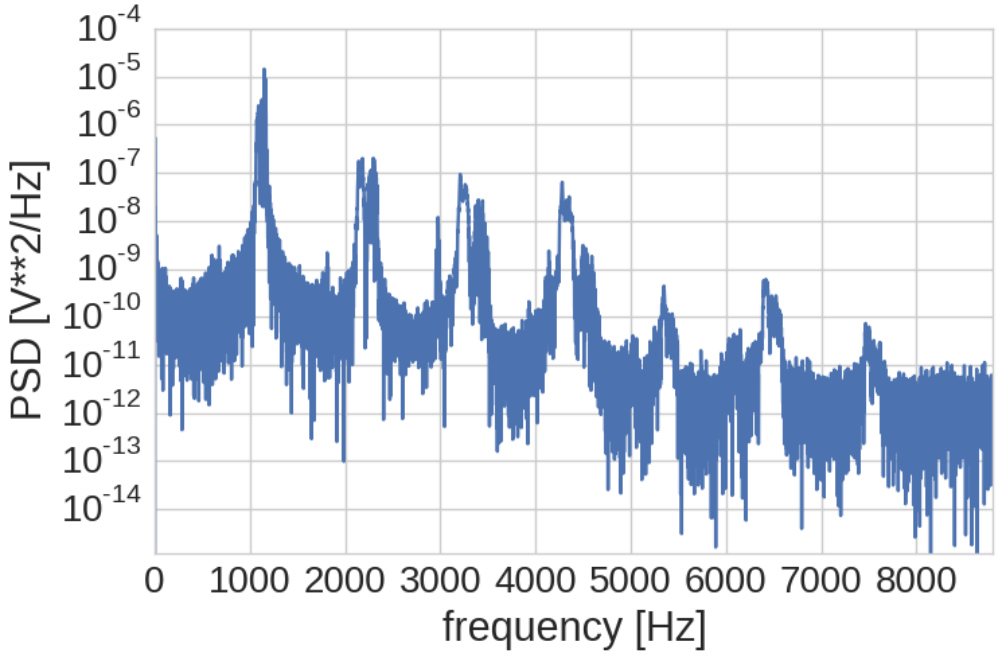

FIGURE 6.8: Chaotic motion from the vertical structure region of figure 6.6 in the frequency domain. From the number of visible peaks and cross terms, we could make the assumption that the particle is accessing a great number of the 'springs' and cross terms available in the higher order expansions of the Gaussian potential, as discussed in section 3.

In any case, the characterization of as many nonlinear states of the system by larger scale data collection methods than previously attempted in mesoscopic levitated optomechanics will be inherently useful in providing a toolkit for pragmatic theoretical approaches to non classical state generation, and possibly for future sensing applications, given the additional sensitivity to system perturbations made available by specific nonlinearities, and the inherent tunability of levitated systems systems.

6.2.3.1 Sensitivity of generated controllable nonlinearities

As discussed in section 5.0.4, a nonlinear system can in principle show a greater response from the same input than a linear one, provided both the nonlinearity and input are chosen carefully.

Sadly, we suffer from a parsimony of experimental data, and have only the random background field to calibrate the sensitivity of the system against. However, we still find that the system exhibits a greater response from the fluctuating background field, as an increasing function of the well separation. The fluctuating temperature of the system over time of the wells in figure 6.9 are shown in figure 6.10.

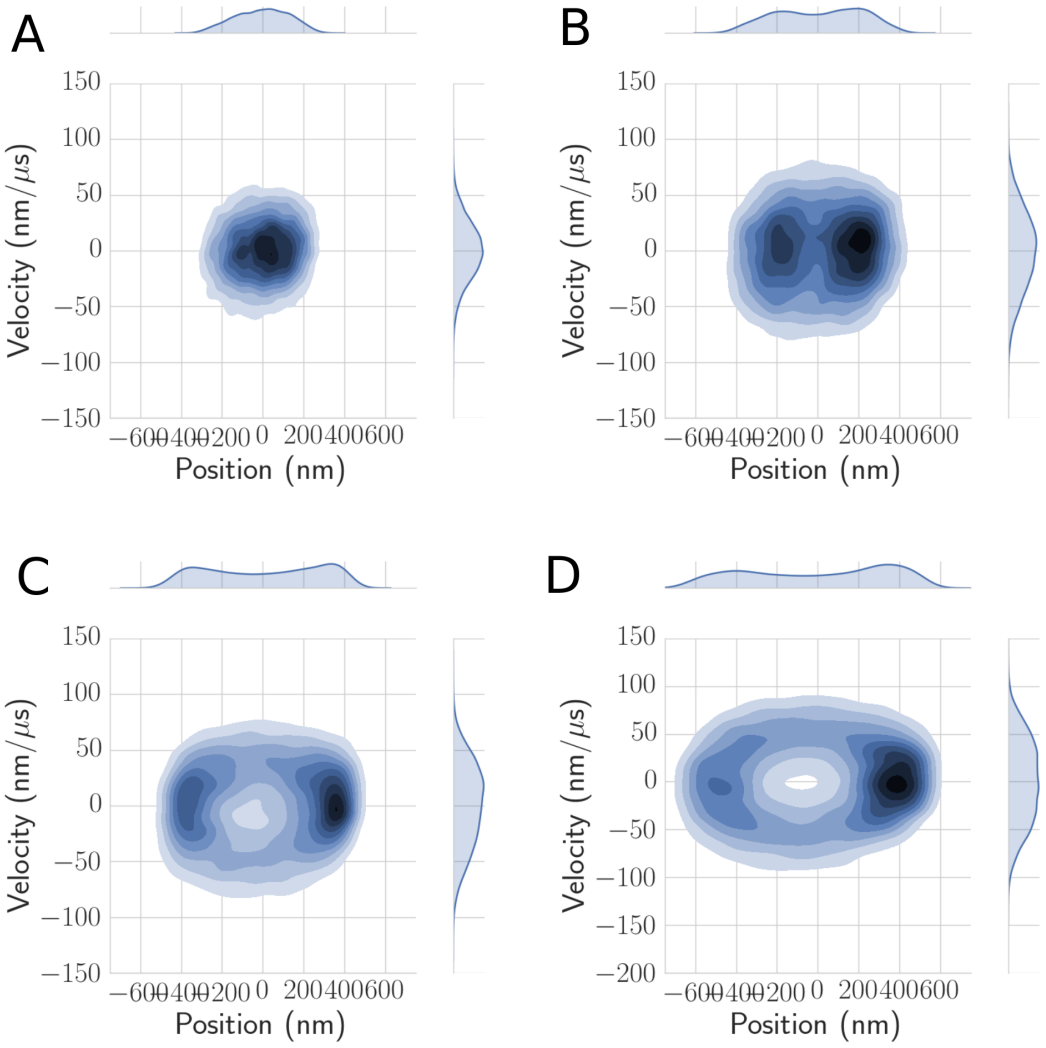

FIGURE 6.9: Double well system of variable separation, obtained by driving system at twice its z motional frequency at different phases. The sensitivity of the systems A-B-C-D is explored in figure 6.10. Note that it is the same nanoparticle in each case and only the drive is varied.

6.3 Chapter conclusion

It might be interesting to perform a two parameter phase scan to recreate a similar result to figure 4 of [132], varying the laser intensity not likely to result in rich chaotic dynamics for the scaling reasons mentioned above, but the frequency of the parametric drive might make an exciting second parameter. Indeed, the difference between the drive used to generate the Duffing terms in this chapter and drive used to generate the Fano resonances in 3 is the Fano resonances are created by driving at the frequency of the primary Z peak of motion, whereas in the case of generating the duffing nonlinearities and thereby the double well (6.9) we drive the system at twice the frequency of the z peak. From this fact alone we can probably make the statement that frequency might be

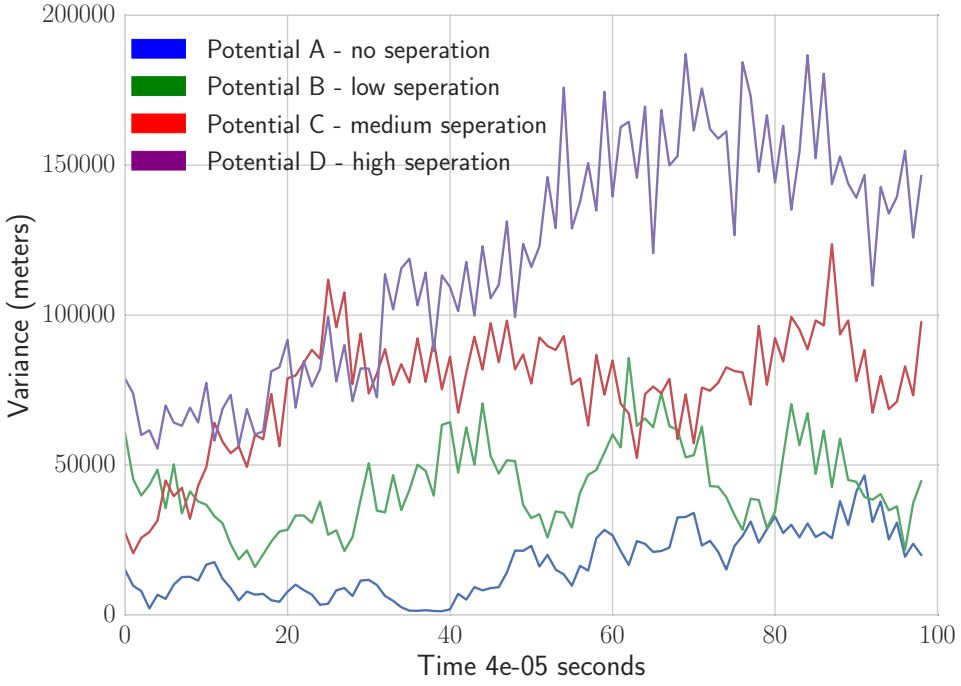

FIGURE 6.10: Fluctuations in particle temperature over time, as a function of well separations. As expected the double well of greatest separation from figure 6.9 fluctuates the most. The sum of the variances for each well is 17224, 44332, 77236 and 121195 respectively, in order of increasing well separation. This is a strong indication that the system's mechanical susceptibility to the random field is increased due to the increased relative strength of the x^3 term in the equation of motion (in comparison to the linear x^2 term). This result is consistent with the simulation in 5.4.

an interesting second parameter to systematically vary in order to find interesting new motional states of the particle. While this might initially read as a naive suggestion, the methodology of simply systematically varying inputs to the particle is how the Fano resonances demonstrated in section 3 were discovered.

On the subject of nonlinearity enhances sensing, since enhanced sensitivity to an AC (resonant) field has already been demonstrated by a stochastic resonance experiment [136], there is little point in retreading such ground specifically. To the best of the author's knowledge however, no experiment exists yet for enhanced nonlinear sensing of a DC field using a levitated nanoparticle, so this might make a good experimental direction for the future. Furthermore, sensing using a system both nonlinearity and low noise enough to be considered genuinely chaotic has some theoretically proposed merit [137][138] and has yet to be demonstrated for a levitated nanoparticle.

A more interesting direction still would be the generation of genuinely bespoke nonlinearities to match the desired signal, or the exploration of nonlinear terms more creative than

those offered by just driving the system into its duffing states. For example, combining spatially enabled non linear states such as those in sections 4.3.1 or 2 with time domain driving, or use of multiple feedback loops possibly without sinusoidal type modulations, it is a wide parameter space to explore.

It might also be interesting to perform similar bifurcation scans of non spherical nanoparticles, or the clusters discussed earlier (in section C). Perturbing a system of already coupled nonlinear oscillators is likely to yield a highly nonlinear response function, although likely at the cost of stability.

Chapter 7

Conclusions

7.1 This work in context

The first two major chapters of this work (Surface interactions and Fano resonances) represent novel work for the field at either their time of publication or at the time this document was written. At the time of uploading to the preprint server, the surface experiment was the first reporting of such an interaction with a nanoparticle within the field. The Fano resonance results will form the basis of a publication in the near future. The result of the particle jumping between potential wells (Chapter 3) was sadly beaten to publication by another group, as was the result of using time driving driving operations enhancing the duffing sensitivity of the system for force sensing (Chapter 5).

7.2 Scientific output - breakdown:

In summation, we perform a first principles analysis of the particles potential from the assumption of Gaussian optics. The particle's motion/evolution in said potential is analyzed/computed in terms of both stochastic differential equations and langevin equations. The assumption of white noise/memoryless heatbath respectively is tested and found to be in good agreement. Equivalency of the two methods of computing the potential under the assumption of the particle being in thermal equilibrium with its background leads to a novel method of computing the nanoparticles mass, which is, in principle, independent of the choice of voltage-meters conversion factor.

Based on this physical understanding of how the particle's motion evolves in its potential, a number of experiments are presented in which the systems nonlinear motional components play a key role: A probe for the Coulomb force in the case of the surface

experiment, a coupling mechanism in the case of the Fano resonances, and the source of the duffing term in the case of the bifurcation scan. The output of these individual experiments is detailed further below.

7.2.1 Surface interactions

We characterise the distance between a levitated nanoparticle and an inert uncharged silicon surface in the character distance length of 10's of microns by a first principles analysis of the particles motion in a harmonic trap in comparison to the expected form of the surface field. At time of publication, this was the first demonstration of such an effect in a levitated nanoparticle system.

Based on our results, we project observing Casimir-Polder forces in the same geometry to be an experimentally reasonable proposition, if the size of the trapped particle is raised and the charge on the nanoparticle is rendered small. Experimentally these two goals could be achieved by cutting the center out of the beam profile to reduce the scattering component on the particle (which scales more strongly with the radius of the particle than the scattering force) and simply testing the particle charge before undergoing the surface experiment respectively.

To observe genuine Casimir forces in the system is an exciting proposition, especially given free rotation of an-isotropic nanoparticles has been recent observed in the same geometry. Combining these two motional effects is predicted to give rise to exotic physics, such as repulsive Casimir forces.

In terms of extending the present surface interactions stream of work into the future, the weakest component of the surface results to date is the treatment of the optical force components in the system. This should be removable as a constraint with more analysis of the existing dataset by comparing physical effects between the x, y and degrees of freedom, and better modelling of the systems optics.

Extraction of 2d images from existing surface data is an ongoing challenge. In principle using the nanoparticle to image an arbitrary surface potential is a straightforward task, however without an image of a known structure such as an AFM calibration chip its difficult to know if we are making real images or just amplifying noise. Therefore, scanning a known regular structure is a matter of some priority in order to extract 2d images from the surface experiment.

However, to date, experiments aimed at extracting images from a regular calibration grid have been indeterminate due to the lack of experimental data against a known calibration

structure. Extremely careful design of any future nanoparticle AFM experiments will be required for future 2d calibration samples.

7.2.2 Fano resonances

We have extended our first principles analysis of the particle optical potential to model the higher order motional modes and intrinsic optical couplings between the degrees of freedom of the system.

By driving the system with carefully chosen parameters, additional motional modes can be generated and the couplings between these additional and primary motional modes can chosen such that some components of the system fall into antiresonance with each other. Such anti resonances are generated by both driving the system optically such that the Gaussian enabled couplings become significant in comparison to the base motional modes of the system, as well as couplings the degrees of the system linearly with an externally applied electrical field.

We demonstrate control over such anti resonances by reversing their window direction, by reversing the polarity in the case of the electrical field coupling, and reversing the systems equilibrium in the case of the optical driving. This (at the time of writing) the first demonstration of controllable anti resonance phenomena in a levitated nanoparticle system, which is exciting in and of itself.

Furthermore, if these additional nonlinear resonances can really be treated as semi independent frequency modes then there is a natural argument in using them for enhanced cooling on their own without any of the antiresonant effects between them being relevant. Recalling the relation $E = n\hbar\Omega$ between the average energy level and the frequency of the oscillator, a simple picture emerges that a higher frequency oscillator is easier to cool towards ground state (Under the assumption of cooling schemes being equally efficient as a functions of frequency, which is not always true). Despite this energy level scaling, work by Novotny et al [10] suggests power dependant minimum occupation number limitations derived from probabilistic Rayleigh scattering effects. Therefor it is of natural favour to generate higher frequency peaks for the same applied optical power incident on the nanoparticle. If we can accidentally give ourselves a factor of 3 by generating additional frequency modes, then trying for higher harmonics with bespoke trapping shapes or driving schemes seems both reasonable and desirable. Driving the system to, for example the 10th harmonic, would likely already be sufficient to reach the particles quantum mechanical groundstate with existing cooling power.

A natural task is to explore how many extra harmonics we can generate through driving, or by engineering of bespoke potential nonlinearities. The major constraint on generating these additional nonlinear modes is that the trap is sufficiently nonlinear enough to generate a large number of additional harmonics, while remaining overall energetically conservative with respect to the absolute spatial limits of the trap.

However as the particles motion would no longer be accurately represented in this case by 3 decoupled linear mechanical oscillators, the physical interpretation of cooling, for example, the 10th harmonic of z may not lead to a quantum mechanical state in the same way that cooling a singular frequency band per Cartesian degree of freedom might.

7.2.3 Optical multiwells

We generate multiple potential wells defined in space, by a summation of optical potentials and observe particle hopping between the wells. It is demonstrated that the nonlinear motion terms demonstrated by such interferometric means of spatially defining a trap leads to types of nonlinear terms not available by simply driving the particle in a standard Gaussian optical potential.

7.2.4 Nonlinear system sensitivity and identification

A nonlinear system should be naturally more sensitive in a specific frequency band and if the coupling between motional modes is truly tunable then we should be able to pick our enhanced sensitivity band with some freedom. Enhanced sensitivity has been demonstrated in limited experiments. However, real characterization over whether dynamical instability is actually useful as a sensing mode is required, given the obvious caveats of calibration. A more robust experimental proof of this would be elegant.

7.2.5 Bifurcation scan

In addition to generating such systems by perturbing the particles potential in space, we also generate them by perturbing the particles effective potential in time. By systematically scanning a wide range of input modes of the system, we recover chaotic motion for a limited range of inputs, in good agreement with the common understanding of the behaviour of Duffing nonlinearities.

Appendix A

Appendix: How white is the white noise?

A.1 Detecting the instantaneous phase of the particle

We track the phase changes in the particle motion (after filtering for a single degree of freedom), by making use of an digital FM discriminator.

Firstly, the time series represented by an analytic signal $x[n]$ must be transformed:

$$x[n] = X^*[n-1] \tag{A.1}$$

Then we can apply the discriminator:

$$f[n] = atan2\left(\frac{Im(x[n])}{Re(x[n])}\right) \tag{A.2}$$

This allows us to track changes to the particle's phase in real time, helpful as it carries information about the changes to both the particles position and velocity from its interaction with random background gas collisions. The cumulative phase changes for one degree of freedom of the particles motion is given in figure A.1.

A.2 Detrended fluctuation analysis

Detrended fluctuation analysis is a method for determining the type of self correlations present in a signal. [139].

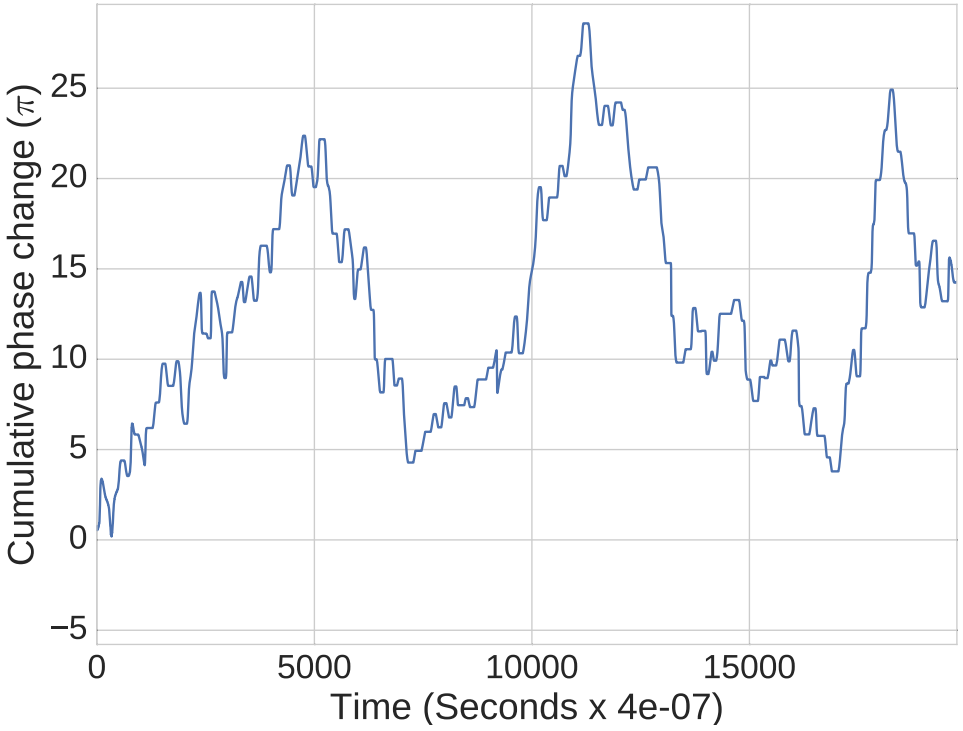

FIGURE A.1: Tracking the phase changes to the particle over time reveal a random walk process.

The fluctuation $F(n)$ of the cumulative sum X_i of a time series x_t from a set a linear trends Y_t fitted to the data in windows of length n [140][141]:

$$F(n) = \sqrt{\frac{1}{N}\Sigma(X_t - Y_t)^2} \tag{A.3}$$

The cumulative sum being given by:

$$X_t = \Sigma(x_i - < x >) \tag{A.4}$$

The values of F(n) for different noise processes are given as:

- $\alpha < \frac{1}{2}$, anti-correlated
- $\alpha \simeq \frac{1}{2}$, uncorrelated white noise
- $\alpha \simeq 1$, 1/f pink noise
- $\alpha > 1$, unbounded process
- $\alpha \simeq \frac{3}{2}$, Brownian noise, Weiner process, Gaussian probability distribution

Applying this method to the cumulative sum of the phase noise of the particle collected in figure A.1, gives a DFA value of F(n) = 1.857, which is fairly close to the $\frac{3}{2}$ we would expect for Weiner process.

A.3 Other applications of DFA numbers - Cryptocurrency trading

Since the DFA number is intended to ascertain the amount of memory in a process, it can also be used to determine is a process is mean reverting. This is helpful if, for example, you want to use a mean reversion trading strategy on a cryptocurrency pair to generate travel money to visit home whilst far away.

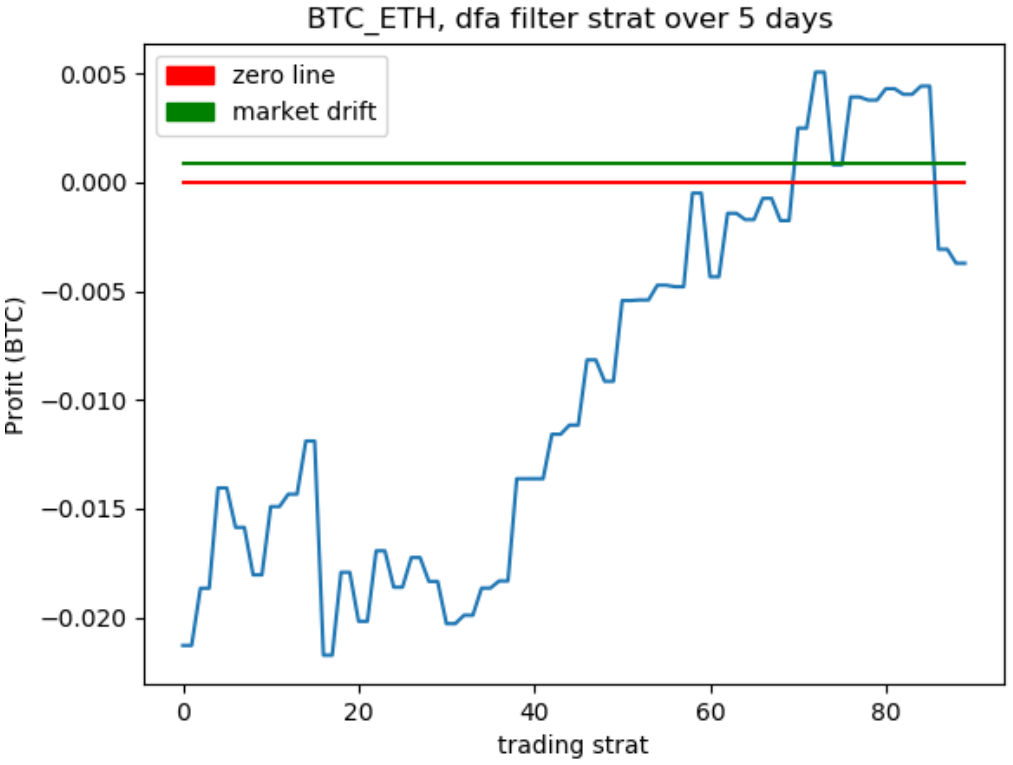

FIGURE A.2: Expected profit of a mean reversion strategy vs time scale in 5 minute intervals.

Appendix B

Appendix: Steady state solution of the Langevin equation.

The Langevin equation describing a particle in a potential V in equilibrium can be defined as:

$$\frac{dx}{dt} = -\frac{1}{\gamma}\frac{\partial V}{\partial x} + \sqrt{2D}\eta(t) \tag{B.1}$$

In which x describes the position of the particle, t its step in time, γ its damping, D its diffusion constant and $\eta(t)$ as Gaussian random noise.

The Fokker-Planck equation is therefore:

$$\frac{\partial P(x,t)}{\partial t} = \frac{1}{\gamma}\frac{\partial}{\partial x}\left(\frac{\partial V(x)}{\partial x}P(x,t)\right) + D\frac{\partial^2 P(x,t)}{\partial^2 t} \tag{B.2}$$

Solving for the steady steady state probability distribution $P_s(x)$, such that $\frac{\partial P(x,t)}{\partial t} = 0$, we see that:

$$\frac{\partial}{\partial x}\left(\frac{1}{\gamma}\frac{\partial V(x)}{\partial x}P_s(x) + D\frac{\partial}{\partial x}P_s(x)\right) = \frac{\partial}{\partial x}J(x) = 0 \tag{B.3}$$

In which J represents the flux of the probability distribution. The boundary conditions imposed by the probability distribution $P_s(x)$ being finite require that J=0 at positive and negative infinity, in addition to $\frac{\partial}{\partial x}J(x) = 0$ required by the solution being for a steady state.

The probability distribution $P_s(x)$ must therefore obey:

$$\frac{1}{\gamma}\frac{\partial V(x)}{\partial x}P_s(x) + D\frac{\partial}{\partial x}P_s(x) = 0 \tag{B.4}$$

One solution of which for $P_s(x)$ (in a steady state) is:

$$P_s(x) = exp(-\frac{V(x)}{\gamma D}) \tag{B.5}$$

Appendix C

Appendix: Clusters

Examples are given here of clusters, trapped in a linear potential, with several discernible additional motional peaks that are not generated through time domain driving, indicative of highly non spherical particles. Furthermore, the additional motional harmonics do not appear at multiples of the prime motional frequencies, indicating genuine additional frequency modes beyond those enabled by entering the nonlinear regime of the Gaussian potential.

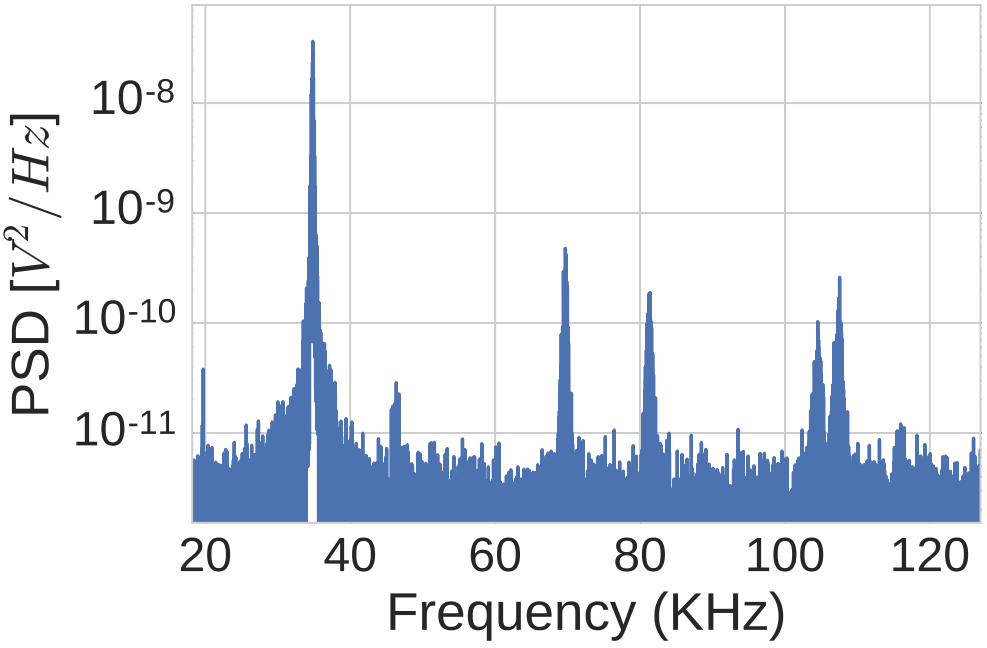

FIGURE C.1: Cluster 1

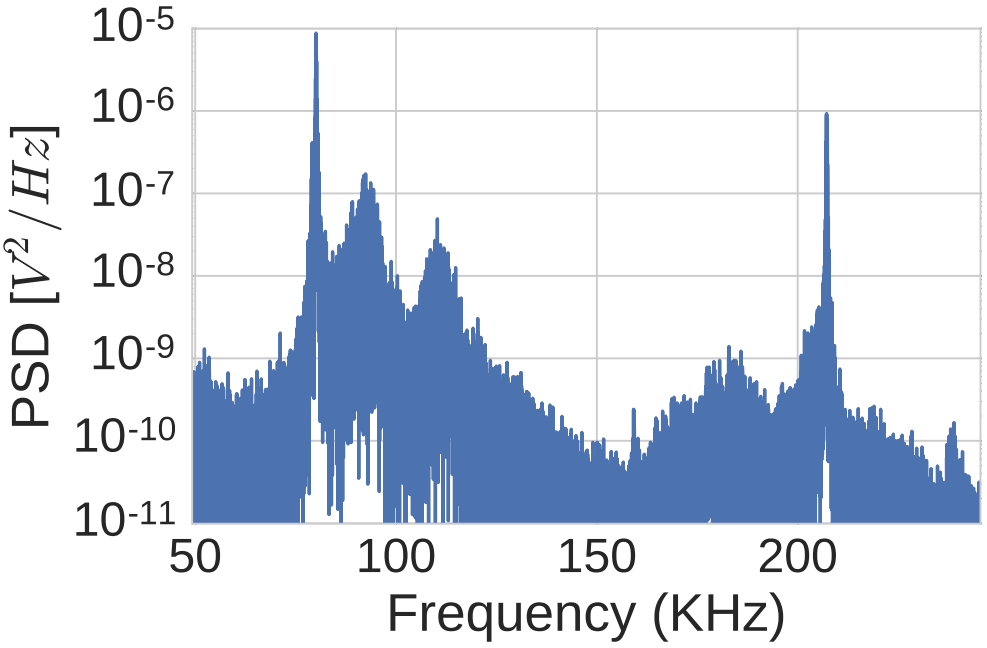

FIGURE C.2: Cluster 2

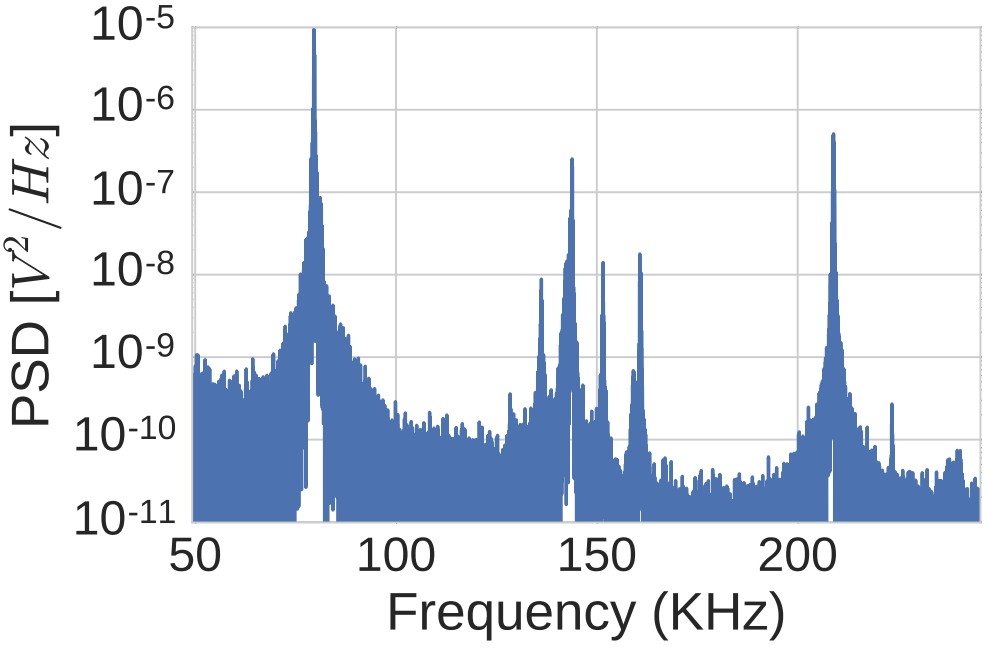

FIGURE C.3: Cluster 3

Appendix D

Appendix: Miniaturized system

For any force sensing or industrial application, it is helpful for any sensing system to be CMOS compatible or at least integrateable on a chip level of critical size [142].

Particle trapping from a thermalised source can be achieved in our system both in the diffusion and ballistic regime, although trapping in the diffusion regime is significantly easier [75].

Integrating our system into chip based architecture will naturally require a microvacuum system. In this section we report on the progress in integrating our high NA parabolic mirror with glass-aluminum bonding technology, such that the space enclosed by the parabola of the mirror becomes the vacuum chamber.

As well as application related motivation, there exists merit in miniaturizing the vacuum system from the point of view of using our levitated nanosphere for fundamental physical tests. An experimental proposal paper by the Atom chip group at Southampton suggests that a micro-vacuum system with passive getter pumping is capable of sustaining a vacuum at $10^{-}10$ for a sustained period of time [142], which rapidly approaches the pressure regimes required for lower (perhaps groundstate[10]) cooling or tests of fundamental collapse models such as CSL[143]. The first milestone of this work however, is just to demonstrate that the actual trapping geometry can realized within such vacuum chip.

D.1 Preliminary Results

Several initial bonding attempts to fuse the parabolic mirror shape to silica glass, an example shown in figure D.2. Bonding performed by Andrei Dragomir.

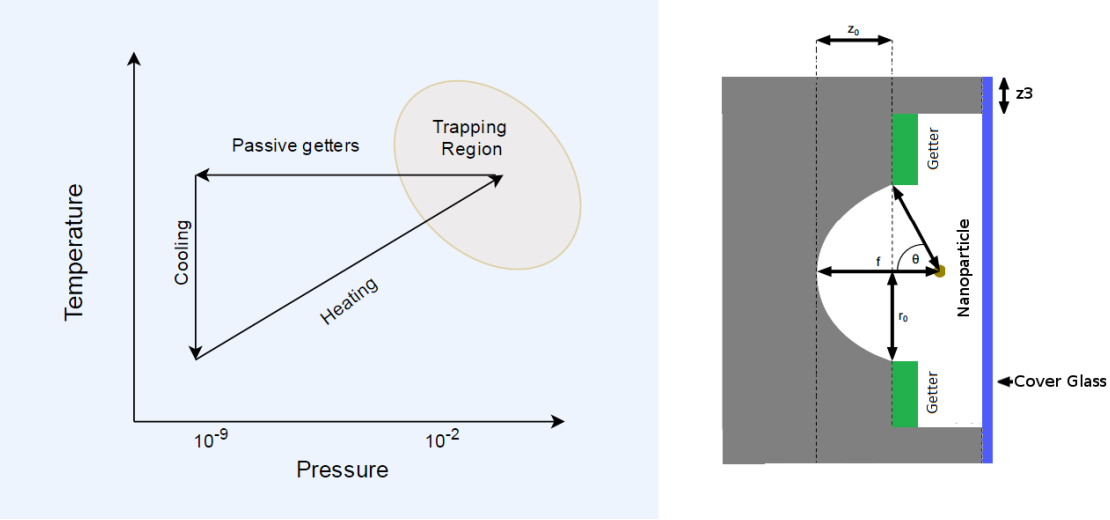

FIGURE D.1: Conceptual diagram of trapping and pumping mechanism (left). There is at time of writing no vacuum compatible nanoparticle source capable of trapping on the order of seconds, the best solution at present requires the use of a buffer gas and experiment data indicates this to be possible up to around 10^{-2} mbar. For a sensing application however we would like as low a pressure as possible. In an chip scale device the only control we have over pressure is by controlling the temperature of the chip, thus the creation of a limit buffer gas could simply be by heating up the whole system. Conceptual geometry of system (right).

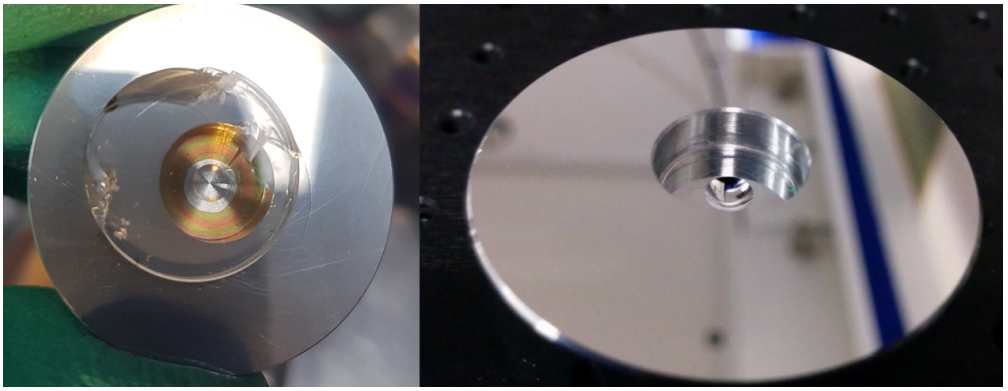

FIGURE D.2: Example of embedded mirror geometry (right) and preliminary at bonding silica glass over micro vacuum region (left). Bonding performed by Andrei Dragomir.

D.1.1 Future systems integration

Several future mission proposals testing quantum mechanics in the mesoscopic regime as being considered by ESA at the study stage[144] [145] [146].

A future cubesatelitte optomechanics mission could serve as a test best for demonstration of the underlying technology.

Any cube satellite or chip satellite mission would likely have a science power budget of a small number of Watts, depending on the specifics of the satellite design. We have previously demonstrated trapping with < 0.5 Watts of laser power from a thermalised source at atmosphere, making this geometry a promising testbed for a small scale demonstration. On the other hand, it has the significant caveat of being closed to space, which would make it unsuitable for proposals to use a levitated nanoparticle to interact with the space environment directly [147].

Appendix E

Appendix: Casimir-Polder Potential

This section is reproduced from the supplmentary material of [148] with the authors permission.

A Casimir-Polder potential is given by:

$$U(z) = \frac{\hbar\mu_0}{8\pi^2}\int_0^\infty \xi^2\alpha(i\xi)\int_{\frac{\xi}{c}}^\infty dk e^{-2kz}[\frac{k-k_1}{k+k_1} + (1-2\frac{k^2c^2}{\xi^2})\frac{\epsilon_1(i\xi)k-k_1}{\epsilon_1(i\xi)k+k_1}] \tag{E.1}$$

where α is the polarizability of the particle, z its distance from the dielectric surface, $\epsilon_1(\omega)$, and k_1 is:

$$k_1 = \sqrt{[\epsilon_1(i\xi)-1]\xi^2/c^2 + k^2} \tag{E.2}$$

In the case of the time-retarded regime as a standard result:

$$U_r = -\frac{C_4}{z^4} \tag{E.3}$$

with C_4 as the non distant dependant terms in the previous equation:

$$C_4 = \frac{3\hbar c\alpha(0)}{64\pi^2\epsilon_0}\int_1^\infty dv(\frac{2}{v^2} - \frac{1}{v^4})\frac{\epsilon(0)v - \sqrt{\epsilon(0)-1+v^2}}{\epsilon(0)v + \sqrt{\epsilon(0)-1+v^2}} \tag{E.4}$$

E.0.1 Casimir-Polder potential

The Casimir-Polder potential $U(z)$ of a particle with polarisibility $\alpha(\omega)$ a distance z from a layer of thickness L and relative permittivity $\epsilon_1(\omega)$, supported by an infinitely deep substrate with relative permittivity $\epsilon_2(\omega)$ is given by [**?**]

$$U_{\rm CP}(z) = \frac{\hbar\mu_0}{8\pi^2}\int_0^\infty \xi^2\alpha(i\xi)\int_{\xi/c}^\infty d\kappa_0\, e^{-2\kappa_0 z}\left[R_{\rm TE}(\kappa_0,\kappa_1,\kappa_2) + \left(1-2\frac{\kappa_0^2c^2}{\xi^2}\right)R_{\rm TM}(\kappa_0,\kappa_1\kappa_2)\right] \tag{E.5}$$

where, for either polarization σ (=TE,TM);

$$R_\sigma = \frac{R_{01}^\sigma + e^{-2\kappa_1 L}R_{12}^\sigma}{1+e^{-2\kappa_1 L}R_{01}^\sigma R_{12}^\sigma} \tag{E.6}$$

with

$$R_{ij}^{\rm TE} = \frac{\kappa_i-\kappa_j}{\kappa_i+\kappa_j} \qquad R_{ij}^{\rm TM} = \frac{\varepsilon_j(i\xi)\kappa_i - \varepsilon_i(i\xi)\kappa_j}{\varepsilon_j(i\xi)\kappa_i + \varepsilon_i(i\xi)\kappa_j} \tag{E.7}$$

and

$$\varepsilon_0(i\xi)=1 \quad \varepsilon_1(i\xi)=\epsilon_{\rm SiO_2}(i\xi) \quad \varepsilon_2(i\xi)=\epsilon_{\rm Si}(i\xi) \quad \kappa_i=\sqrt{\left[\varepsilon_i(i\xi)-1\right]\xi^2/c^2+\kappa_0^2} \tag{E.8}$$

A small sphere of radius R may be modelled via the Clausius-Mossotti polarizability

$$\alpha(\omega) = 4\pi\epsilon_0 R^3\frac{\varepsilon(\omega)-1}{\varepsilon(\omega)+2} \tag{E.9}$$

where $\varepsilon(\omega)$ is the dielectric function of the material from which the sphere is made, and ϵ_0 is the permittivity of free space. Using this relation, equation (E.5) is now a formula whose inputs are the dielectric functions for the media that make up the substrate, layer and sphere, which are all known from experiment. As discussed in the main text, we will eventually approximate this by its large-distance limit near a simple half-space of permittivity $\varepsilon_1(\omega)$, in which case the potential takes on the following form;

$$U_{\rm CP}(z) = -\frac{C_4}{z^4} \tag{E.10}$$

where C_4 is a distance-independent constant defined as [84];

$$C_4 = \frac{3\hbar c\alpha(0)}{64\pi^2\epsilon_0}\int_1^\infty dv\left(\frac{2}{v^2}-\frac{1}{v^4}\right)\frac{\varepsilon_1(0)v-\sqrt{\varepsilon_1(0)-1+v^2}}{\varepsilon_1(0)v+\sqrt{\varepsilon_1(0)-1+v^2}} \tag{E.11}$$

In the experiment presented in the main text the surface is silicon and the sphere is silicon dioxide. We model both of these via an N-resonance Drude-Lorentz permittivities,

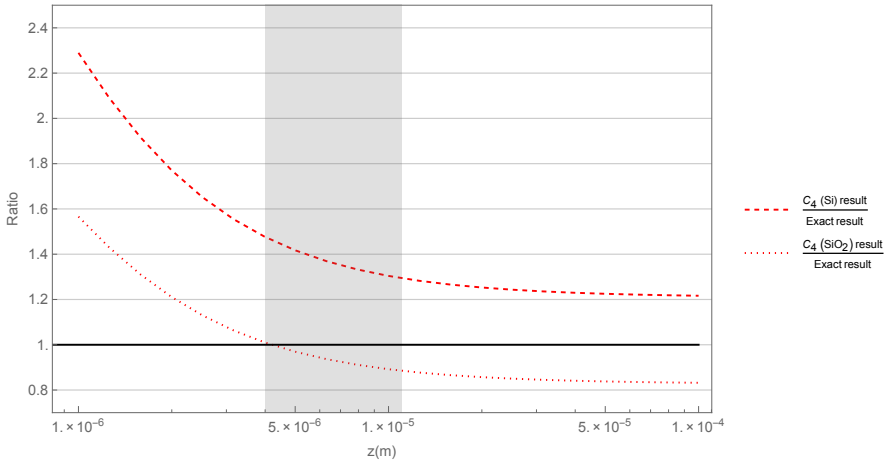

FIGURE E.1: Ratio of the approximations shown in Fig. L.4 to the exact numerical result (which is independent of the radius of the sphere). The silicon dioxide result is seen to agree well within the experimental region of interest.

defined by;

$$\epsilon(\omega) = 1 + \sum_{i=1}^{N} \frac{\omega_{p,i}^2}{\omega_{T,i}^2 - \omega^2 + i\gamma_i\omega} \tag{E.12}$$

Here $\omega_{p,i}$ is the plasma frequency, $\omega_{T,i}$ is the transition frequency and γ_i is the damping frequency, each for the ith resonance of the dielectric function. For silicon we use a single-resonance model, and for silicon dioxide we use a two-resonance model, with parameters from [83] shown in Table (E.1). Using these parameters in Eq. (E.11) we

	i	$\omega_{p,i}$	$\omega_{T,i}$	γ_i
Si	1	23	7.1	0.98
SiO_2	1	0.17	0.13	0.043
	2	29	27	8.1

TABLE E.1: Drude-Lorentz parameters for silicon and silicon dioxide (all values in units of 10^{15}rad/s)

find the dispersion constant C_4 for our particular setup

$$C_4 = (7.60 \times 10^{-28}\text{Jm}) \cdot R^3 \tag{E.13}$$

As a consistency check we evaluate Eq. (E.5) numerically over both distance regimes, the results of this alongside the asymptotic long-distance result according to equation (E.13) are shown in figure L.4 for a range of sphere sizes.

Appendix F

Appendix: Parametric feedback

The parametric feedback routine we use to suppress the motion of the particle to a lower value of $< n >$ is based on a principle of applying a sinusoidal time variation to the normally harmonic trap potential of twice the degree of freedoms oscillation frequency, thus simultaneously arresting the momentum and position modes of the particles motion. Examples of heating and cooling modes of such a feedback scheme are given in figure F.1. A more efficient way of cooling is discussed in [149], where a Kalman filter is used instead of a parametric feedback loop.

FIGURE F.1: Phase solutions of applying a signal at twice the frequency of the mechanical motion of the oscillator. Red is the externally applied signal and blue is the (simulated) motion of the particle.

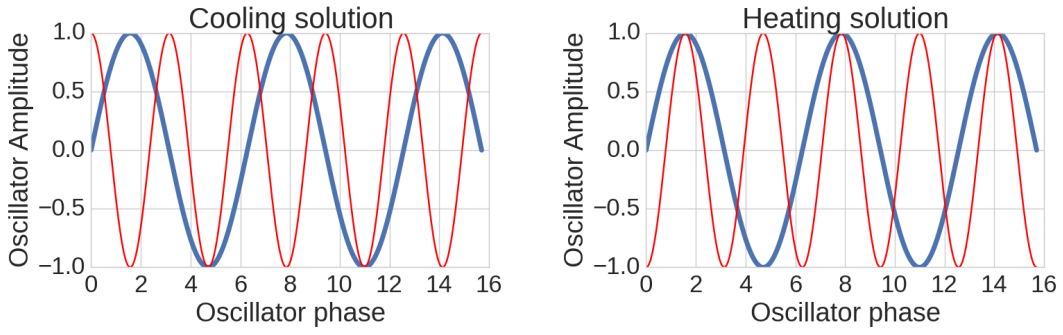

An experimental example of a linear particle with only 3 motional degrees of freedom being cooled under parametric feedback in given in figure F.2.

FIGURE F.2: Particle cooled to milli-Kelvin temperatures. From [9]

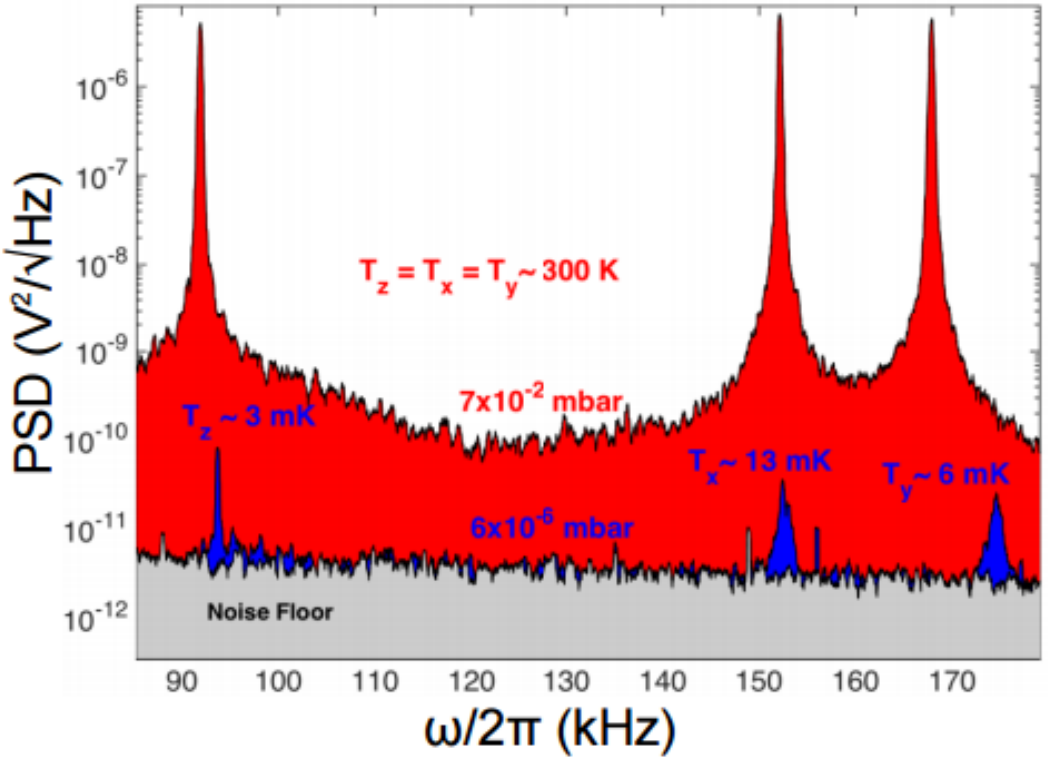

Appendix G

Appendix: Logistics map time traces

Here the full timetraces for paramters of the logistics map are give for the readers understanding.

In the case of the driving paramters such that the oscillation tends to a single value and we recover a single limit cycle, the time trace of the oscillations of the system are given in figure G.1.

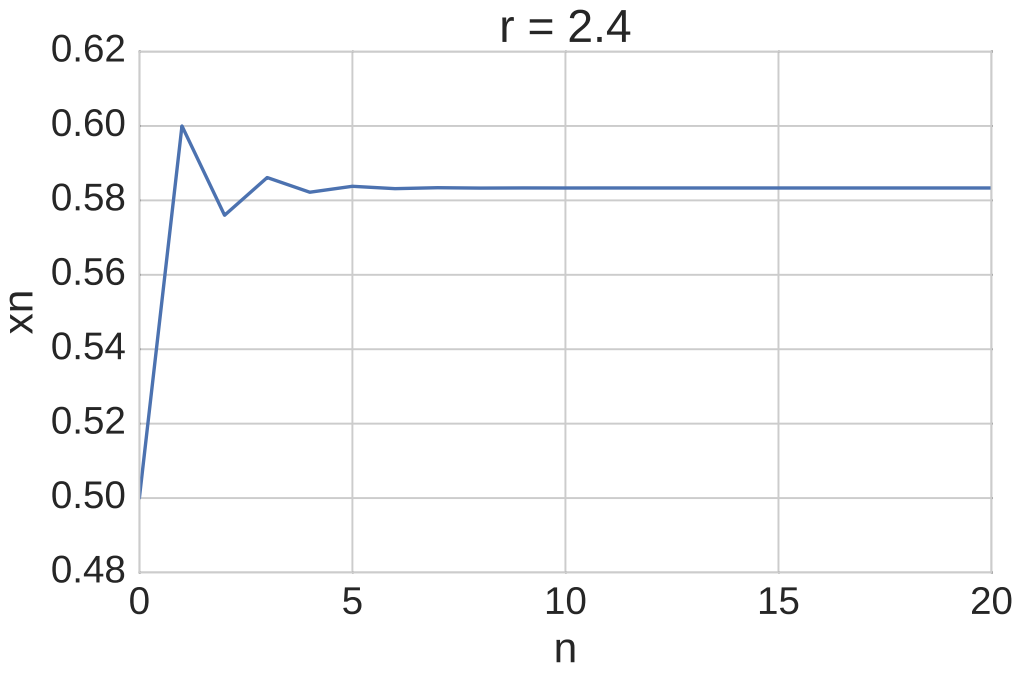

FIGURE G.1: Time trace for logistics map r value for a single limit cycle

In the case of the driving parameters such that the oscillation tends to two values and we recover a bistable limit cycle, the time trace of the oscillations of the system are given in figure G.2.

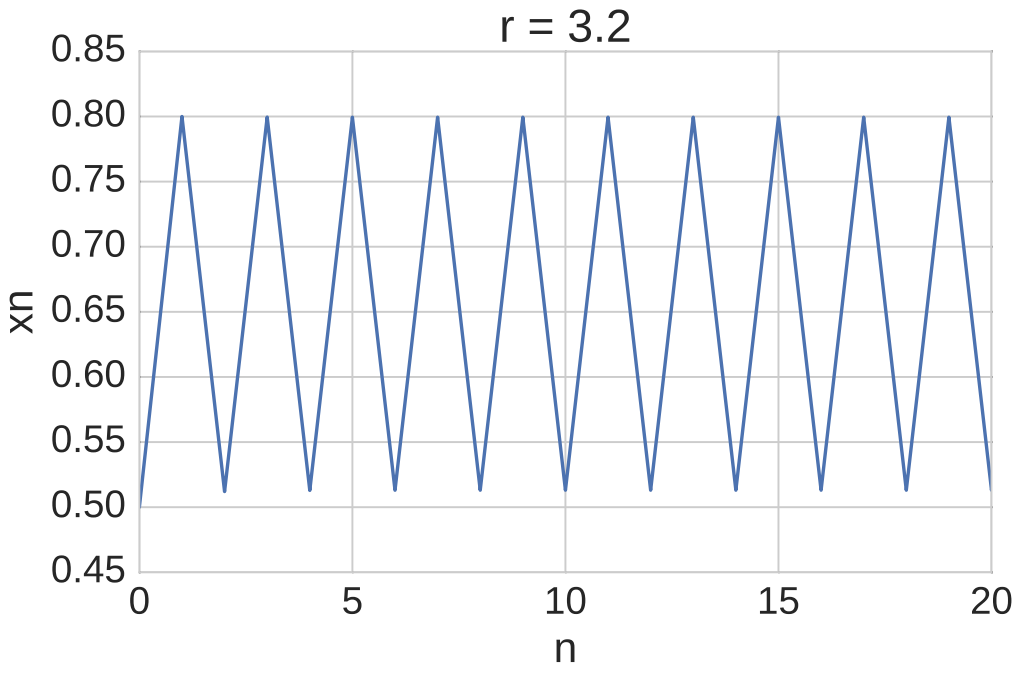

FIGURE G.2: Timetrace for logistics map r value for a bistable limit cycle.

In the case of the driving parameters such that the oscillation tends to no particular value and we recover no single limit cycle, the time trace of the oscillations of the system are given in figure G.3.

G.1 Lyapunov exponent sensitivity to noise

The maximal Lyapunov exponent of a system is often used to quantify or demonstrate chaotic behaviour within it [132]. Typically, a positive Lyapunov exponent can be an indication that the system is indeed displaying chaotic behaviour. It is however as a tool, highly sensitive to noise within the system.

Two driving values of the logistics problem are studied here, one for an r value known to be non chaotic $r = 3.2$ and another known to be chaotic $r = 3.9$, with the time traces for these values given in the previous section. The Lyapunov exponent for these two time traces with increasingly large amounts of noise being added to them are given in figure G.4.

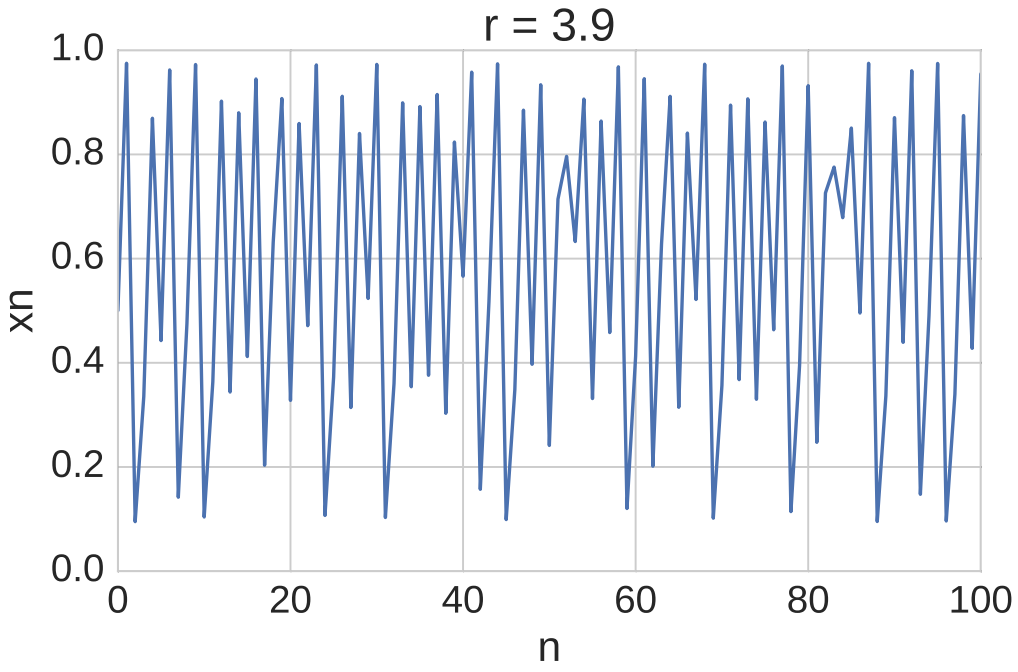

FIGURE G.3: Timetrace for logistics map r value for chaotic region, ie no stable limit cycle.

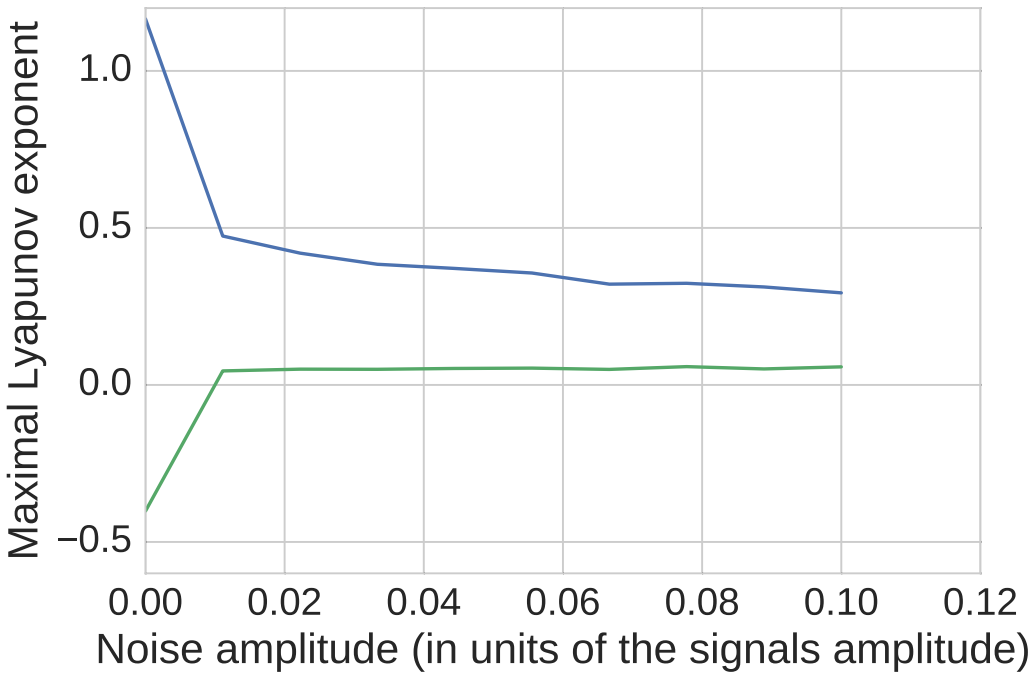

FIGURE G.4: The maximal values for the Lyapunov exponents for chaotic and non chaotic driving values of the logistics problem are given. As increasing amounts of noise are added to the system the Lyapunov exponents becomes an increasingly poor method of discriminating between the chaotic and non chaotic motional modes of the system.

Appendix H

Appendix: Reccurence quantification Analysis

H.0.1 Recurrent Quantification Analysis

As methods of classifying chaotic systems such as Lyapanov exponents are sensitive to noise, recurrence plots are often used to quantify dynamic systems displaying chaotic motion in noisy regimes.

The recurrence of a trajectory is the time it takes to return to the same location[150], a recurrence plot correlates visually the times at which a system visits a similar volume in phase space. It is computed from the following algorithm [135]:

$$R(i,j) = \begin{cases} 1 & if \quad |x(i) - x(j)| < threshold \\ 0 & otherwise \end{cases} \tag{H.1}$$

Generating the recurrence plot of the oscillators time series motion in a method consistent with [135], gives us the plots displayed in Appendix H.1.

Since looking for visually identifiable structure in a complex graph is not an especially scientific way to analyze something, methods exist to quantify the structures generated in recurrence plots as tie them to the nonlinear behaviours present in a system, these are commonly reffered to as RQA metrics.

The RQA metrics for the plots in appendix H.1 are given in table H.0.1. The trapping time (here referring to the RQA metric and not the optomechanical quality related to the potential) as introduced in [135] is correlated with the amount of chaotic states in the system.

The maximal length of the vertical structures generated in the recurrence plot V_{max} represents an established RQA measure for detecting the changes between chaotic and periodic states [135].

The trapping time T, introduced in [135], and defined as the average length of the vertical structures in the recurrence plot of the system:

$$T := \frac{\sum vP(v))}{\sum P(v))}. \tag{H.2}$$

Both of these metrics are greatly increased in the central potential in contrast to the two outer positional states. It is discussed in [135] that RQA metrics based on analyzing vertical line structures can be sensitive to different scale sizes in the embedding of the ta. For this reason we also include average diagonal line length, which is also strongly correlated with the presence of chaotic states and less sensitive to false recurrences.

These numbers suggest that the mutli-well potential with a high proportion of duffing terms in its equation of motion demonstrated more chaotic behaviour than its more linear neighbors, an unsurprising result.

RQA Metric:	Trap 1	Trap 2	Trap 3
Trapping Time	35.22	125.88	57.70
Longest Vertical Line Length	85	210	53
Average Diagonal Line Length	23.15	82.82	41.74

The full output of the recurrence quantification analysis (RQA) is given here. The key element is that the center trap of the spatial double well system displays auto correlation structures common to each of its neighboring traps, again suggesting it to be an intermediate mode of motion between the two potential wells.

FIGURE H.1: Time series and recurrence plots of the first of the spatially defined traps, with some common structures shared with the middle trap in figure H.2.

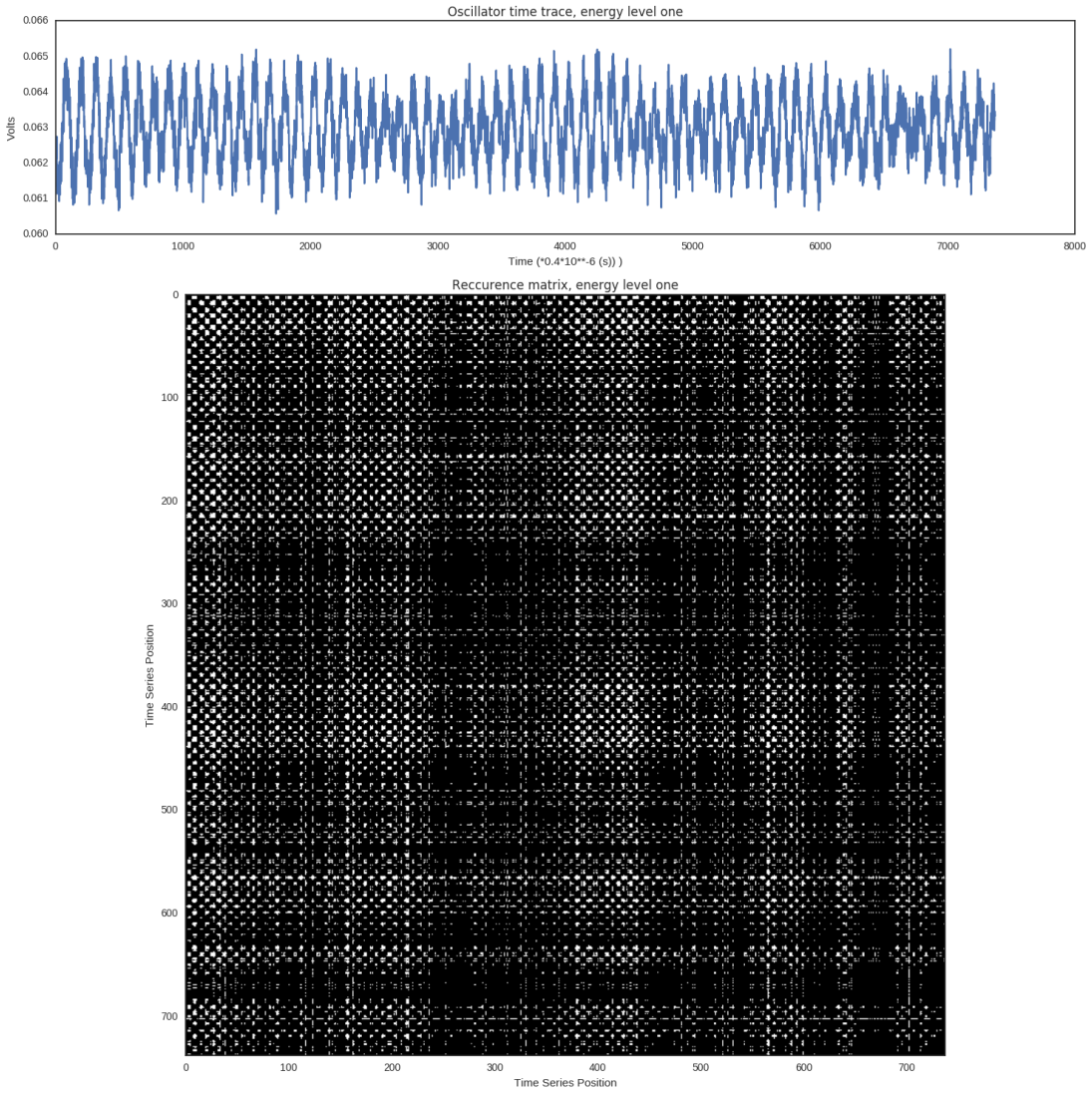

FIGURE H.2: Time series and recurrence plots of middle instance of the spatially defined traps. This center trap demonstrates a convolution of the RQA structures seen in its neighbor traps.

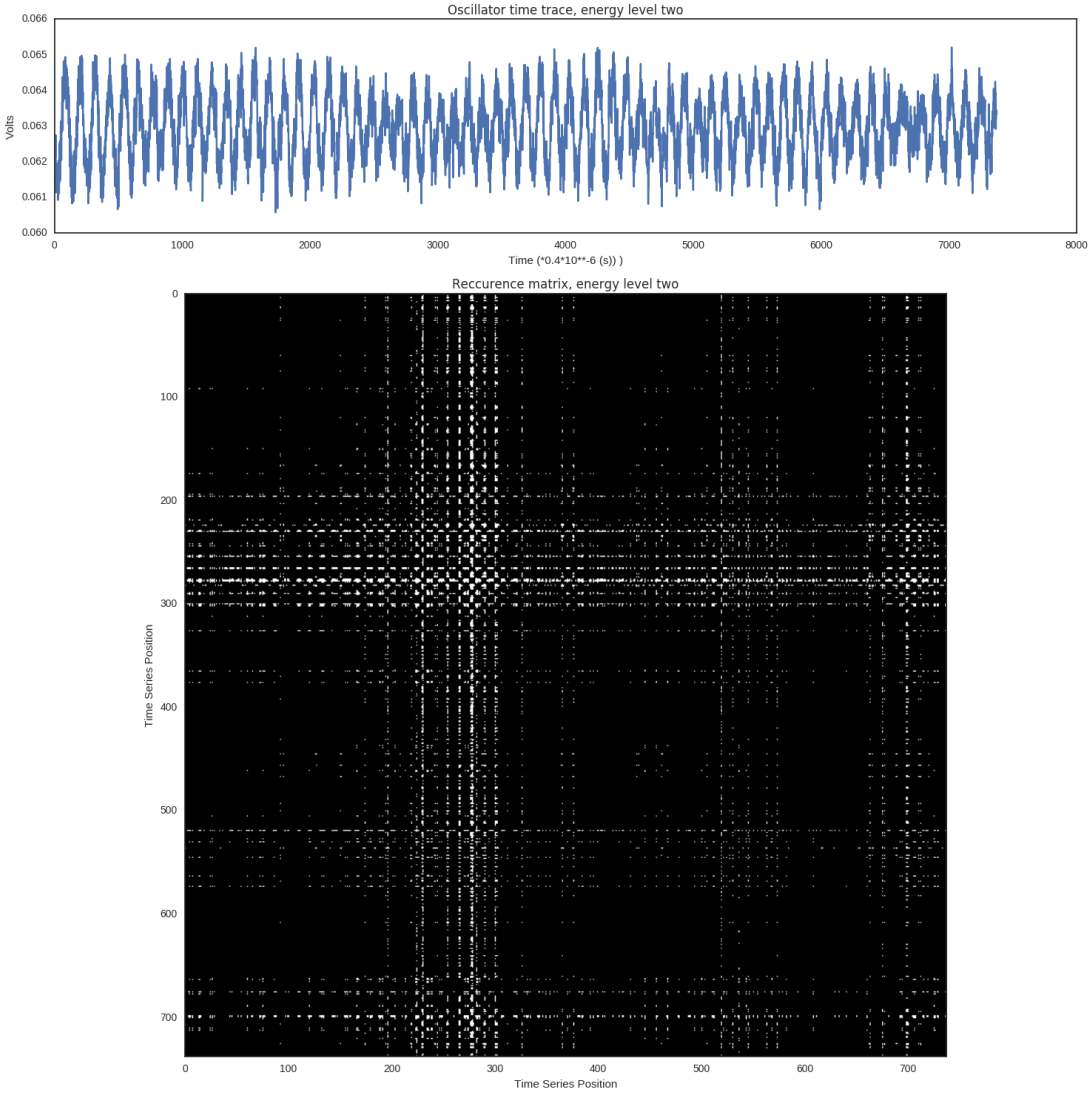

FIGURE H.3: Time series and recurrence plots of the last of the spatially defined traps, with some common structures shared with the middle trap in figure H.2.

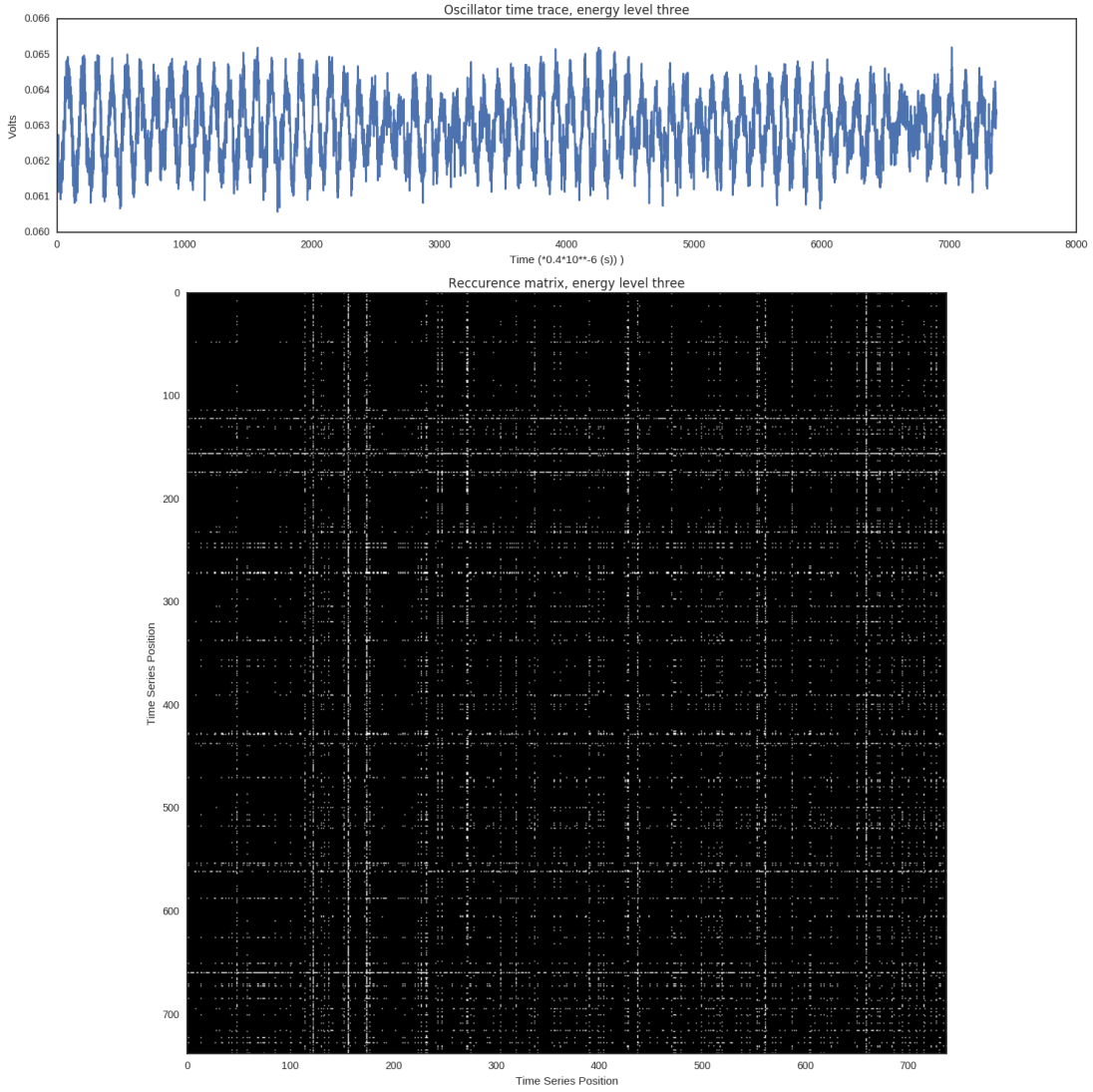

Appendix I

Appendix: Detection function

In this appendix we briefly discuss the detection scheme that allows the particles motion to be read out by interference of light rays that do and do not interact with the particle in its trapping region.

I.1 Detection function for a fixed point in space

For on dimension of the particles motion, in a linear harmonic trap, its motion can be written:

$$z(t) = z_0 = sin(\omega_0 t) \tag{I.1}$$

where z_0 is the maximum extent of the particles motion and ω_0 its frequency. This modulates the scattering field of the particle thus:

$$E_{scattering} = E_{scattering} e^{i\beta sin(\omega_0 t)} \tag{I.2}$$

where β represents the modulation depth:

$$\beta = z_0 \partial\theta \tag{I.3}$$

θ theta represents the phase of the light as it passes through the focus, modulated by its scattering interaction with the levitated nanoparticle by the function:

$$\theta = k_0 z - arctan(\frac{z_0}{z_R}) \tag{I.4}$$

where z_R is the Rayleigh distance. The diverging field that does *not* interaction with the particle can be written as:

$$E_{diverging} = E_{divergingmax} e^{i\phi} \frac{1}{Dtan(\Xi)} \tag{I.5}$$

where $E_{divergingmax}$ is the maximum intensity of the diverging field of the light (located at the focus of the parabolic mirror) and Ξ is the solid angle of the mirror. D is the distance between the focus of the parabolic mirror and the detector, and $\phi = k_0 z_0 + \pi$, π is introduced by the Gouy shift whilst passing through the focus.

This finally leads to:

$$I(t, D) = |E_{scattering} + E_{diverging}|^2 \tag{I.6}$$

I.2 Detection function as a function of nanoparticle - detector distance

This is the detection efficiency for a single degree of the freedom of the nanoparticle as a function of focus-detector distance. In other words the evolution of equation I.6 as a function of the variable D.

Measured detection function for the z degree of motion of a levitated particle is given in figure I.1

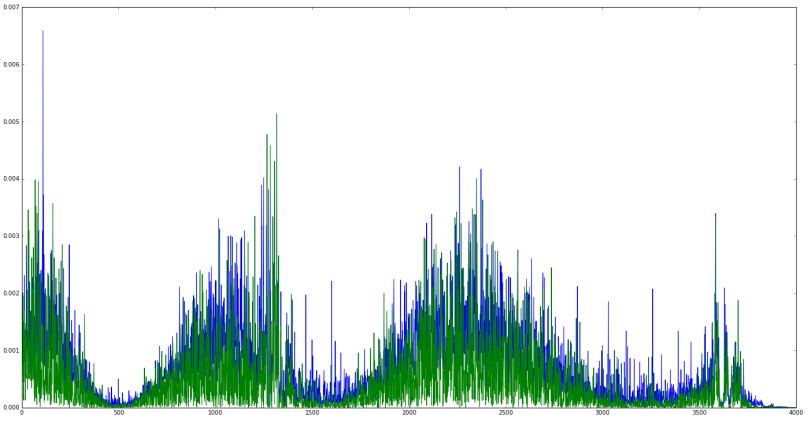

FIGURE I.1: Detection efficiency of Z peak as a function of distance.

Appendix J

Additional Poincare Sections

Poicnare sections of simulated oscillators with increasing duffing parameters and noise respectively.

FIGURE J.1: Poincare Sections of simulated and experimental systems, adding noise to the system expands the poincare section while adding nonlinearities to the underlying potential of an already noisy system compresses the phase in a non cartesian fashion.

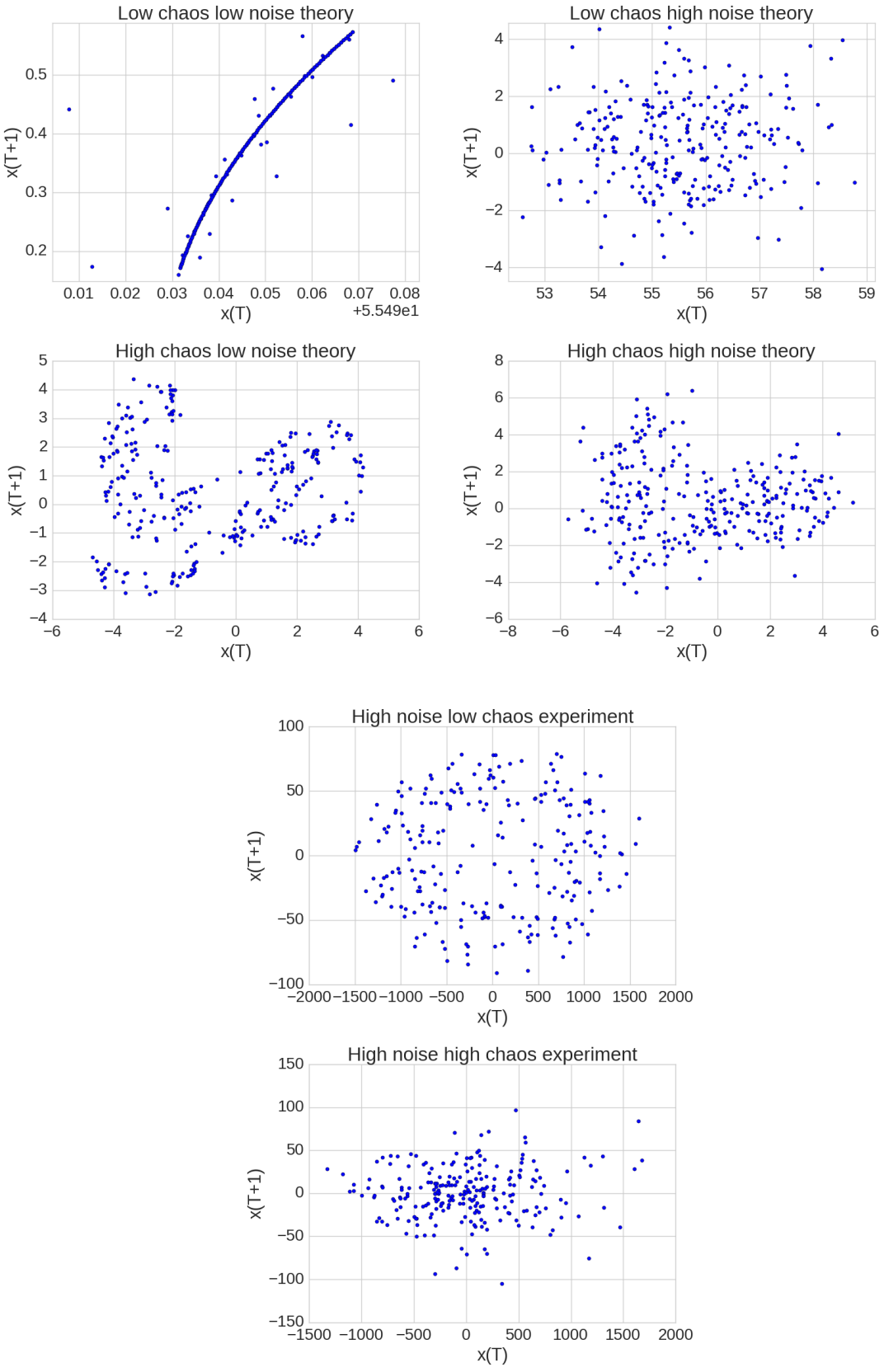

Appendix K

Other Bifurcation graphs

K.1 ring states

While the exact mechanics behind why this takes place are beyond the scope of this thesis, a phase driving solution for the bifurcation scan in section 6 exists such that the phase space of the particle is bi-modal in both position and velocity. Given in figure K.1.

K.2 Bifurcation plots with noise suppression

Naturally, suppressing noise comes with the possibility of suppressing signal, therefore both methods and outputs of producing bifurcation plots are reproduced in this thesis for completeness.

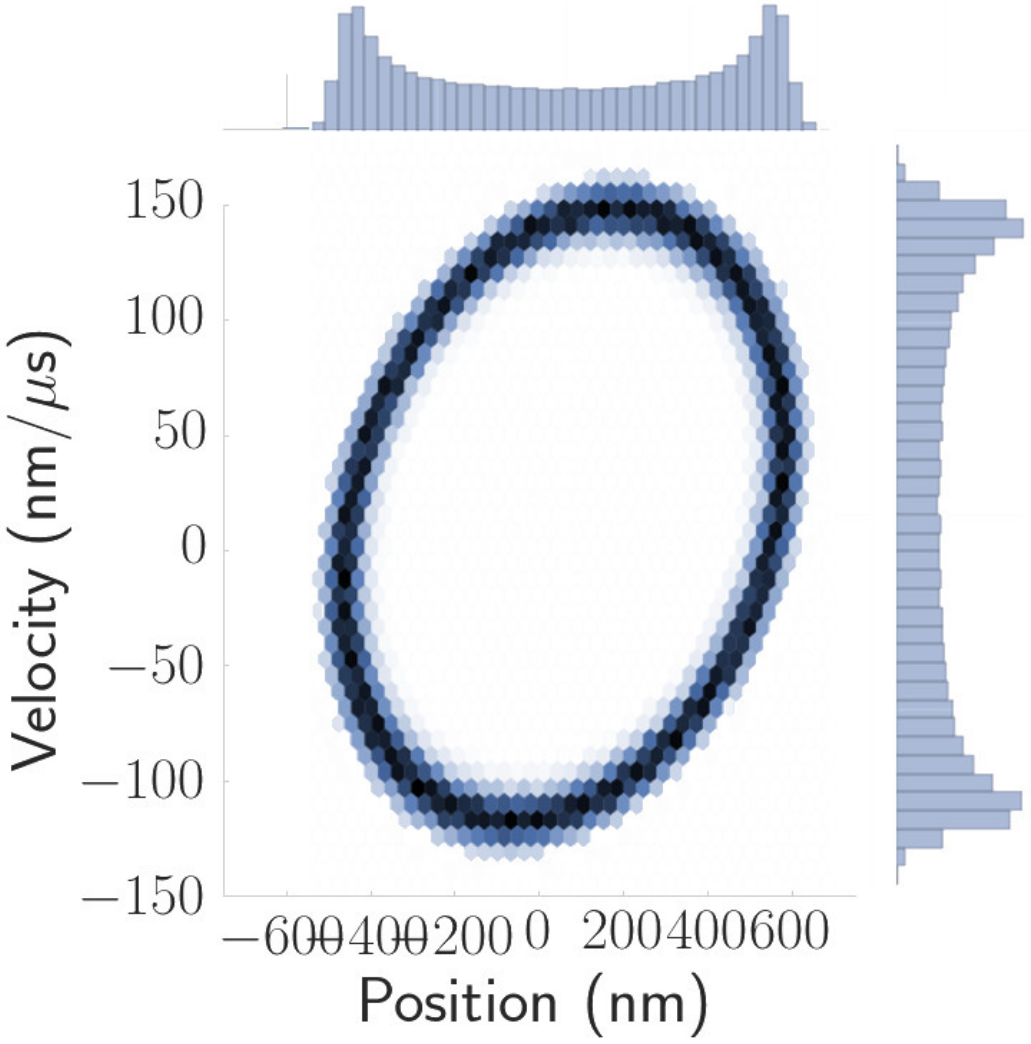

FIGURE K.1: Highly driven nonlinear motional state with a double peaked feature in both position and velocity

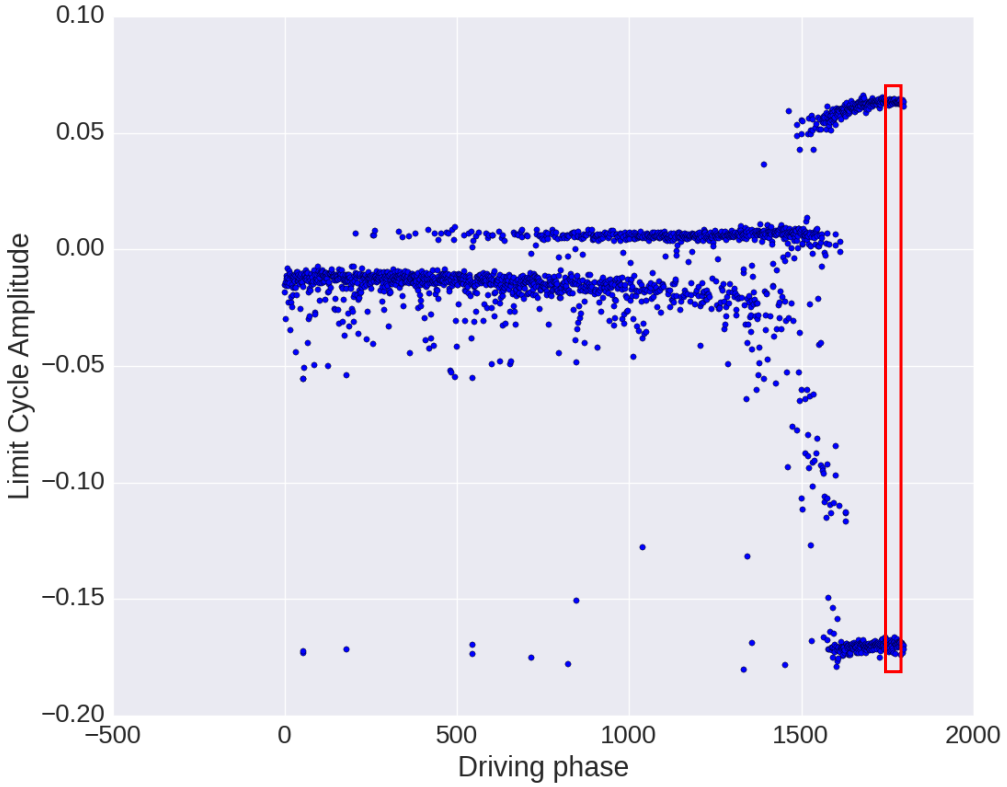

FIGURE K.2: Bifurcation plot for complete phase scan of the system. The system visible transitions from having one central motional mode at one end of the phase spectrum, with extreme duffing behaviour observed at the other end. The central region of the phase scan demonstrates many interesting 3 level systems such as van der pol oscillators and intervals of chaotic behaviour. The section marked by the red box is the dataset shown in figure K.3. The size of the dataset makes the region difficult to see without zooming in as such.

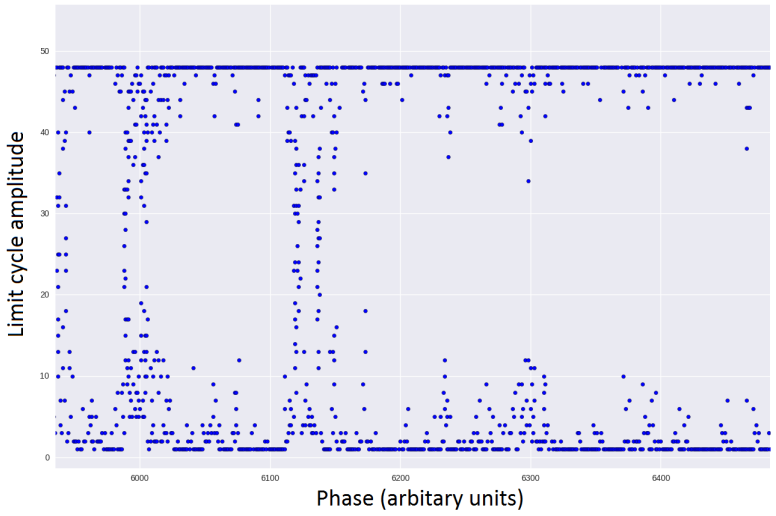

FIGURE K.3: Data shown is the expanded version of the data in the red box shown in figure K.2. The size of the dataset makes the regions of chaotic motion difficult to see without zooming in as such. Transitional behaviour between bimodal duffing oscillator and chaotic behaviour (vertical line sections) for limited values of driving phase.

Appendix L

Appendix: Other surface graphs

L.0.1 2D image extraction from surface potential

An initial attempt at extracting a an image from an unstructured surface is given in figure L.1.

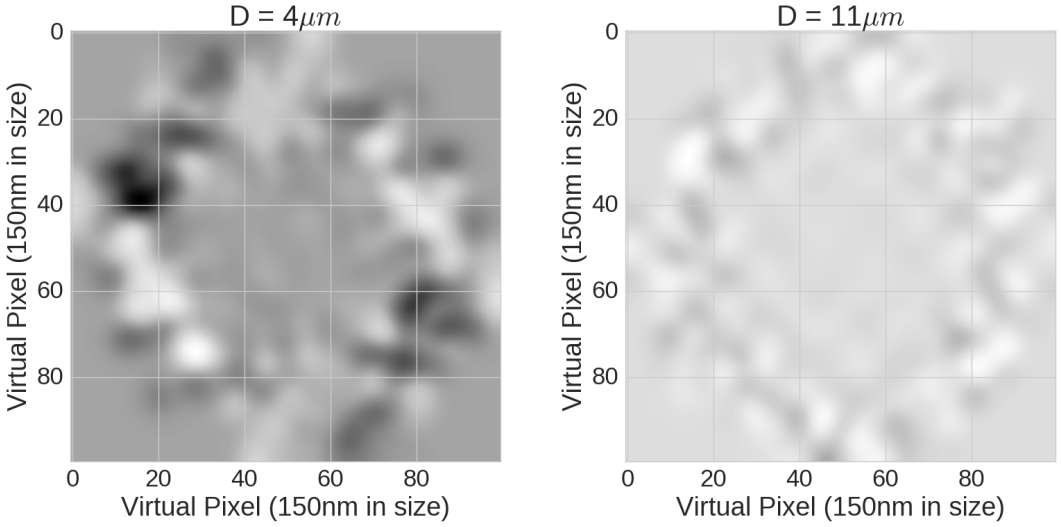

FIGURE L.1: 2D images extracted computing the nanoparticles mean z position for binned values of the x-y plane. Some structure is seem as the particle approaches the surface, however without a known calibration structure to compare this against, no scientific statement can be made from the available data.

L.0.2 Overlaid potentials

The spring functions for the particle close to and far away from the surface are given in figure L.2. Note that the displacement of the center of the trap close to the surface

is likely due to the increase in net (spatially uniform) scattering force in the direction away from the surface.

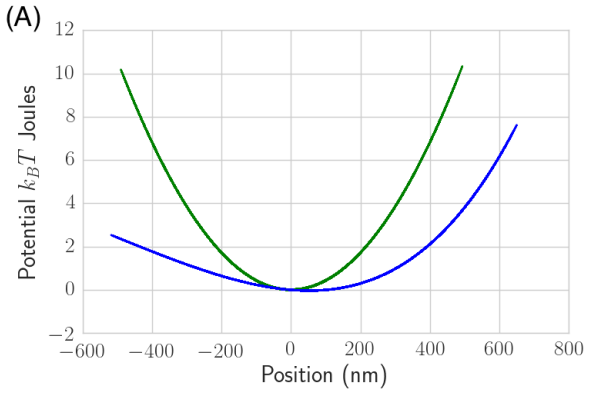

FIGURE L.2: Resultant potentials for the nonlinear (blue) and linear (green) motional states of the particle. Obtained by integrating the spring functions in figure 2.12.

L.0.3 Spring functions - density plots

The density plots of the spring functions for the particle at distances of $4\mu m$ and $11\mu m$ away from the surface are given in figure L.3. The purpose of reproducing the data already present in section 2 in a slightly different plotting style is to aid in the visual identification of the spread in acceleration on the left hand side of the potential of spring function A.

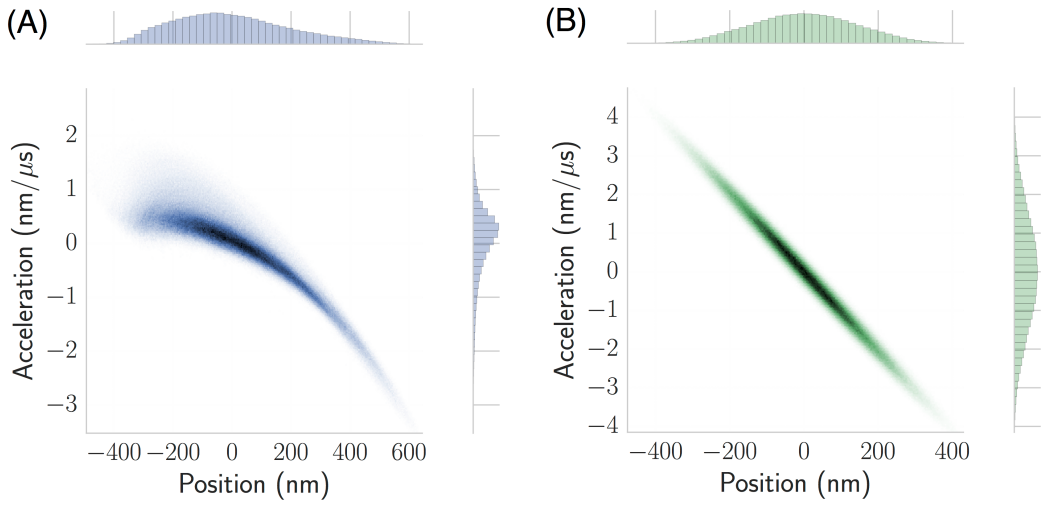

FIGURE L.3: Density plot of spring functions (acceleration/force - position curves) for the non linear motional state of the particle close to the surface (A) and the linear state of the particles motion whilst far away from the surface (B).

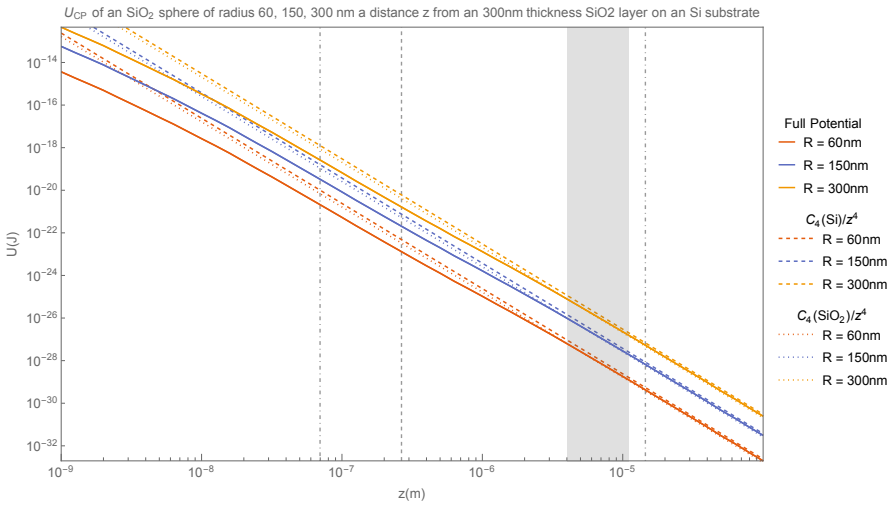

FIGURE L.4: Casimir-Polder potential of an SiO_2 sphere of various radii near an Si plate. The solid curves are exact results found from numerical integration of (E.5), while the dotted curves are from the approximate form equation (E.11). We also show with dashed lines the result of evaluating equation (E.11) using instead the permittivity of Si for the half-space. The absorption wavelengths of the two media involved are shown as vertical lines (dashed for silicon, dot-dashed for silicon dioxide), while the experimental region of interest ($\sim$ 4 to 11μm) is highlighted in grey. It is seen that this experiment is taking place at distances larger than the dominant transition wavelengths of either medium involved (the longer-wavelength silicon dioxide transition is significantly weaker than the shorter-wavelength one, corresponding to a much smaller value of ω_p in Table E.1). Both half-space approximations agree well with the full numerical integration of the layered potential, but in figure E.1 it is seen that closer agreement is found with the silicon dioxide version.

L.0.4 Moving the particle optically

Initially, the nanoparticle - surface distance was varied by moving the nanoparticle optically, rather than moving the surface on a mechanical stage (as is the solution finally used in section 2). The angle is varied by the use of the first half of a Keplarian beam expander (A standard optical component.) such that the beam is converted from collimated to diverging (or converging) but then not normalized back to a collimated beam.

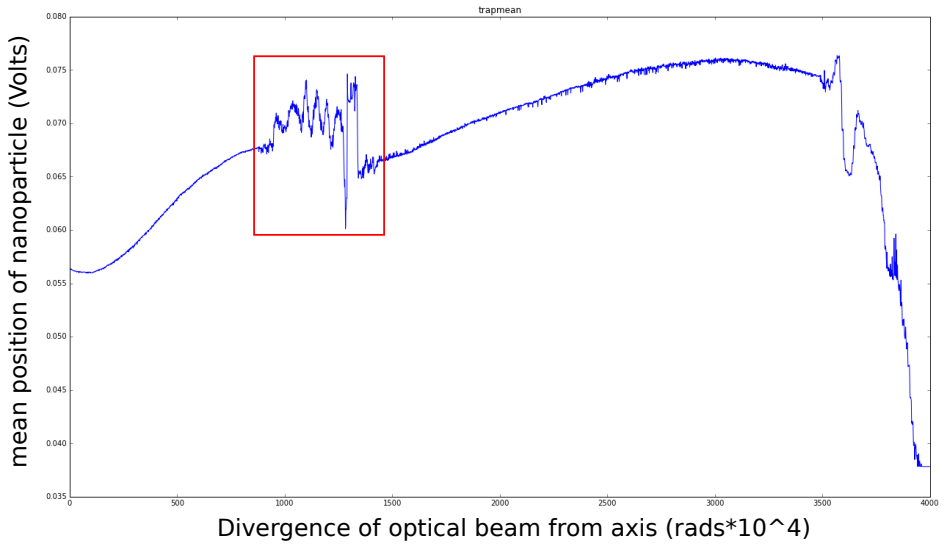

FIGURE L.5: Initial surface experiments moved the particle optically by changing the divergence of the optical beam into the parabolic mirror. This led to a somewhat unstable trap in contrast to the later experiments in which the surface was the mobile component (detailed in section 2). Indeed, the trap becomes so unstable for specific values of the divergence θ that the nanoparticle jumps between several trapping sites, the region surrounded by the red box is the section in which the nanoparticle jumps rapidly between trapping sites, these angle solutions are the ones also used to generate the multiple wells in section 4.

Bibliography

[1] Marko Toroš, Muddassar Rashid, and Hendrik Ulbricht. Simulation of anisotropic particles in levitated optomechanics. 2018. URL https://arxiv.org/abs/1804.01150.

[2] J Millen, T Deesuwan, P Barker, and J Anders. Nanoscale temperature measurements using non-equilibrium Brownian dynamics of a levitated nanosphere. *Nature Nanotechnology*, 9(6):425–9, 2014. ISSN 1748-3395. doi: 10.1038/nnano.2014.82. URL http://www.ncbi.nlm.nih.gov/pubmed/24793558.

[3] Levi P. Neukirch and A. Nick Vamivakas. Nano-optomechanics with optically levitated nanoparticles. *Contemporary Physics*, 56(1):48–62, 2014. ISSN 0010-7514. doi: 10.1080/00107514.2014.969492. URL http://www.tandfonline.com/doi/abs/10.1080/00107514.2014.969492.

[4] Liselle Douyon and David E Schteingart. Lorenz-Mie Scattering. In *Matrix*, volume 31, pages 1–19. 2002. URL http://www.ncbi.nlm.nih.gov/pubmed/12055988.

[5] J Bateman, I McHardy, A Merle, T R Morris, and H Ulbricht. On the existence of low-mass dark matter and its direct detection. *Scientific Reports*, 5, 2015. doi: 10.1038/srep08058. URL https://doi.org/10.1038/srep08058.

[6] C Jess Riedel. Direct detection of classically undetectable dark matter through quantum decoherence. *Physical Review D*, 88(11):116005, 2013.

[7] C Jess Riedel. Decoherence from classically undetectable sources: Standard quantum limit for diffusion. *Physical Review A*, 92(1):010101, 2015.

[8] C Jess Riedel and Itay Yavin. Decoherence as a way to measure extremely soft collisions with dark matter. *Physical Review D*, 96(2):023007, 2017.

[9] Muddassar Rashid, Tommaso Tufarelli, James Bateman, Jamie Vovrosh, David Hempston, M. S. Kim, and Hendrik Ulbricht. Experimental Realisation of a Thermal Squeezed State of Levitated Optomechanics. 10:1–6, 2016. URL http://arxiv.org/abs/1607.05509.

[10] Vijay Jain, Jan Gieseler, Clemens Moritz, Christoph Dellago, Romain Quidant, and Lukas Novotny. Direct Measurement of Photon Recoil from a Levitated Nanoparticle. *Physical Review Letters*, pages 3–7, 2016. ISSN 0031-9007. doi: 10.1103/PhysRevLett.116.243601.

[11] Markus Aspelmeyer, Tobias J. Kippenberg, and Florian Marquardt. Cavity Optomechanics. 2013. ISSN 0034-6861. doi: 10.1103/RevModPhys.86.1391.

[12] Igor Pikovski, Michael R. Vanner, Markus Aspelmeyer, Myungshik Kim, and Caslav Brukner. Probing Planck-scale physics with quantum optics. *Nature Physics*, 8:393–398, 2011. ISSN 1745-2473. doi: 10.1038/nphys2262.

[13] Zhang-qi Yin, Tongcang Li, Xiang Zhang, and LM Duan. Large quantum superpositions of a levitated nanodiamond through spin-optomechanical coupling. *Physical Review A*, 88(3):033614, 2013.

[14] LIGO Scientific, BP Abbott, R Abbott, TD Abbott, F Acernese, K Ackley, C Adams, T Adams, P Addesso, RX Adhikari, et al. Gw170104: observation of a 50-solar-mass binary black hole coalescence at redshift 0.2. *Physical Review Letters*, 118(22):221101, 2017.

[15] F Acernese, M Agathos, K Agatsuma, D Aisa, N Allemandou, A Allocca, J Amarni, P Astone, G Balestri, G Ballardin, et al. Advanced virgo: a second-generation interferometric gravitational wave detector. *Classical and Quantum Gravity*, 32(2):024001, 2014.

[16] Emanuele Berti, Vitor Cardoso, and Clifford M Will. Gravitational-wave spectroscopy of massive black holes with the space interferometer lisa. *Physical Review D*, 73(6):064030, 2006.

[17] Jasper Chan, TP Mayer Alegre, Amir H Safavi-Naeini, Jeff T Hill, Alex Krause, Simon Gröblacher, Markus Aspelmeyer, and Oskar Painter. Laser cooling of a nanomechanical oscillator into its quantum ground state. *Nature*, 478(7367):89, 2011.

[18] Jan Gieseler, Lukas Novotny, and Romain Quidant. Thermal nonlinearities in a nanomechanical oscillator. *Nature Phys*, 9(12):806–810, 2013. ISSN 1745-2473. doi: 10.1038/nphys2798.

[19] Marissa Giustina, Marijn AM Versteegh, Sören Wengerowsky, Johannes Handsteiner, Armin Hochrainer, Kevin Phelan, Fabian Steinlechner, Johannes Kofler, Jan-Åke Larsson, Carlos Abellán, et al. Significant-loophole-free test of bells theorem with entangled photons. *Physical Review Letters*, 115(25):250401, 2015.

[20] Anton Zeilinger, Roland Gähler, CG Shull, Wolfgang Treimer, and Walter Mampe. Single-and double-slit diffraction of neutrons. *Reviews of Modern Physics*, 60(4): 1067, 1988.

[21] MR Andrews, CG Townsend, H-J Miesner, DS Durfee, DM Kurn, and W Ketterle. Observation of interference between two bose condensates. *Science*, 275(5300): 637–641, 1997.

[22] S Nimmrichter. *Macroscopic matter wave interferometry*. Springer, Switzerland, 2014. URL https://doi.org/10.1007/978-3-319-07097-1. DOI: 10.1007/978-3-319-07097-1.

[23] Stefan Nimmrichter and Klaus Hornberger. Macroscopicity of mechanical quantum superposition states. *Physical Review Letters*, 110(16):160403, 2013.

[24] Markus Arndt, Olaf Nairz, Julian Vos-Andreae, Claudia Keller, Gerbrand Van der Zouw, and Anton Zeilinger. Wave–particle duality of c 60 molecules. *nature*, 401 (6754):680, 1999.

[25] Stefan Gerlich, Sandra Eibenberger, Mathias Tomandl, Stefan Nimmrichter, Klaus Hornberger, Paul J Fagan, Jens Tüxen, Marcel Mayor, and Markus Arndt. Quantum interference of large organic molecules. *Nature communications*, 2:263, 2011.

[26] James Bateman, Stefan Nimmrichter, Klaus Hornberger, and Hendrik Ulbricht. Near-field interferometry of a free-falling nanoparticle from a point-like source. *Nature Communications*, 5:4788, 2014.

[27] H Pino, J Prat-Camps, K Sinha, B Prasanna Venkatesh, and O Romero-Isart. Magnetic skatepark for quantum interference of a superconducting microsphere. *arXiv preprint arXiv:1603.01553*, 2016.

[28] Maximilian Schlosshauer. Decoherence, the measurement problem, and interpretations of quantum mechanics. *Reviews of Modern Physics*, 76(4):1267, 2005.

[29] Philip Pearle, James Ring, Juan I Collar, and Frank T Avignone. The csl collapse model and spontaneous radiation: an update. *Foundations of Physics*, 29(3):465–480, 1999.

[30] Mohammad Bahrami, André Großardt, Sandro Donadi, and Angelo Bassi. The schrödinger–newton equation and its foundations. *New Journal of Physics*, 16(11): 115007, 2014.

[31] M Bahrami, A Bassi, S McMillen, M Paternostro, and H Ulbricht. Is gravity quantum? *arXiv preprint arXiv:1507.05733*, 2015.

[32] CR Pringle. The ordermononegavirales. *Archives of virology*, 117(1-2):137–140, 1991.

[33] O Romero-Isart, L Clemente, C Navau, A Sanchez, and JI Cirac. Quantum magnetomechanics with levitating superconducting microspheres. *Physical Review Letters*, 109(14):147205, 2012.

[34] Gambhir Ranjit, Mark Cunningham, Kirsten Casey, and Andrew A. Geraci. Zeptonewton force sensing with nanospheres in an optical lattice. page 5, 2016. ISSN 2469-9926. doi: 10.1103/PhysRevA.93.053801.

[35] Michael Konopik, Alexander Friedenberger, Nikolai Kiesel, and Eric Lutz. Nonequilibrium information erasure below $k_b t\ln(2)$. *arXiv preprint arXiv:1806.01034*, 2018.

[36] J Millen, T Deesuwan, P Barker, and Janet Anders. Nanoscale temperature measurements using non-equilibrium brownian dynamics of a levitated nanosphere. *Nature Nanotechnology*, 9(6):425, 2014.

[37] Markus Aspelmeyer, Tobias J. Kippenberg, and Florian Marquardt. Cavity optomechanics. *Reviews of Modern Physics*, 86(4):1391–1452, 2014. ISSN 15390756. doi: 10.1103/RevModPhys.86.1391.

[38] Marko Toroš, Muddassar Rashid, and Hendrik Ulbricht. Detection of anisotropic particles in levitated optomechanics. *arXiv preprint arXiv:1804.01150*, 2018.

[39] René Reimann, Michael Doderer, Erik Hebestreit, Rozenn Diehl, Martin Frimmer, Dominik Windey, Felix Tebbenjohanns, and Lukas Novotny. GHz rotation of an optically trapped nanoparticle in vacuum. *arXiv preprint arXiv:1803.11160*, 2018.

[40] J Millen, T Deesuwan, P Barker, and J Anders. Nanoscale temperature measurements using non-equilibrium Brownian dynamics of a levitated nanosphere. *Nature Nanotechnology*, 9, 2014. doi: 10.1038/nnano.2014.82. URL https://doi.org/10.1038/nnano.2014.82.

[41] Jan Gieseler, Romain Quidant, Christoph Dellago, and Lukas Novotny. Dynamic relaxation of a levitated nanoparticle from a non-equilibrium steady state. *Nature Nanotechnology*, 9(5):358–64, 2014. ISSN 1748-3395. doi: 10.1038/nnano.2014.40. URL http://www.ncbi.nlm.nih.gov/pubmed/24681775.

[42] Aaron D OConnell, Max Hofheinz, Markus Ansmann, Radoslaw C Bialczak, Mike Lenander, Erik Lucero, Matthew Neeley, Daniel Sank, H Wang, M Weides, et al. Quantum ground state and single-phonon control of a mechanical resonator. *Nature*, 464(7289):697, 2010.

[43] Ludovico Latmiral and Florian Mintert. Deterministic preparation of highly non-classical quantum states of massive oscillators. 2017. URL http://arxiv.org/abs/1705.10334.

[44] MR Vanner, J Hofer, GD Cole, and M Aspelmeyer. Cooling-by-measurement and mechanical state tomography via pulsed optomechanics. *Nature Communications*, 4:2295, 2013.

[45] TJ Milburn, MS Kim, and MR Vanner. Nonclassical-state generation in macroscopic systems via hybrid discrete-continuous quantum measurements. *Physical Review A*, 93(5):053818, 2016.

[46] R. A. Norte, J. P. Moura, and S. Groblacher. Mechanical Resonators for Quantum Optomechanics Experiments at Room Temperature. *Physical Review Letters*, 116 (14):1–11, 2016. ISSN 10797114. doi: 10.1103/PhysRevLett.116.147202.

[47] David Hempston, Jamie Vovrosh, Marko Toroš, George Winstone, Muddassar Rashid, and Hendrik Ulbricht. Force sensing with an optically levitated charged nanoparticle. *Applied Physics Letters*, 111(13):133111, 2017.

[48] Fernando Monteiro, Sumita Ghosh, Adam Getzels Fine, and David C Moore. Optical levitation of 10 nanogram spheres with nano-g acceleration sensitivity. *arXiv preprint arXiv:1711.04675*, 2017.

[49] Asimina Arvanitaki and Andrew A Geraci. Detecting high-frequency gravitational waves with optically levitated sensors. *Physical review letters*, 110(7):071105, 2013.

[50] CC Heyde. Central limit theorem. *Wiley StatsRef: Statistics Reference Online*, 2014. URL https://onlinelibrary.wiley.com/doi/abs/10.1002/9781118445112.stat04559.

[51] John E Greivenkamp. *Field guide to geometrical optics*, volume 1. SPIE Press Bellingham, WA, 2004.

[52] Craig F Bohren and Donald R Huffman. *Absorption and Scattering by an Arbitrary Particle*. Wiley Online Library, 2007. URL https://onlinelibrary.wiley.com/doi/10.1002/9783527618156.ch3.

[53] Benjamin J Sumlin, William R Heinson, and Rajan K Chakrabarty. Retrieving the aerosol complex refractive index using pymiescatt: A mie computational package with visualization capabilities. *Journal of Quantitative Spectroscopy and Radiative Transfer*, 205:127–134, 2018.

[54] Tongcang Li. *Fundamental tests of physics with optically trapped microspheres*. Springer Science & Business Media, 2012.

[55] Yasuhiro Harada and Toshimitsu Asakura. Radiation forces on a dielectric sphere in the rayleigh scattering regime. *Optics communications*, 124(5-6):529–541, 1996.

[56] J Bateman, S Nimmrichter, K Hornberger, and H Ulbricht. Near-field interferometry of a free-falling nanoparticle from a point-like source. *Nature Communications*, 5, 2014. doi: 10.1038/ncomms5788. URL https://doi.org/10.1038/ncomms5788.

[57] Rainer Kaltenbaek, Markus Aspelmeyer, Peter F Barker, Angelo Bassi, James Bateman, Bruno Christophe, and Michael Chwalla. Macroscopic Quantum Resonators (MAQRO): 2015 update. *EPJ Quantum Technology*, 2016. doi: 10.1140/epjqt/s40507-016-0043-7.

[58] L. Rondin, J. Gieseler, F. Ricci, R. Quidant, C. Dellago, and L. Novotny. Direct Measurement of Kramers Turnover with a Levitated Nanoparticle. pages 1–12, 2017. URL http://arxiv.org/abs/1703.07699.

[59] Hart Goldman Geraci, Andrew. Sensing Short-Range Forces with a Nanosphere Matter-Wave Interferometer. 2014. doi: 10.1103/PhysRevD.92.062002. URL http://arxiv.org/pdf/1412.4482v1.pdf.

[60] Desmond J Higham. An algorithmic introduction to numerical simulation of stochastic differential equations. *SIAM Review*, 43(3):525–546, 2001.

[61] Rebecca L Honeycutt. Stochastic runge-kutta algorithms. i. white noise. *Physical Review A*, 45(2):600, 1992.

[62] Erik Hebestreit, Martin Frimmer, Ren Reimann, and Lukas Novotny. Sensing of Static Forces with Free-Falling Nanoparticles. 2017. URL http://arxiv.org/abs/1801.01169.

[63] L Rondin, J Gieseler, F Ricci, R Quidant, C Dellago, and L Novotny. Direct Measurement of Kramers Turnover with a Levitated Nanoparticle. pages 1–12, 2017.

[64] L. Rondin, J. Gieseler, F. Ricci, R. Quidant, C. Dellago, and L. Novotny. Direct Measurement of Kramers Turnover with a Levitated Nanoparticle. pages 1–12, 2017. URL http://arxiv.org/abs/1703.07699.

[65] George Winstone, Markus Rademacher, Robert Bennett, Stefan Buhmann, and Hendrik Ulbricht. Direct measurement of short-range forces with a levitated nanoparticle. *arXiv preprint arXiv:1712.01426*, 2017.

[66] Sandeep Tyagi, Axel Arnold, and Christian Holm. Electrostatic layer correction with image charges: A linear scaling method to treat slab 2 d+ h systems with dielectric interfaces. *The Journal of Chemical Physics*, 129(20):11B616, 2008.

[67] Hendrick BG Casimir. On the attraction between two perfectly conducting plates. In *Proc. Kon. Ned. Akad. Wet.*, volume 51, page 793, 1948.

[68] Stefan Yoshi Buhmann. *Dispersion forces I: Macroscopic quantum electrodynamics and ground-state Casimir, Casimir–Polder and van der Waals Forces*, volume 247. Springer, 2013.

[69] Steve K Lamoreaux. Demonstration of the casimir force in the 0.6 to 6 μ m range. *Physical Review Letters*, 78(1):5, 1997.

[70] Umar Mohideen and Anushree Roy. Precision measurement of the casimir force from 0.1 to 0.9 μ m. *Physical Review Letters*, 81(21):4549, 1998.

[71] A. Shih and V. A. Parsegian. Van der Waals forces between heavy alkali atoms and gold surfaces: Comparison of measured and predicted values. *Physical Review A*, 12(3):835–841, 1975. ISSN 10502947. doi: 10.1103/PhysRevA.12.835.

[72] CI Sukenik, MG Boshier, D Cho, V Sandoghdar, and EA Hinds. Measurement of the casimir-polder force. *Physical review letters*, 70(5):560, 1993.

[73] John Michael Obrecht, RJ Wild, M Antezza, LP Pitaevskii, S Stringari, and Eric A Cornell. Measurement of the temperature dependence of the casimir-polder force. *Physical review letters*, 98(6):063201, 2007.

[74] Helmar Bender, Christian Stehle, Claus Zimmermann, Sebastian Slama, Johannes Fiedler, Stefan Scheel, Institut Physik, Universitt Rostock, D Rostock, and Stefan Yoshi Buhmann. Probing Atom-Surface Interactions by Diffraction of Bose-Einstein Condensates. *Physical Review X*, 011029:1–10, 2014. doi: 10.1103/PhysRevX.4.011029.

[75] Hart Goldman Geraci, Andrew. Sensing Short-Range Forces with a Nanosphere Matter-Wave Interferometer. *Physical Review D*, 2014. doi: 10.1103/PhysRevD.92.062002.

[76] Asimina Arvanitaki and Andrew A. Geraci. Detecting high-frequency gravitational waves with optically-levitated sensors. *Physical Review Letters*, 2012. doi: 10.1103/PhysRevLett.110.071105.

[77] Alejandro Manjavacas, Francisco J. Rodriguez-Fortuno, F. Javier Garcia De Abajo, and Anatoly V. Zayats. Lateral Casimir Force on a Rotating Particle near a Planar Surface. *Physical Review Letters*, 118(13):1–5, 2017. ISSN 10797114. doi: 10.1103/PhysRevLett.118.133605.

[78] A Fujimori, Th Müller, F Steiner, J Trümper, P Wölfle, Gerhard Höhler, and Frank Steiner. *Springer Tracts in Modern Physics Managing Editor Springer Tracts in Modern Physics*, volume 240. . ISBN 9783642141881.

[79] A Fujimori, Th Müller, F Steiner, J Trümper, P Wölfle, Gerhard Höhler, and Frank Steiner. *Springer Tracts in Modern Physics Managing Editor Springer Tracts in Modern Physics*, volume 240. . ISBN 9783642141881.

[80] Muddassar Rashid, Tommaso Tufarelli, James Bateman, Jamie Vovrosh, David Hempston, M. S. Kim, and Hendrik Ulbricht. Experimental Realisation of a Thermal Squeezed State of Levitated Optomechanics. 2016. URL http://arxiv.org/abs/1607.05509.

[81] Richard P Feynman, Robert B Leighton, and Matthew Sands. The feynman lectures on physics; vol. i. *American Journal of Physics*, 33(9):750–752, 1965.

[82] JH Hannay. The clausius-mossotti equation: an alternative derivation. *European Journal of Physics*, 4(3):141, 1983.

[83] Edward D Palik. *Handbook of Optical Constants of Solids (Academic, Orlando, 1985)*. Elsevier.

[84] Yoel Tikochinsky and Larry Spruch. Retarded casimir interaction in the asymptotic domain of an electron and a dielectric wall. *Physical Review A*, 48(6):4223, 1993.

[85] Martin Frimmer, Karol Luszcz, Sandra Ferreiro, Vijay Jain, Erik Hebestreit, and Lukas Novotny. Controlling the net charge on a nanoparticle optically levitated in vacuum. *Physical Review A*, 95(6):061801, 2017.

[86] Rozenn Diehl, Erik Hebestreit, René Reimann, Martin Frimmer, Felix Tebbenjohanns, and Lukas Novotny. Optical potential mapping with a levitated nanoparticle at sub-wavelength distances from a membrane. *arXiv preprint arXiv:1803.04917*, 2018.

[87] Martin Frimmer, Karol Luszcz, Sandra Ferrero, Vijay Jain, and Lukas Novotny. Controlling the net charge on a nanoparticle optically levitated in vacuum. *Physical Review A*, 2017. ISSN 2469-9926. doi: 10.1103/PhysRevA.95.061801.

[88] AO Sushkov, WJ Kim, DAR Dalvit, and SK Lamoreaux. Observation of the thermal casimir force. *Nature Physics*, 7(3):230, 2011.

[89] RO Behunin, Y Zeng, DAR Dalvit, and S Reynaud. Electrostatic patch effects in casimir-force experiments performed in the sphere-plane geometry. *Physical Review A*, 86(5):052509, 2012.

[90] RO Behunin, F Intravaia, DAR Dalvit, PA Maia Neto, and S Reynaud. Modeling electrostatic patch effects in casimir force measurements. *Physical Review A*, 85 (1):012504, 2012.

[91] Gerd Binnig, Calvin F Quate, and Ch Gerber. Atomic force microscope. *Physical Review Letters*, 56(9):930, 1986.

[92] Vijay Jain, Jan Gieseler, Clemens Moritz, Christoph Dellago, Romain Quidant, and Lukas Novotny. Direct Measurement of Photon Recoil from a Levitated Nanoparticle. *Arxiv preprint*, pages 3–7, 2016. ISSN 0031-9007. doi: 10.1103/PhysRevLett.116.243601. URL http://arxiv.org/abs/1603.03420.

[93] M R Vanner, I Pikovski, G D Cole, M S Kim, C Brukner, K Hammerer, G J Milburn, and M Aspelmeyer. Pulsed quantum optomechanics .

[94] Jan Gieseler, Lukas Novotny, and Romain Quidant. Thermal nonlinearities in a nanomechanical oscillator. *Nature Physics*, 9(12):806–810, 2013. ISSN 1745-2473. doi: 10.1038/nphys2798. URL http://dx.doi.org/10.1038/nphys2798%5Cn10.1038/nphys2798%5Cnhttp://www.nature.com/nphys/journal/v9/n12/abs/nphys2798.html#supplementary-information.

[95] J Chan, T P Alegre Mayer, A H Safavi-Naeini, J T Hill, A Krause, S Grblacher, M Aspelmeyer, and O Painter. Laser cooling of a nanomechanical oscillator into its quantum ground state. *Nature*, 478, 2011. doi: 10.1038/nature10461. URL https://doi.org/10.1038/nature10461.

[96] Yong S Joe, Arkady M Satanin, and Chang Sub Kim. Classical analogy of fano resonances. *Physica Scripta*, 74(2):259, 2006.

[97] Muddassar Rashid, Marko Toroš, Ashley Setter, and Hendrik Ulbricht. Precession motion in levitated optomechanics. *arXiv preprint arXiv:1805.08042*, 2018.

[98] Ugo Fano. Sullo spettro di assorbimento dei gas nobili presso il limite dello spettro d'arco. *Il Nuovo Cimento (1924-1942)*, 12(3):154–161, 1935.

[99] U. Fano. Effects of configuration interaction on intensities and phase shifts. *Physical Review*, 124(6):1866–1878, 1961. ISSN 0031899X. doi: 10.1103/PhysRev.124.1866.

[100] Mikhail F. Limonov, Mikhail V. Rybin, Alexander N. Poddubny, and Yuri S. Kivshar. Fano resonances in photonics. *Nature Photonics*, 11(9):543–554, 2017. ISSN 1749-4885. doi: 10.1038/nphoton.2017.142. URL http://www.nature.com/doifinder/10.1038/nphoton.2017.142.

[101] Yong S Joe, Arkady M Satanin, and Chang Sub Kim. Classical analogy of Fano resonances. *Physica Scripta*, 74(2):259, 2006. ISSN 1402-4896. doi: 10.1088/0031-8949/74/2/020. URL http://iopscience.iop.org/1402-4896/74/2/020%5Cnhttp://iopscience.iop.org/1402-4896/74/2/020/%5Cnhttp://iopscience.iop.org/1402-4896/74/2/020/pdf/1402-4896_74_2_020.pdf.

[102] J-P Connerade and AM Lane. Interacting resonances in atomic spectroscopy. *Reports on Progress in Physics*, 51(11):1439, 1988.

[103] Stefano Stassi, Alessandro Chiadò, Giuseppe Calafiore, Gianluca Palmara, Stefano Cabrini, and Carlo Ricciardi. Experimental evidence of fano resonances in nanomechanical resonators. *Scientific Reports*, 7(1):1065, 2017.

[104] Liron Stern, Meir Grajower, and Uriel Levy. resonantly coupled plasmonic atomic system. *Nature Communications*, 5:1–9, 2014. doi: 10.1038/ncomms5865. URL http://dx.doi.org/10.1038/ncomms5865.

[105] Fan Wang, Xiang Wang, Haifeng Zhou, Qiang Zhou, Yinlei Hao, Xiaoqing Jiang, Minghua Wang, and Jianyi Yang. Fano-resonance-based Mach-Zehnder optical switch employing dual-bus coupled ring resonator as two-beam interferometer. *Optics express*, 17(9):7708–7716, 2009. ISSN 1094-4087. doi: 10.1364/OE.17.007708.

[106] Reza Asadi, Mohammad Malek-Mohammad, and Sina Khorasani. All optical switch based on Fano resonance in metal nanocomposite photonic crystals. *Optics Communications*, 284(8):2230–2235, 2011. ISSN 00304018. doi: 10.1016/j.optcom.2010.12.085. URL http://dx.doi.org/10.1063/1.4893451.

[107] C. F. Roos, D. Leibfried, A. Mundt, F. Schmidt-Kaler, J. Eschner, and R. Blatt. Experimental Demonstration of Ground State Laser Cooling with Electromagnetically Induced Transparency. *Physical Review Letters*, 85(26):5547–5550, 2000. ISSN 0031-9007. doi: 10.1103/PhysRevLett.85.5547. URL https://link.aps.org/doi/10.1103/PhysRevLett.85.5547.

[108] Y. Lin, J. P. Gaebler, T. R. Tan, R. Bowler, J. D. Jost, D. Leibfried, and D. J. Wineland. Sympathetic electromagnetically-induced-transparency laser cooling of motional modes in an ion chain. *Physical Review Letters*, 110(15):1–5, 2013. ISSN 00319007. doi: 10.1103/PhysRevLett.110.153002.

[109] Keyu Xia and J??rg Evers. Ground State Cooling of a Nanomechanical Resonator in the Nonresolved Regime via Quantum Interference. *Physical Review Letters*, 103(22):1–4, 2009. ISSN 00319007. doi: 10.1103/PhysRevLett.103.227203.

[110] Mohammad Ali Abbassi and Khashayar Mehrany. The impact of Fano resonance on enhancing the cooling of a levitated nanosphere in the resolved sideband regime. pages 1–15, 2017. URL https://arxiv.org/pdf/1707.05823.pdf.

[111] Boris Luk'yanchuk, Nikolay I. Zheludev, Stefan A. Maier, Naomi J. Halas, Peter Nordlander, Harald Giessen, and Chong Tow Chong. The Fano resonance in plasmonic nanostructures and metamaterials. *Nature materials*, 9(9):707–15, 2010. ISSN 1476-1122. doi: 10.1038/nmat2810. URL http://www.ncbi.nlm.nih.gov/pubmed/20733610%5Cnhttp://www.nature.com/doifinder/10.1038/nmat2810.

[112] Muddassar Rashid, Marko Toroš, and Hendrik Ulbricht. Wigner function reconstruction in levitated optomechanics. *Quantum Measurements and Quantum Metrology*, 4(1):17–25, 2017.

[113] AO Caldeira and AJ Leggett. Physica (amsterdam) 121a, 587 (1983). *Phys. Rev. A*, 31:1059, 1985.

[114] Heinz-Peter Breuer and Francesco Petruccione. *The theory of open quantum systems*. Oxford University Press on Demand, 2002.

[115] HM Wiseman and GJ Milburn. Interpretation of quantum jump and diffusion processes illustrated on the bloch sphere. *Physical Review A*, 47(3):1652, 1993.

[116] George Winstone, Markus Rademacher, Robert Bennett, Stefan Buhmann, and Hendrik Ulbricht. Direct measurement of short-range forces with a levitated nanoparticle. pages 1–12, 2017. ISSN 1748-3387. URL http://arxiv.org/abs/1712.01426.

[117] Andreas Jöckel, Aline Faber, Tobias Kampschulte, Maria Korppi, Matthew T. Rakher, and Philipp Treutlein. Sympathetic cooling of a membrane oscillator in a hybrid mechanicalatomic system. *Nature Nanotechnology*, 10(1):55–59, 2014. ISSN 1748-3387. doi: 10.1038/nnano.2014.278. URL http://www.nature.com/doifinder/10.1038/nnano.2014.278.

[118] Ivan S Maksymov. Optical switching and logic gates with hybrid plasmonic–photonic crystal nanobeam cavities. *Physics Letters A*, 375(5):918–921, 2011.

[119] Jiagui Wu, Shu-Wei Huang, Yongjun Huang, Hao Zhou, Jinghui Yang, Jia-Ming Liu, Mingbin Yu, Guoqiang Lo, Dim-Lee Kwong, Guangqiong Xia, and Chee Wei

Wong. Dynamical chaos in chip-scale optomechanical oscillators. (1), 2016. URL http://arxiv.org/abs/1608.05071.

[120] Mei Wang, Xin-You Lü, Jin-Yong Ma, Hao Xiong, Liu-Gang Si, and Ying Wu. Controllable chaos in hybrid electro-optomechanical systems. *Scientific Reports*, 6:22705, 2016. ISSN 2045-2322. doi: 10.1038/srep22705. URL http://www.nature.com/articles/srep22705.

[121] Guanyu Wang and Sailing He. A quantitative study on detection and estimation of weak signals by using chaotic Duffing oscillators. *IEEE Transactions on Circuits and Systems I: Fundamental Theory and Applications*, 50(7):945–953, 2003. ISSN 10577122. doi: 10.1109/TCSI.2003.812606.

[122] Norbert Marwan, M. Carmen Romano, Marco Thiel, and J??rgen Kurths. Recurrence plots for the analysis of complex systems. *Physics Reports*, 438(5-6):237–329, 2007. ISSN 03701573. doi: 10.1016/j.physrep.2006.11.001.

[123] Muddassar Rashid, Tommaso Tufarelli, James Bateman, Jamie Vovrosh, David Hempston, M. S. Kim, and Hendrik Ulbricht. Experimental Realization of a Thermal Squeezed State of Levitated Optomechanics. *Physical Review Letters*, 2016. ISSN 10797114. doi: 10.1103/PhysRevLett.117.273601.

[124] Geoff Boeing. Visual analysis of nonlinear dynamical systems: chaos, fractals, self-similarity and the limits of prediction. *Systems*, 4(4):37, 2016.

[125] LA Month and R Ho Rand. An application of the poincaré map to the stability of nonlinear normal modes. *Journal of Applied Mechanics*, 47(3):645–651, 1980.

[126] Joshua Wilkie. Numerical methods for stochastic differential equations. *Physical Review E - Statistical, Nonlinear, and Soft Matter Physics*, 70(1 2):1–5, 2004. ISSN 15393755. doi: 10.1103/PhysRevE.70.017701.

[127] G Wang, D Chen, J Lin, and X Chen. The application of chaotic oscillators to weak signal detection. *Industrial Electronics, IEEE ...*, 46 (2):440–444, 1999. ISSN 02780046. doi: 10.1109/41.753783. URL http://ieeexplore.ieee.org/lpdocs/epic03/wrapper.htm?arnumber=753783%5Cnhttp://ieeexplore.ieee.org/xpls/abs_all.jsp?arnumber=753783.

[128] Michael Schmidt and Hod Lipson. Distilling free-form natural laws from experimental data. *science*, 324(5923):81–85, 2009.

[129] Josh Bongard and Hod Lipson. Automated reverse engineering of nonlinear dynamical systems. *Proceedings of the National Academy of Sciences*, 104(24):9943–9948, 2007.

[130] Steven L Brunton, Joshua L Proctor, and J Nathan Kutz. Discovering governing equations from data by sparse identification of nonlinear dynamical systems. *Proceedings of the National Academy of Sciences*, page 201517384, 2016.

[131] Celso Grebogi, Edward Ott, and James A Yorke. Chaotic attractors in crisis. *Physical Review Letters*, 48(22):1507, 1982.

[132] L Bakemeier, A Alvermann, and H Fehske. Route to chaos in optomechanics. *Physical review letters*, 114(1):013601, 2015.

[133] A. Serletis, A. Shahmoradi, and D. Serletis. Effect of noise on estimation of Lyapunov exponents from a time series. *Chaos, Solitons & Fractals*, 32(2):883–887, 2007. ISSN 09600779. doi: 10.1016/j.chaos.2005.11.048. URL http://dx.doi.org/10.1016/j.chaos.2005.11.048.

[134] Mikail Rubinov, Olaf Sporns, Cees van Leeuwen, and Michael Breakspear. Symbiotic relationship between brain structure and dynamics. *BMC neuroscience*, 10:55, 2009. ISSN 1471-2202. doi: 10.1186/1471-2202-10-55. URL http://www.pubmedcentral.nih.gov/articlerender.fcgi?artid=2700812&tool=pmcentrez&rendertype=abstract.

[135] N. Marwan, N. Wessel, U. Meyerfeldt, A. Schirdewan, and J. Kurths. Recurrence Plot Based Measures of Complexity and its Application to Heart Rate Variability Data. *Physical review E*, 66(2):1–16, 2002. ISSN 15393755. doi: 10.1103/PhysRevE.66.026702. URL http://arxiv.org/abs/physics/0201064.

[136] Francesco Ricci, Raúl A Rica, Marko Spasenović, Jan Gieseler, Loïc Rondin, Lukas Novotny, and Romain Quidant. Optically levitated nanoparticle as a model system for stochastic bistable dynamics. *Nature communications*, 8:15141, 2017.

[137] Guanyu Wang, Dajun Chen, Jianya Lin, and Xing Chen. The application of chaotic oscillators to weak signal detection. *IEEE Transactions on industrial electronics*, 46(2):440–444, 1999.

[138] Guanyu Wang and Sailing He. A quantitative study on detection and estimation of weak signals by using chaotic duffing oscillators. *IEEE Transactions on Circuits and Systems I: Fundamental Theory and Applications*, 50(7):945–953, 2003.

[139] C-K Peng, Sergey V Buldyrev, Shlomo Havlin, Michael Simons, H Eugene Stanley, and Ary L Goldberger. Mosaic organization of dna nucleotides. *Physical review e*, 49(2):1685, 1994.

[140] C-K Peng, Shlomo Havlin, H Eugene Stanley, and Ary L Goldberger. Quantification of scaling exponents and crossover phenomena in nonstationary heartbeat

time series. *Chaos: An Interdisciplinary Journal of Nonlinear Science*, 5(1):82–87, 1995.

[141] RM Bryce and KB Sprague. Revisiting detrended fluctuation analysis. *Scientific reports*, 2:315, 2012.

[142] J A Rushton, M Aldous, and M D Himsworth. Contributed Review : The feasibility of a fully miniaturized magneto-optical trap for portable ultracold quantum technology Contributed Review : The feasibility of a fully miniaturized magneto-optical trap for portable ultracold quantum technology. *Review of scientific instruments*, 121501(2014), 2017. doi: 10.1063/1.4904066.

[143] M. Bahrami, M. Paternostro, A. Bassi, and H. Ulbricht. Non-interferometric Test of Collapse Models in Optomechanical Systems. pages 1–7, 2014. doi: 10.1103/PhysRevLett.112.210404. URL http://arxiv.org/abs/1402.5421%0Ahttp://dx.doi.org/10.1103/PhysRevLett.112.210404.

[144] Rainer Kaltenbaek, Markus Aspelmeyer, Peter F Barker, Angelo Bassi, James Bateman, Kai Bongs, Sougato Bose, Claus Braxmaier, Časlav Brukner, Bruno Christophe, et al. Macroscopic quantum resonators (maqro): 2015 update. *EPJ Quantum Technology*, 3(1):5, 2016.

[145] Gerald Hechenblaikner, Fabian Hufgard, Johannes Burkhardt, Nikolai Kiesel, Ulrich Johann, Markus Aspelmeyer, and Rainer Kaltenbaek. How cold can you get in space? quantum physics at cryogenic temperatures in space. *New Journal of Physics*, 16(1):013058, 2014.

[146] R Kaltenbaek and M Aspelmeyer. *Erwin Schrodinger - 50 years on: Optomechanical Schrdinger cats - a case for space*. European Mathematical society publishing house, Vienna, 2013. URL https://doi.org/10.4171/121-1/6. DOI: 10.4171/121-1/6.

[147] James Bateman, Ian McHardy, Alexander Merle, Tim R Morris, and Hendrik Ulbricht. On the existence of low-mass dark matter and its direct detection. *Scientific reports*, 5:8058, 2015.

[148] George Winstone, Markus Rademacher, Robert Bennett, Stefan Buhmann, and Hendrik Ulbricht. Direct measurement of short-range forces with a levitated nanoparticle. pages 1–12, 2017. ISSN 1748-3387. URL http://arxiv.org/abs/1712.01426.

[149] Ashley Setter, Marko Toroš, Jason F Ralph, and Hendrik Ulbricht. Real-time kalman filter: Cooling of an optically levitated nanoparticle. *Physical Review A*, 97(3):033822, 2018.

[150] J-P Eckmann, S Oliffson Kamphorst, and David Ruelle. Recurrence plots of dynamical systems. *EPL (Europhysics Letters)*, 4(9):973, 1987.